# Ultrasound contrast imaging with multi-pulse transmission

Fanglue Lin

N° d'ordre : 2013ISAL0117 Année 2013

THESE

# Ultrasound Contrast Imaging with Multi-pulse Transmission

Délivrée par
*L'INSTITUT NATIONAL DES SCIENCES APPLIQUEES DE LYON*

Pour obtenir
*DIPLÔME DE DOCTORAT*

École doctorale:
*ELECTRONIQUE, ELECTROTECHNIQUE, AUTOMATIQUE*

Soutenue publiquement le 14 Novembre par
*Fanglue LIN*

## Jury

| | |
|---|---|
| Co-directeur de thèse : | |
| Olivier BASSET | Professeur des Universités, Université Claude Bernard, Lyon I |
| Christian CACHARD | Professeur des Universités, Université Claude Bernard, Lyon I |
| Rapporteur : | |
| Philippe MARMOTTANT | Charge de Recherche CNRS, HDR, Université Joseph Fourier, Grenoble I |
| Ayache BOUAKAZ | Directeur de Recherche INSERM, Tours |
| Examinateur : | |
| François TRANQUART | Directeur de Recherche, Bracco Suisse |
| Denis FRIBOULET | Professeur des Universités, INSA de Lyon |
| Armand ABERGEL | Professeur des Universités - Praticien Hospitalier, Université d'Auvergne |

# INSA Direction de la Recherche - Ecoles Doctorales – Quinquennal 2011-2015

| SIGLE | ECOLE DOCTORALE | NOM ET COORDONNEES DU RESPONSABLE |
|---|---|---|
| **CHIMIE** | **CHIMIE DE LYON**<br>**http://www.edchimie-lyon.fr**<br><br>Insa : R. GOURDON | M. Jean Marc LANCELIN<br>Université de Lyon – Collège Doctoral<br>Bât ESCPE<br>43 bd du 11 novembre 1918<br>69622 VILLEURBANNE Cedex<br>Tél : 04.72.43 13 95<br>directeur@edchimie-lyon.fr |
| **E.E.A.** | **ELECTRONIQUE, ELECTROTECHNIQUE, AUTOMATIQUE**<br>**http://edeea.ec-lyon.fr**<br><br>Secrétariat : M.C. HAVGOUDOUKIAN<br>eea@ec-lyon.fr | M. Gérard SCORLETTI<br>Ecole Centrale de Lyon<br>36 avenue Guy de Collongue<br>69134 ECULLY<br>Tél : 04.72.18 65 55 Fax : 04 78 43 37 17<br>Gerard.scorletti@ec-lyon.fr |
| **E2M2** | **EVOLUTION, ECOSYSTEME, MICROBIOLOGIE, MODELISATION**<br>**http://e2m2.universite-lyon.fr**<br><br>Insa : H. CHARLES | Mme Gudrun BORNETTE<br>CNRS UMR 5023 LEHNA<br>Université Claude Bernard Lyon 1<br>Bât Forel<br>43 bd du 11 novembre 1918<br>69622 VILLEURBANNE Cédex<br>Tél : 06.07.53.89.13<br>e2m2@ univ-lyon1.fr |
| **EDISS** | **INTERDISCIPLINAIRE SCIENCES-SANTE**<br>**http://www.ediss-lyon.fr**<br><br>Sec : Samia VUILLERMOZ<br>Insa : M. LAGARDE | M. Didier REVEL<br>Hôpital Louis Pradel<br>Bâtiment Central<br>28 Avenue Doyen Lépine<br>69677 BRON<br>Tél : 04.72.68.49.09 Fax :04 72 68 49 16<br>Didier.revel@creatis.uni-lyon1.fr |
| **INFOMATHS** | **INFORMATIQUE ET MATHEMATIQUES**<br>**http://infomaths.univ-lyon1.fr**<br><br>Sec :Renée EL MELHEM | Mme Sylvie CALABRETTO<br>Université Claude Bernard Lyon 1<br>INFOMATHS<br>Bâtiment Braconnier<br>43 bd du 11 novembre 1918<br>69622 VILLEURBANNE Cedex<br>Tél : 04.72. 44.82.94 Fax 04 72 43 16 87<br>infomaths@univ-lyon1.fr |
| **Matériaux** | **MATERIAUX DE LYON**<br>**http://ed34.universite-lyon.fr**<br><br>Secrétariat : M. LABOUNE<br>PM : 71.70 –Fax : 87.12<br>Bat. Saint Exupéry<br>Ed.materiaux@insa-lyon.fr | M. Jean-Yves BUFFIERE<br>INSA de Lyon<br>MATEIS<br>Bâtiment Saint Exupéry<br>7 avenue Jean Capelle<br>69621 VILLEURBANNE Cedex<br>Tél : 04.72.43 83 18 Fax 04 72 43 85 28<br>Jean-yves.buffiere@insa-lyon.fr |
| **MEGA** | **MECANIQUE, ENERGETIQUE, GENIE CIVIL, ACOUSTIQUE**<br>**http://mega.ec-lyon.fr**<br><br>Secrétariat : M. LABOUNE<br>PM : 71.70 –Fax : 87.12<br>Bat. Saint Exupéry<br>mega@insa-lyon.fr | M. Philippe BOISSE<br>INSA de Lyon<br>Laboratoire LAMCOS<br>Bâtiment Jacquard<br>25 bis avenue Jean Capelle<br>69621 VILLEURBANNE Cedex<br>Tél :04.72 .43.71.70 Fax : 04 72 43 72 37<br>Philippe.boisse@insa-lyon.fr |
| **ScSo** | **ScSo***<br>**http://recherche.univ-lyon2.fr/scso/**<br><br>Sec : Viviane POLSINELLI<br>Brigitte DUBOIS<br>Insa : J.Y. TOUSSAINT | M. OBADIA Lionel<br>Université Lyon 2<br>86 rue Pasteur<br>69365 LYON Cedex 07<br>Tél : 04.78.77.23.86 Fax : 04.37.28.04.48<br>Lionel.Obadia@univ-lyon2.fr |

*ScSo : Histoire, Géographie, Aménagement, Urbanisme, Archéologie, Science politique, Sociologie, Anthropologie

# ABSTRACT

In ultrasound imaging domain, nonlinear imaging, which utilizes the nonlinear backscattered signals, has become an important branch. Nonlinear imaging, also named harmonic imaging, can be divided into tissue harmonic imaging and contrast harmonic imaging, according to where the nonlinear signals come from. Contrast harmonic imaging emerges because contrast agents, which are intravenously injected to enhance the weak echoes backscattered from blood cells, can vibrate nonlinearly when they undergo a acoustic pressure higher than a threshold. Then, these nonlinear signals backscattered by contrast agents are collected to form harmonic images where the linear echoes backscattered from surrounding tissue are supposed to be removed. However, during the wave propagation in tissue, the interaction between the acoustic wave and tissue medium modifies the wave shape and the harmonics of the transmitted wave are also generated in tissue. The presence of tissue harmonic signals, merged with harmonic signals from contrast agents, degrades the image quality in contrast harmonic imaging.

This thesis aims to better distinguish the echoes from contrast agents and the echoes from tissue, whether through designing new modalities, or investigating and optimizing the existing modalities. Our efforts are mainly focused on the multi-pulse techniques in ultrasound contrast imaging.

Firstly, we propose a mathematical background to generalize most of the multi-pulse ultrasound imaging techniques that have been described in previous literatures. The formulation can be used to predict the nonlinear components in each frequency band and to design new transmission sequences to either increase or decrease specified nonlinear components in each harmonic band. Simulation results on several multi-pulse techniques are in agreement with the results given in previous literatures.

Secondly, the techniques using multiple transmissions to increase the CTR are generally based on the response of static scatterers inside the imaged region. However, scatterer motion, for example in blood vessels, has an inevitable influence on the relevance of the techniques. It can either upgrade or degrade the technique involved. Simulations, *in-vitro* experiments from a single bubble and clouds of bubbles, and *in-vivo* experiments from rats show that the phase shift of the echoes backscattered from bubbles is dependent on the transmissions' phase shift, and that the bubble motion influences the efficiency of multi-pulse techniques. Fundamental and second-harmonic amplitudes of the summed signal change periodically, exhibiting maximum or minimum values, according to scatterer motion. Furthermore, experimental results based on the second-harmonic inversion (SHI) technique reveal that bubble motion

can be taken into account to regulate the pulse repetition frequency (PRF). With the optimal PRF, the CTR of SHI images can be improved compared to second-harmonic images.

Besides of these considerations relative to generalization and scatterer movement in multi pulse techniques, a new technique, called double pulse inversion (DPI), has also been proposed. The PI technique is applied twice before and after the arrival of the contrast agents to the region of interest. The resulting PI signals are substracted to suppress the tissue-generated harmonics and to improve CTR. Simulations and *in-vitro* experimental results have shown an improved CTR of DPI. However, the presence of tissue movements may hamper the effectiveness of this technique. *In-vivo* experimental results confirm that the tissue motion of the rat during the acquisition is an inevitable barrier of this technique.

# ACKNOWLEDGMENT

Firstly, I would like to thank Prof. Philippe Marmottant and Prof. Ayache Bouakaz for their acceptance to be the reviewer of this thesis and their effort to review this thesis manuscript. I am also grateful to the other members of the jury, Prof. François Tranquart, Prof. Denis Friboulet and Prof. Armand Abergel, for their willingness to discuss the work during the defense.

Three years ago, when I finished my Master study in Southeast University in Nanjing, I had a strong willingness to go outside to see the "western world". Therefore, I am very happy to be given the opportunity to pursue my Ph.D. degree in Lab CREATIS in France. I would like to thank my supervisors, Prof. Olivier Basset and Prof. Christian Cachard, for choosing me from the list of applicants. I would also thank Prof. YueMing Zhu, who is responsible for this application program and Prof. Isabelle Magnin, who is the director of the lab, for their approval to my application. I would also show my gratitude to China Scholarship Council (CSC) for the financement during my Ph.D. study.

Special thanks should be given to my supervisors, Prof. Olivier Basset and Prof. Christian Cachard. Your broad scientific view and your enthusiasm to research always inspire me. Your patience and kindness help me pass through the difficult time at the very beginning when I cannot say a single French word. Also thank you for the guidance, the weekly discussions and the corrections to all my papers.

I would like to also acknowledge Prof. Piero Tortoli, Dr. Francesco Guidi, Dr. Riccardo Mori and Dr. Alessandro Ramalli for their warm reception, selfless sharing of their experience and useful help during our collaboration. Also thank you for the real Italian pizza and Italian espresso coffee. I am also grateful to Dr. Aymeric Guibal, who spared his time to help us with the clinical tests.

Ultrasound group in our lab is not only a professional group, but also a friendly group. I am lucky to have these colleagues and make friends with them. François, you are a good example of a researcher. Your smartness, creativity and hardworking impresses me. Thank you for your numerous help and I learned a lot from you. Matthieu, with your warm smile, it is a pleasure having scientific or non scientific conversations with you. Thank you for every detailed explanation to French phrases and French culture. Thank you for being my "tourist guide" during our short stay in Florence. Adeline, with your presence in the ultrasound room, experiments become more efficient when something is missing, not working or needed. Thank you for your assistance. Hervé and Denis, you are very easy-going. Life seems more colorful with your big smile and laughter. Bakary, you are a nice officemate with a good temper. It

was a pleasure sharing an office with you. Sébastien, still remember the short stay in Dresden as my neighbor? Thank you for sending me back in the dark.

During the past three years, I have also made friends with some Chinese students: Feng, Lihui, Yue, Xinxin, Yan, Hongjiang, Changyu, Hongying, Shengfu and Liang. I have many unforgettable memories with you: the “tea time”, the dinner parties, the travel… I also find it interesting to discover the difference between our southern and northern culture in everyday life. I cherish our friendship.

At last, I like to appreciate the support and unconditional love from my parents. Their optimism and open-minded attitude towards the life always give me courage every time when I feel depressed. Pei, the distance between Lyon and Grenoble does not separate us, it makes us closer. Thank you for always being there, for sharing my happiness and sadness, for wiping my tears and fears, for everything.

# CONTENTS

# I. INTRODUCTION

# Chapter 1

## Introduction

## Contents

## 1.1 Medical ultrasound

Every day, we touch with sound, a very common and intuitive physical phenomenon. Then what is sound? Sound is a mechanical wave in nature: a wave that is created by oscillating objects and that propagates through a medium (gas, liquid or solid). An important parameter to describe sound, or acoustic wave, is frequency $f$. According to frequency, sound can be classified to infrasound, audible sound and ultrasound. The frequency of the audible sound, which is perceptible by human ears, is from about 20 $Hz$ to 20 $kHz$. Then the acoustic wave having a frequency higher than 20 $kHz$ is called ultrasound while that having a frequency lower than 20 $Hz$ is called infrasound. As a mechanical wave, sound propagation depends on the properties of the medium. So the physical quantities related to medium, such as pressure $p$, density $\rho$ and sound velocity $c$, are also important. The effects like reflection, refraction, scattering, attenuation, absorption are usually involved in the various applications of sound.

Ultrasound, because of its good directivity, high spatial resolution or high energy, has been applied in various domains, such as underwater detection, industrial flaw detection, distance measurement, mechanical pieces cleaning and alloy production. Besides of these, ultrasound has also been widely used in medical diagnosis, thanks to its safety, real-time property and low cost compared to other medical assisted devices, and in medical treatment like in HIFU (High Intensity Focused Ultrasound) techniques.

For medical ultrasound, the propagation medium is the organs in human body. In biological tissue, the average sound velocity is around 1540 $m/s$. The frequency of the diagnostic ultrasound is usually in the range between 1.5 $MHz$ and 15 $MHz$. So the wavelength of medical ultrasound wave is between 1 $mm$ and 0.1 $mm$. Because the wavelength is larger than the medium particle, or the obstacle, scattering is the dominant effect happening when the ultrasound wave travels through the biological medium. The backscattered signals from all the medium particles during the wave travelling path are captured by the transducer and displayed as an ultrasound image, which can show the anatomy structure of the insonified region.

## 1.2 Thesis objective

Conventionally, the backscattered signals are collected to form an ultrasound image. Nowadays, nonlinear imaging, which utilizes the nonlinear backscattered signals, has become an important branch in ultrasound imaging domain, mainly because nonlinear imaging provides an improved resolution. Nonlinear imaging, also named harmonic imaging, can be divided into tissue harmonic imaging and contrast harmonic imaging, according to where the nonlinear signals come from.

Contrast harmonic imaging emerges because contrast agents, which is intravenously injected to enhance the weak echoes backscattered from blood cells, can vibrate nonlinearly when they undergo a high acoustic pressure, then these nonlinear signals backscattered by contrast agents are collected to form harmonic images, to distinguish the linear echoes backscattered from surrounding tissue. Contrast harmonic imaging is commonly used to help the diagnosis of the cardiovascular disease through observing the anatomical structure of blood vessel, and abdominal organ cancer through observing tissue perfusion dynamics.

However, as already mentioned above, nonlinear signals can also come from tissue. During the wave propagation in tissue, the interaction between the acoustic wave and tissue medium modifies the wave shape, so the harmonics of the transmitted wave are generated. The presence of tissue harmonic signals is merged with the harmonic signals from contrast agents and degrades the image quality in contrast harmonic imaging.

Therefore, the thesis objective is to better distinguish the echoes from contrast agents and the echoes from tissue, whether through designing new modalities, or investigating and optimizing the existing modalities.

## 1.3 Layout of the thesis

In this thesis, efforts are mainly focused on the multi-pulse techniques in ultrasound contrast imaging. The manuscript is divided into the following four parts:

- Introduction part: Chapter 1 leads the readers into the topic of this thesis by a general introduction of medical ultrasound, thesis objective and layout of the thesis.
- Background part: This part introduces the necessary background knowledge in ultrasound nonlinear imaging. Chapter 2 describes the linear and nonlinear behaviors of contrast agent bubbles and presents different models generally used. Chapter 3 presents the nonlinear phenomenon of wave propagation, the equations used to describe the nonlinear propagation, and then introduces two simulators used in this thesis.
- Contribution part: This part presents my original works on the nonlinear imaging, especially on the multi-pulse techniques in ultrasound contrast imaging. Chapter 4 generalizes most of the multi-pulse techniques applied in contrast imaging, using a single formula. This formula can be used to predict each nonlinear component in each harmonic band. Simulations have been conducted to validate this formula. Chapter 5 investigates the influence of bubble movement to multi-pulse techniques. Simulations and experimental results on a single bubble and a cloud of bubbles are presented. Based on these results, the optimization of second harmonic inversion (SHI) imaging, a

recently proposed multi-pulse technique, is also presented. Chapter 6 proposes a new modality named double pulse inversion (DPI), using the pulse inversion technique twice, to reduce the tissue-generated harmonics to increase contrast-to-tissue ratio (CTR). Simulations and experimental results are presented.

- Conclusion and perspectives part: Chapter 7 concludes the contributions of this thesis and gives the perspectives of the work.

# II. BACKGROUND

# Chapter 2

## Ultrasound contrast agents

## Contents

## 2.1 Introduction

Ultrasound contrast agents (UCA) are a collection of microbubbles, intravenously injected into human body as a red blood cell enhancer. It is applied to ultrasound after the gas microbubbles were reported to have the ability to increase the reflectivity [Gramiak *et al.* (1968)].

Contrast agents are expected to be persistent enough to complete the diagnosis process, small enough to move into capillaries and pass through pulmonary circulation, and inert enough not to alter hemodynamics. Nowadays, contrast agents are usually gas-filled and encapsulated. The acoustic properties of contrast agents are strongly influenced by the kinds of capsule material. So efforts have also been taken to the measurement of acoustic properties of microbubbles and to the production of them.

This chapter introduces the linear and nonlinear behavior of a free gas microbubble in section 2.2, and then presents the characteristics, the models and the medical applications of ultrasound contrast agents in section 2.3. At last, a short conclusion is given in section 2.4.

## 2.2 Microbubble

The diameter of a microbubble is on the order of micron. As it is much smaller than ultrasound wavelength (between 0.1 $mm$ to 1 $mm$), the bubble behaves like a Rayleigh scatterer.

### 2.2.1 Linear behavior

Air bubble in water has a cross section 100 million times greater than that of the iron sphere having the same radius, because of the significantly different compressibility of the gas bubble [De Jong (1993)].

An air bubble has a flexible boundary with surrounding fluid. The response of the bubble depends on two factors: the springlike stiffness of the gas and the inertia of the fluid. The balance between the two factors can leads to the resonant frequency:

$$f_r = \frac{1}{2\pi R_0}\sqrt{\frac{3\gamma_C p_0}{\rho}} \tag{2.1}$$

where $R_0$ is the equilibrium bubble radius, $\gamma_C$ is the ratio of heat capacities at constant pressure and constant volume, $p_0$ is the static pressure at the bubble surface and $\rho$ is the density of the surrounding liquid.

When there is an acoustic pressure on the bubble, the bubble contracts and expands with this external force.

### 2.2.2 Nonlinear behavior

When the pressure amplitude is large, a bubble can expand more than compress. Recently it has also been found that some bubbles had "compress-only" behavior [De Jong *et al.* (2007)]. These asymmetric vibrations lead to nonlinear response of bubbles. Lord Rayleigh [Rayleigh (1917)] was the first one to describe the behavior of a microbubble by an equation, this equation has been improved by Plesset [Plesset (1949)], Nolting and Nepiras [Noltingk *et al.* (1950)], and Poritsky [Poritsky (1952)]. All these contributions lead to the Rayleigh-Plesset equation:

$$R\ddot{R} + \frac{3\dot{R}^2}{2} = \frac{1}{\rho}\left(\left(p_0 + \frac{2\sigma}{R_0} - p_v\right)\left(\frac{R_0}{R}\right)^{3\kappa} + p_v - p_0 - \frac{2\sigma}{R} - \frac{4\mu\dot{R}}{R} - P\right) \qquad (2.2)$$

where $R_0$ is the equilibrium bubble radius, $\rho$ is the liquid density, $p_0$ is the static pressure at the bubble surface, $p_v$ is the liquid vapor pressure, $\mu$ is the damping term for the shear viscosity of the fluid, $\sigma$ is the surface tension term, $\kappa$ is the polytropic gas index. $R$ is the time-varying radius of the bubble, acted on by a time-varying acoustic pressure $P$. $\dot{R}$ and $\ddot{R}$ are the velocity and the acceleration of the bubble surface. Equation (2.2) describes the dynamics of a free gas bubble without shell in an incompressible fluid.

## 2.3 Ultrasound contrast agents

### 2.3.1 Characteristics of ultrasound contrast agents

Different from air bubbles, a contrast agent usually has a shell outside the gas core. The majority of these gases are perfluorocarbon-like gases or air, and the shells vary from serum albumin to surfactants. The diameter of contrast agents is about 1-10 $\mu m$ and the thickness of the shell is about 10-200 $nm$.

With the presence of the shell, the expansion of a contrast agent is constrained and the resonant frequency is raised. So the resonant frequency becomes:

$$f_{re}{}^2 = f_r{}^2 + \frac{S_p}{4\pi^2 m} \qquad (2.3)$$

where $S_p$ is the stiffness of the shell, $m$ is the effective mass of the system, and $f_r$ is the free gas bubble resonance expressed by equation (2.1).

Before talking about the behavior of these contrast agents, the concept of mechanical index (MI) should be introduced. MI is a parameter to estimate the likelihood of inertial cavitation with an intervening tissue path:

$$MI = \frac{P_r'}{\sqrt{f_c}} \qquad (2.4)$$

where $f_c$ is the center frequency ($MHz$), $P_r'$ is the maximum axial value of rarefactional pressure measured in water ($MPa$), $p_r(z)$, multiplied by an *in situ* exponential factor:

$$P_r' = max[p_r(z)e^{-0.0345 f_c z}] \quad (2.5)$$

In United States, the allowed maximum MI for medical ultrasound imaging is 1.9 [Szabo (2004)].

The behavior of contrast agents under acoustic excitation depends on the exciting pressure and frequency, and the structure of the microbubbles:

$$\begin{cases} stable\ linear\ scattering & low\ MI \\ stable\ nonlinear\ scattering & medium\ MI \\ transient\ nonlinear\ scattering & high\ MI \end{cases} \quad (2.6)$$

### 2.3.2 Models of ultrasound contrast agents

To well understand the behavior of contrast agents, efforts have been done to model the vibration of the contrast agent microbubbles.

#### *2.3.2.1 Rayleigh-Plesset model*

The basic equation to describe oscillating gas bubble is the Rayleigh-Plesset equation, which has been presented in equation (2.2) and is rewritten here:

$$R\ddot{R} + \frac{3\dot{R}^2}{2} = \frac{1}{\rho}\left[\left(p_0 + \frac{2\sigma}{R_0} - p_v\right)\left(\frac{R_0}{R}\right)^{3\kappa} + p_v - p_0 - \frac{2\sigma}{R} - \frac{4\mu\dot{R}}{R} - P\right] \quad (2.7)$$

This equation is applicable to a spherically symmetrical free gas bubble in an incompressible fluid, but the effect of shell is missing [Leighton (1994)].

#### *2.3.2.2 De Jong model*

The model proposed by De Jong *et al.* modifies the basic Rayleigh-Plesst equation to take into account shell and other damping effects as well as shell forces. The shell is assumed to be extremely thin. With the presence of the shell, the stiffness of the contrast agent is strengthened and the sound damping is increased. Therefore, instead of the viscosity damping of the fluid, a total damping parameter is given [De Jong *et al.* (1992)]:

$$\delta_t = \delta_{vis} + \delta_{rad} + \delta_{th} + \delta_f \quad (2.8)$$

where $\delta_{vis}$ is the viscous damping, $\delta_{rad}$ is radiation damping, $\delta_{th}$ is thermal conduction damping and $\delta_f$ is damping due to friction within the shell. So together with a shell elastic parameter $S_p$ used to describe the shell-restoring force, the modified equation is given [De Jong *et al.* (1993)]:

$$R\ddot{R} + \frac{3\dot{R}^2}{2} = \frac{1}{\rho}\left[p_{g0}\left(\frac{R_0}{R}\right)^{3\kappa} + p_v - p_0 - \frac{2\sigma}{R} - S_p\left(\frac{1}{R_0} - \frac{1}{R}\right) - \delta_t\omega_0\rho R\dot{R} - P\right] \quad (2.9)$$

where $p_{g0}$ is the initial pressure inside the bubble and $\omega_0$ is the center pulsation of the excitation wave. The parameters $S_p$ and $\delta_t$ were determined by experimental measurements on Albunex bubbles.

#### 2.3.2.3 Hoff model

The model proposed by Hoff *et al.* accounts for the finite thickness of the shell and forces, elastic nature of the shell in a more accurate way. A more accurate description of the effects of the shell have been presented by Hoff *et al.* [Hoff *et al.* (2000)] based on Church model [Church (1995)]. The shell thickness is modeled as a viscoelastic layer that changes thickness in proportion to the stretching of the dynamic radius.

$$R\ddot{R} + \frac{3\dot{R}^2}{2} = \frac{1}{\rho_L}\left\{p_0\left[\left(\frac{R_0}{R}\right)^{3\kappa} - 1\right] - 4\mu_L\frac{\dot{R}}{R} - 12\mu_S\frac{d_{S0}R_0^2}{R^3}\frac{\dot{R}}{R} - 12G_S\frac{d_{S0}R_0^2}{R^3}\left(1 - \frac{R_0}{R}\right) - P\right\} \tag{2.10}$$

where $\rho_L$ and $\mu_L$ are the densities and the shear viscosity of the surrounding liquid, $d_{S0}$, $\mu_S$ and $G_S$ are the initial thickness, the shear viscosity and the shear modulus of the shell. In this equation, two shell parameters, the shear modulus $G_S$ and the shear viscosity $\mu_S$, were determined from measurements on experimental bubbles from Nycomed.

#### 2.3.2.4 Marmottant model

Another model can describe the behavior that microbubble can break up when the driving pressure is high enough [Marmottant *et al.* (2005)]. A surface tension varying with bubble radius is added. The equation is:

$$R\ddot{R} + \frac{3\dot{R}^2}{2} = \frac{1}{\rho}\left[\left(p_0 + \frac{2\sigma}{R_0} - p_v\right)\left(\frac{R_0}{R}\right)^{3\kappa}\left(1 - \frac{3\kappa}{c}\dot{R}\right) - p_0 - \frac{2\sigma_R}{R} - \frac{4\dot{R}}{R}\left(\mu_L - \frac{\kappa_S}{R}\right) - P\right] \tag{2.11}$$

where the surface tension is defined as:

$$\sigma_R = \begin{cases} 0 & R \le R_{bucking} \\ \lambda\left(\dfrac{R^2}{R_{bucking}^2} - 1\right) & R_{bucking} \le R \le R_{rupture} \\ \sigma_{water} & R \ge R_{rupture} \end{cases} \tag{2.12}$$

The rupture radius $R_{rupture}$, the bucking radius $R_{bucking}$ were determined by experimental measurements on SonoVue and BR14 bubbles, which have phospholipid shells.

There also exist many other models. More details can be found in the review paper by Allen *et al.* [Allen *et al.* (2002)] and Faez *et al* [Faez *et al.* (2013)].

### 2.3.3 Applications of ultrasound contrast agents

The application of ultrasound contrast agents falls into two scopes: diagnosis and therapy.

One major diagnostic application is opacification, which is the brightening of a blood pool. For example, the blood pool volume of the left ventricle of the heart is tracked to determine the ejection fraction to measure the function of the heart acting as a pump, or to identify irregular local wall motions of the endocardium under stress testing [Szabo (2004)]. Another diagnostic application is perfusion, which is the amount of blood delivered into a local volume of tissue per unit of time. For example, perfusion of myocardium can be measured, and regions where blood cannot reach may indicate ischemia or infarct; perfusion of other tissues can indicate angiogenesis or increased vascularization in tumors and the location of lesions [Szabo (2004)].

For therapeutic applications, contrast agents are designed to carry drugs to targeted sites and release medication by ultrasound-induced fragments, in order to avoid wasting large amount of medications throughout the body, to prevent unwanted side effects, and to ensure the drugs are delivered to the intended sites. For example, the agents can find and bind with thrombi and vulnerable plaque [Lindner (2001)]. The agents can also deliver cytotoxic drugs to angiogenesis sites to prevent feeding tumor growth [Lindner (2001)].

## 2.4 Conclusion

In this chapter, a brief review about ultrasound contrast agents is presented. This thesis mainly pays attention to the nonlinear responses or the harmonics of these contrast agents because the thesis objective is to detect and distinguish the harmonic signals generated by contrast agents and by tissues.

# Chapter 3

## Nonlinear ultrasound propagation

## Contents

## 3.1 Introduction

When the ultrasound wave propagation is studied, a simplification is generally made, considering that the waves obey the principle of linearity. Linearity means that waves keep the same shape as they change amplitude and that different scaled versions of waves at a given location can be combined to form more complicated waves. Because biological tissues have high water content, wave propagation in the body is often modeled as in liquids [Szabo (2004)].

In reality, tissue has a nonlinear behavior, as is much of the world around us. This nonlinearity alters the linear situation and complicates the solution to wave propagation equations. This thesis aims to decrease the nonlinear components generated by tissue, so the principle of nonlinear wave propagation in tissue should also be understood.

In section 3.2, linear wave propagation theory is firstly introduced. In section 3.3, the nonlinear parameter, which is very important in nonlinear ultrasound theory, and the physical interpretation of this parameter are presented in section 3.3.1, then several nonlinear wave equations are described from section 3.3.2 to section 3.3.4. At last, in section 3.4, two nonlinear simulators are presented.

## 3.2 Linear propagation

When the wave disturbance pressure $p$ passes through the medium, the medium particles are displaced from their original equilibrium at a rate or particle velocity $\vec{u}$. If the viscosity of the medium is neglected, the propagation of the ultrasound wave obeys the linearized Euler's equations:

- Conservation of mass

$$\frac{\partial \rho}{\partial t} + \rho \nabla \cdot \vec{u} = 0 \tag{3.1}$$

- Conservation of momentum

$$\rho \frac{\partial \vec{u}}{\partial t} + \nabla p = 0 \tag{3.2}$$

where $\rho$ is the density of the medium. Eq.(3.1) and Eq.(3.2) mean that the changes in density from equilibrium values are proportional to the input disturbance.

Another assumption is made that the process is adiabatic, meaning that there is no heat transfer during the rapid fluctuations of an acoustic wave. Under this assumption and for infinitesimal amplitudes, linearity holds as described by:

$$p - p_0 = \left[\rho_0 \left(\frac{\partial p}{\partial \rho}\right)_{S,\rho=\rho_0}\right]\left(\frac{\rho - \rho_0}{\rho_0}\right) = \rho_0 c_0^2 \left(\frac{\rho - \rho_0}{\rho_0}\right) \tag{3.3}$$

where $p_0$ and $\rho_0$ are the pressure and density at equilibrium, $\rho_0 c_0^2$ is a constant taken for $\rho = \rho_0$ and at a specific entropy $S$.

## 3.3 Nonlinear ultrasound

The equations in section 3.2 are based on infinitesimal amplitudes. However, in reality, the pressure amplitudes are finite. So the equation of momentum (Eq.(3.2)) becomes [Hamilton (1988)]:

$$\rho\left(\frac{\partial \vec{u}}{\partial t}+(\vec{u}\cdot\nabla)\vec{u}\right)=-\nabla p \tag{3.4}$$

In this equation, the convective acceleration term, $(\vec{u}\cdot\nabla)\vec{u}$, is added. This term explains the nonlinear propagation and also complicates the analytical solution of Eq.(3.4).

The equation of state (Eq. (3.3)) becomes [Beyer (1960)]:

$$\begin{aligned} p-p_0=&\left[\rho_0\left(\frac{\partial p}{\partial \rho}\right)_{S,\rho=\rho_0}\right]\left(\frac{\rho-\rho_0}{\rho_0}\right)\\ &+\frac{1}{2!}\left[{\rho_0}^2\left(\frac{\partial^2 p}{\partial \rho^2}\right)_{S,\rho=\rho_0}\right]\left(\frac{\rho-\rho_0}{\rho_0}\right)^2+\cdots \end{aligned} \tag{3.5}$$

In this equation, a Taylor expansion series are included to get more accurate pressure as a function of density.

### 3.3.1 Nonlinear parameters

Eq.(3.5) can be rewritten as:

$$p'=A\left(\frac{\rho'}{\rho_0}\right)+\frac{B}{2!}\left(\frac{\rho'}{\rho_0}\right)^2+\cdots \tag{3.6}$$

where

$$p'=p-p_0 \tag{3.7}$$

$$\rho'=\rho-\rho_0 \tag{3.8}$$

$$A=\rho_0\left(\frac{\partial p}{\partial \rho}\right)_{S,\rho=\rho_0}=\rho_0 c_0^2 \tag{3.9}$$

$$B={\rho_0}^2\left(\frac{\partial^2 p}{\partial \rho^2}\right)_{S,\rho=\rho_0} \tag{3.10}$$

Then, the relative amount of nonlinearity is expressed by nonlinear parameter $B/A$. More common is the coefficient of nonlinearity, $\beta$, which is defined as:

$$\beta=1+\frac{B}{2A} \tag{3.11}$$

The quadratic dependence of pressure on density leads to a change in sound speed between the positive and negative half cycle of the pressure.

For a sinusoidal plane wave in a lossless nonlinear medium, the speed of sound for a displacement amplitude $d$ is expressed as:

$$c=c_0+\beta d=c_0+\frac{\beta\Delta p}{\rho_0 c_0} \tag{3.12}$$

Eq.(3.12) indicates that the positive pressure speeds up the sound speed while the negative pressure slows down it. In other words, the positive peaks move faster than the negative peaks. This leads to a shape distortion of the sinusoidal wave. Figure 3.1(a) and Figure 3.1(b) illustrate the initial waveform of a sinusoidal pressure wave and the waveform after distortion. This phenomenon can also been observed in the frequency domain. For the initial wave, only the fundamental component is present, as seen in Figure 3.1(c). For the distorted wave, several harmonic components appear, as seen in Figure 3.1(d).

When the positive peaks continue moving forward and the negative peaks retreating, the wave becomes a sawtooth with an infinite slope. This phenomenon is called shock formation. Let's define the normalized distance nonlinearity parameter $\sigma$ as:

$$\sigma = \beta\varepsilon kz = \frac{\beta p_0 \omega_0 z}{\rho_0 c_0^3} \tag{3.13}$$

where $\varepsilon$ is the acoustic Mach number, $\varepsilon = d_0/c_0 = p_0/(\rho_0 c_0^2)$, $k$ is the wave number, $k = \omega/c_0$, and $z$ is the distance from the source. Eq.(3.13) indicates that the extent of distortion depends on nonlinearity $\beta$, frequency $f$, amplitude $p_0$ and distance $z$. Shock occurs when $\sigma = 1$.

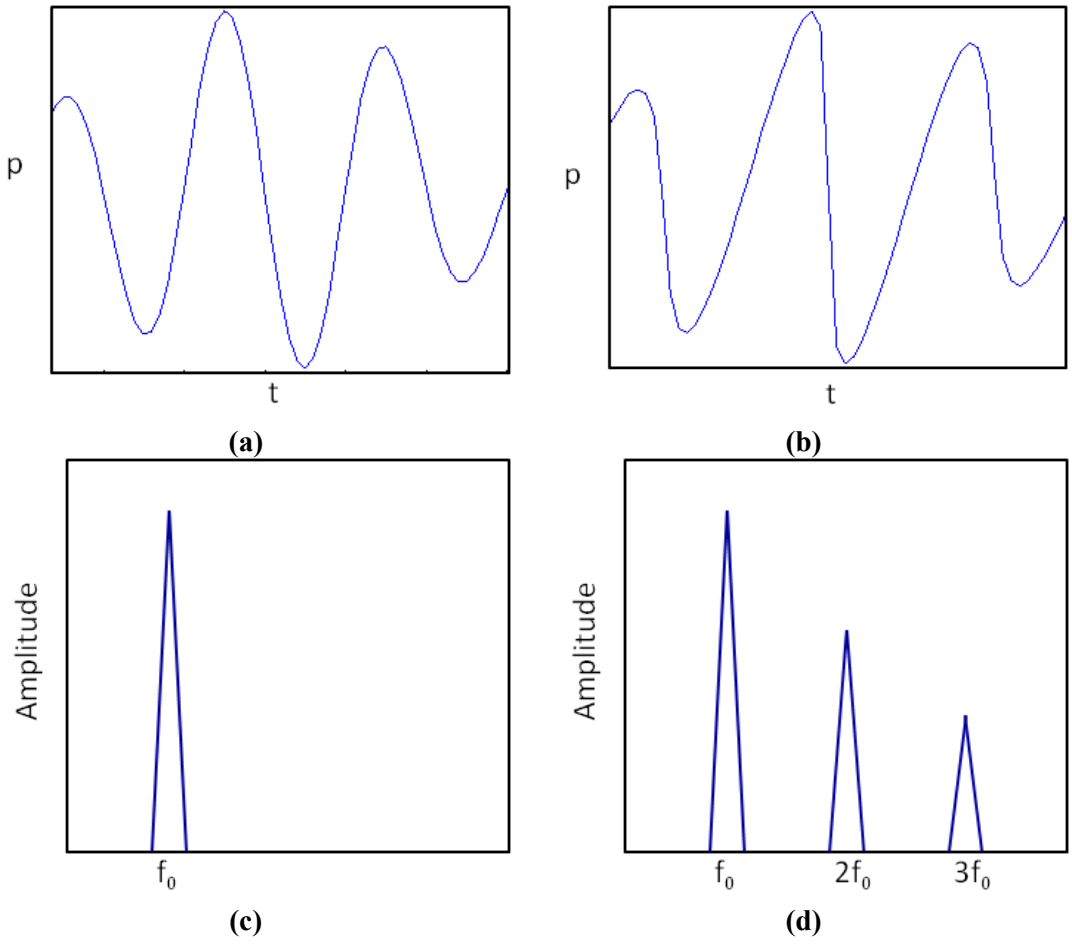

Figure 3.1 Illustration of the initial waveform of a sinusoidal pressure wave (a) and the waveform after deformation (b). In frequency domain, only fundamental component is present for initial wave (c), while the harmonic components appear for deformed wave (d).

The nonlinear coefficient $\beta$ for biological tissue falls in the range of 3 to 7 [Duck (1990)], while the contrast agents can have nonlinear coefficient of more than 1000 if the concentration is high [Wu *et al.* (1998)]. Table 3.1 lists the values of nonlinear coefficient for several different biological tissues.

Table 3.1 Value of nonlinear coefficient for several biological tissues

| Medium | Nonlinear coefficient $\beta$ |
|---|---|
| water | 3.48 |
| fat | 6.4 |
| muscle | 4.55 |
| liver | 4.85 |
| blood | 4.35 |

### 3.3.2 Lossless Burgers equation

The propagation of a plane wave in a lossless medium can be described by the lossless Burgers equation [Burgers (1948)]:

$$\frac{\partial p}{\partial z} = \frac{\beta p}{\rho_0 c_0^3}\frac{\partial p}{\partial \tau} \tag{3.14}$$

where $\tau$ is the delayed time, $\tau = t - z/c_0$. The solution of Eq.(3.14) was proposed by Fubini [Fubini (1935)]:

$$p(z,\tau) = p_0 \sum_{n=1}^{\infty} \frac{2}{nz_d} J_n(nz_d)\sin(n\omega_0\tau) \tag{3.15}$$

where $n$ is the number of harmonic, $J_n$ is the Bessel function of $n^{th}$ order and $z_d$ is the dimentionless distance, expressed as:

$$z_d = \frac{\omega_0 \beta p_0}{\rho_0 c_0^3} z \tag{3.16}$$

### 3.3.3 Complete Burgers equation

In reality, the ultrasound wave propagation has not only nonlinear effect, but also the absorption and dispersion effects. Because of these effects, some of the wave energy is converted in heat. So the wave energy is attenuated.

Taking into account the attenuation, the Burgers equation is expressed as:

$$\frac{\partial p}{\partial z} = \frac{\beta p}{\rho_0 c_0^3}\frac{\partial p}{\partial \tau} + \frac{\delta}{2c_0^3}\frac{\partial^2 p}{\partial \tau^2} \tag{3.17}$$

where $\delta$ is the effect of the thermo-viscious dissipation.

### 3.3.4 KZK equation

Section 3.3.2 and section 3.3.3 consider a plane wave propagation, however in reality, transducers have finite size. So the diffraction effect should also be taken into account. The complete model of nonlinear wave propagation in a medium can be described by the Khokhlov-Zabolotskaya-Kuznetsov (KZK) equation [Zabolotskaya *et al.* (1969); VP Kuznetsov (1970)]:

$$\frac{\partial p}{\partial z} = \frac{c_0}{2}\Delta_\perp p + \frac{\delta}{2c_0^3}\frac{\partial^2 p}{\partial \tau^2} + \frac{\beta p}{\rho_0 c_0^3}\frac{\partial p}{\partial \tau} \tag{3.18}$$

where $\Delta_\perp p$ presents the diffraction effect of the transducer and depends on the transducer shape. The three terms in the right side of (3.18) stand for diffraction effect of the probe, the attenuation of the medium and the nonlinear distortion of the medium, respectively.

If the transducer is a circular single element transducer, as illustrated in Figure 3.2, then

$$\Delta_\perp p = \int_{-\infty}^{\tau} \left(\frac{\partial^2 p}{\partial r^2} + \frac{1}{r}\frac{\partial p}{\partial r}\right) d\tau' \tag{3.19}$$

where $r$ is the radius of the transducer.

If the transducer is a linear-array probe, as illustrated in Figure 3.3, then

$$\Delta_\perp p = \int_{-\infty}^{\tau} \left(\frac{\partial^2 p}{\partial x^2} + \frac{\partial^2 p}{\partial y^2}\right) d\tau' \tag{3.20}$$

The geometrical parameters of linear-array probes, which are important for the diffraction effect, are described in Figure 3.4 and listed below:

- $N_{ele}$: number of elements of the transducer
- $Width$: width of the element in the lateral direction $x$
- $Height$: height of the element in the elevation direction $y$
- $Kerf$: spacing between two consecutive elements
- $Pitch$: distance between the center of two consecutive elements

Figure 3.2 Single element transducer

Figure 3.3 Linear array probe.

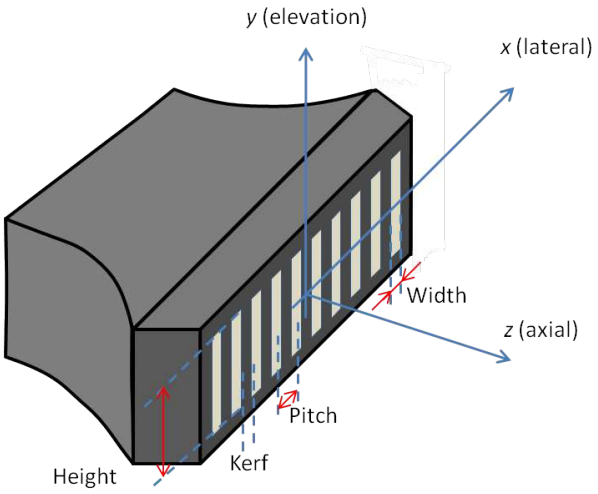


Figure 3.4 Geometrical description of the linear array probe

## 3.4 Simulators

Coupling with the study to nonlinear ultrasound propagation, various simulation tools have been developed. In this section, two simulators, used in this thesis, are introduced.

### 3.4.1 Voormolen simulator

The Voormolen is a nonlinear ultrasound propagation simulator, using a time domain algorithm as solution to KZK equation, for rectangular array with arbitrary excitation [Voormolen (2007)]. The impact of the different dimension of the array is taken into account. The different effects are solved with a finite difference scheme.

The time domain solution proposes a higher order in nonlinear interaction but needs a long computation time to converge to the solution. In order to decrease the computation time, the steps in the propagation direction are not equal, because more accuracy is required in the near field.

### 3.4.2 CREANUIS

CREANUIS is a tool that simulates nonlinear radio frequency (RF) ultrasound images containing both the fundamental and the second-harmonic evolution [Varray *et al.* (2013)]. It is the combination of two specific tools. The first tool is a nonlinear ultrasound propagation simulator that allows computing the increase of the fundamental and second-harmonic wave [Varray *et al.* (2011)]. The second tool is a reconstruction algorithm, using this field information and creating the corresponding nonlinear radio frequency (RF) image [Varray *et al.* (2010)].

For the nonlinear ultrasound propagation simulator, a generalized angular spectrum method (GASM) is used, so medium with an inhomogeneous nonlinear coefficient can be simulated.

## 3.5 Conclusion

In this chapter, the theoretical background about nonlinear wave propagation in biological tissue is mainly introduced. The development of new imaging techniques requires realistic conditions for simulated data. This chapter also shows that several tools can be used to simulate biological tissue when the nonlinearity of the medium is concerned.

# III. CONTRIBUTION

# Chapter 4

## Generalization of multi-pulse transmission

### Contents

In order to increase the contrast-to-tissue ratio (CTR) in contrast imaging or the signal-to-noise ratio (SNR) in tissue harmonic imaging, many multi-pulse transmission techniques have been proposed. This chapter presents a mathematical background to generalize most of the multi-pulse ultrasound imaging techniques. The presented formulation can be used to predict the nonlinear components in each frequency band. Simulation results on several multi-pulse techniques agree with the results given in previous literatures.

This chapter is the work presented in the journal article submitted to *Ultrasonics* [Lin *et al*., 2013b].

## 4.1 Introduction

Ultrasound echography is now widely used for the diagnosis of many diseases because it is non-invasive, simple to implement and relatively low cost compared to other modalities. In conventional imaging, the amplitudes of the reflected echoes are detected and used to form a B-mode image. Following the use of ultrasound contrast agents (UCA), diverse imaging techniques appear. UCA are suspensions of micro-bubbles injected intravenously and pass through the lung capillary circulation. They are stable enough to avoid rapid disappearance. Most of them have diameters less than 10 μm. UCA are used to enhance the backscattered signal from the blood pool [Gramiak *et al.* (1968)]. It was found that bubbles also backscattered harmonics because they vibrated asymmetrically (expanding much more than compressing) when exposed to an ultrasound pulse [De Jong *et al.* (1994a), (1994b)]. Previously, tissue was considered as a linear reflector, especially under low acoustic power, so it was natural to adopt harmonic imaging, which filters out the harmonics of UCA, to observe the behaviour of blood flow in large vessels and myocardial and tumour perfusion, in contrast imaging [Porter *et al.* (2010)]. Second-harmonic imaging is the most common imaging used [Burns *et al.* (1992), (1996)].

Unfortunately, tissue can also generate harmonics because the transmitted wave is deformed gradually during its propagation in tissue [Aanonsen *et al.* (1984)]. Therefore, in ultrasound contrast imaging, the contrast-to-tissue ratio (CTR) is limited because of tissue-generated harmonics. CTR is used to quantify the extent of discrimination between UCA and tissue and can be defined at a specified $m^{th}$ harmonic:

$$CTR_m = 20log\frac{P_m^{UCA}}{P_m^{tissue}} \tag{4.1}$$

where $P_m^{UCA}$ and $P_m^{tissue}$ are backscattered pressures of the $m^{th}$ harmonic from UCA and tissue, respectively.

In the other hand, harmonic imaging can be applied to tissue only, without injecting UCA, in order to improve resolution [Ward *et al.* (1997)], to increase the signal-to-

noise ratio (SNR) and to reduce artefacts. This technique is called tissue harmonic imaging [Bouakaz *et al.* (2003); Shen *et al.* (2007a), (2011)].

Besides the common criteria to judge the imaging quality of an ultrasound imaging technique, such as higher image resolution and fewer image artefacts, CTR is the main parameter in contrast imaging, and SNR in tissue harmonic imaging without UCA. Equation (4.1) claims that, to increase CTR in contrast imaging, the echoes generated by tissue should be reduced and those produced by UCA should be enhanced. In tissue harmonic imaging, conversely, the harmonic echoes from tissue should be enhanced while the other signals should be decreased.

### 4.1.1 Single-pulse techniques

Conventional B-mode imaging and second-harmonic imaging, including contrast harmonic imaging and tissue harmonic imaging, use a single-pulse transmission. In addition to these approaches, Forsberg *et al.* proposed sub-harmonic imaging by receiving at half of the transmitted frequency to increase CTR [Forsberg *et al.* (2000)]. Bouakaz *et al.* proposed super-harmonic imaging, transmitting at low frequency (0.8 MHz) and taking advantage of combined harmonics higher than third harmonics (third, fourth, fifth, …), termed super-harmonics, to increase CTR [Bouakaz *et al.* (2002)]. This method can also be used to image native tissue by transmitting at a higher frequency (1.2 MHz) to increase SNR [Bouakaz *et al.* (2003)].

Besides these techniques, several groups used the idea of source prebiasing to increase $CTR_2$ by suppressing the second harmonic generated by tissue. The difference between these techniques lies in how the source prebiasing signal is designed. Krishnan *et al.* predicted the waveform at the focus and the source prebiasing signal is the inversion of the obtained second-harmonic signal mixed with the imaging pulse [S Krishnan *et al.* (1996), (1998); Christopher (1999); KB Krishnan *et al.* (2008)]. This method was named the harmonic cancellation system (HCS). However, the tissue harmonic is reduced over a narrow band and a limited range of axial field. Pasovic *et al.* eliminated this disadvantage by defining a multiple-frequency component second-harmonic prebiasing signal [Pasovic *et al.* (2010)]; this technique is called multiple-component second-harmonic reduction signal (mcSHRS).

Shen *et al.* proposed transmitting a fundamental and a phase-shifted third harmonic wave simultaneously. The second harmonic is decreased when the frequency-sum component and the frequency-difference component are out of phase. When the two components are in phase, the second harmonic is enhanced. Therefore, this technique can be used in contrast imaging as well as in tissue harmonic imaging [Shen *et al.* (2007b), (2008b)]. These authors also suggested using the harmonic leakage signal to generate the second-harmonic reduction signal [Shen *et al.* (2008a), (2010)].

### 4.1.2 Multi-pulse techniques

However, in conventional harmonic imaging, the following problem is always encountered: if a short pulse, that is a broadband pulse, is transmitted, there is an inevitable spectral overlap between the fundamental and harmonic frequencies. To increase the sensitivity of the system in detecting harmonic echoes, a multiple-cycle pulse, that is a narrowband pulse, has to be transmitted, which unfortunately causes the a deterioration of the imaging resolution [Frinking *et al.* (2000); Chiao *et al.* (2003)].

To overcome the trade-off between contrast detectability and imaging resolution in conventional harmonic imaging and to further explore the specific ultrasonic properties of micro-bubbles as well as those of tissue, many multi-pulse techniques have been developed. Most of them modulate the transmission and reception frequency, pulse amplitude, pulse phase, pulse duration, number of pulses, pulse repetition frequency (PRF) and so on.

In pulse inversion (PI), a sequence of two inverted pulses is transmitted [Hwang (1999); Simpson *et al.* (1999)]. For a linear system, the response to the second pulse is an inverted copy of the response to the first one and the sum of the two responses is zero. For a non-linear system, the sum is not zero. Pulse inversion works over the entire bandwidth of the received echo signal and achieves better image resolution.

To suppress tissue harmonics in contrast imaging, Couture *et al.* developed PI using time reversal [Couture *et al.* (2008)]. The backscattered echoes from two inverted pulses were time-reversed and then used as excitation pulses. The echoes received from the new excitation signals were summed to form an image. Pasovic *et al.* proposed a method called second-harmonic inversion (SHI)[1] [Pasovic *et al.* (2011)]. As in PI, a sequence of two pulses is transmitted and the two responses are summed, but the phase shift between the two transmitted pulses is 90°. Because the second-harmonic component has a quadratic relationship to the fundamental one, the phase shift between the two second-harmonic components is 180°, so the second harmonic is cancelled successfully in tissue. In the contrast agent region, good preservation of the second harmonic was observed (maximum reduction was only 0.3 dB), therefore, the CTR is effectively increased. The preservation of the second harmonic was explained when Morgan observed that the signals reflected from a single bubble excited by two inverted one-cycle pulses have frequency shift and that the polarity of the two echoes received is not significantly changed [Morgan *et al.* (1998)].

[1] SHI refers to second-harmonic imaging, sub-harmonic imaging [Forsberg *et al.* (2000)], super-harmonic imaging [Bouakaz *et al.* (2002)] or second-harmonic inversion [Pasovic *et al.* (2011)] in different literatures.

There are also several methods to increase the non-linear response of microbubbles. Borsboom *et al.* proposed a method called pulse subtraction time delay imaging. Three pulses were transmitted. The third pulse emitted was the juxtaposition of the first two non-overlapping pulses. The echoes from the first two pulses were subtracted from the echo from the third pulse [Borsboom *et al.* (2009)]. Brock-Fisher *et al.* used a modulation in amplitude (AM) [Brock-Fisher *et al.* (1996)]. The linear echoes were cancelled but the odd nonlinear components were preserved. The combination of phase and amplitude modulation in a more generalized non-linear detection process was first suggested by Haider and Chiao [Haider *et al.* (1999)]. Phillips further evaluated this idea for three different UCA with several sequences called contrast pulse sequences (CPS) [PJ Phillips (2001); P Phillips *et al.* (2004)]. Eckersley *et al.* [Eckersley *et al.* (2005)] combined PI and AM where the second pulse was inverted and its amplitude was half that of the first pulse. The response to the second pulse was multiplied by two before being summed with the response to the first pulse. CTR was enhanced by 4±1 dB. Wilkening *et al.* transmitted five pulses with equidistant phases, a weighted summation of the received echoes suppressed the selected harmonics [Wilkening *et al.* (2000), (2001)].

There are also some multi-pulse techniques using different threads. Frinking *et al.* transmitted identical imaging pulses separated by a release burst which partially destroyed the UCA. The presence of UCA was detected by correlating or subtracting the response of the imaging pulses before and after the release of free gas bubbles [Frinking *et al.* (2001)]. Reddy *et al.* also used pulse inversion to increase the response of bubbles by identifying the shape of the driving pulse with limited driving intensity [Reddy *et al.* (2002)]. A dual-pulse frequency-compounding (DPFC) method was proposed to reduce the ghost reflection artefacts in super-harmonic images. Each radio frequency (RF) line is the summation of the response from two transmissions with slightly different centre frequencies [Van Neer *et al.* (2011)].

To eliminate the non-linear components produced by capacitive micromachined ultrasonic transducers (CMUTs), Novell *et al.* proposed two methods: one of them transmits the inverse signal of the undesired harmonic component while the other uses the interaction between the fundamental component and the selected transmitted frequency component to cancel the undesired harmonic component [Novell *et al.* (2009)].

Besides the imaging techniques mentioned, Doppler techniques, used to measure the blood flow, can be considered as multi-pulse techniques. Conventional pulsed Doppler and colour Doppler techniques repeat the same pulse for each line to track the moving scatterers in a region of interest (ROI); the movement then represents blood velocity. Power Doppler displays the power of the Doppler signal instead of the flow velocity. The Doppler technique has also been combined with harmonic imaging

leading to harmonic power Doppler (HPD) [Burns *et al.* (1994)] in order to increase the detectability of bloods or combined with PI to give the technique called pulse inversion Doppler (PID) [Simpson *et al.* (1999)] to decrease tissue movement artefacts. The pulse subtraction Doppler (PSD) was developed to differentiate bubble motion from tissue motion [Mahue *et al.* (2011)].

This chapter aims to present a generalized mathematical background to generalize most of the multi-pulse techniques in ultrasound imaging. The formulation obtained fits with previously proposed techniques to increase or to decrease specified nonlinear components in a specified harmonic band. Simulation results are shown to verify the generalization of this formulation and demonstrate that most of the nonlinear imaging techniques can be generalized by this formulation. The organization of the chapter is as follows. Section 4.2 introduces the theoretical background. Examples of several techniques are presented using the proposed formulation. The simulation results of several multi-pulse transmission techniques are shown and discussed in Section 4.3, to verify the generalization of such a mathematical background for multi-pulse transmissions. Section 4.4 concludes this chapter.

## 4.2 Theory

### 4.2.1 Mathematical background

When a wave propagates in a non-linear medium, the wave is deformed gradually during the propagation because of the diffraction effect of the probe, the absorption of the medium and the non-linear distortion of the medium [Aanonsen *et al.* (1984)]. Assuming the transmitted acoustic wave is:

$$p_0(t) = P_0 e^{j\omega_0 t + \varphi_0} \tag{4.2}$$

where $p_0$ is the amplitude of the wave, $\omega_0$ is the angular frequency and $\varphi_0$ is the phase. The received wave $r(t)$ is modelled as the polynomial expansion of a basis waveform $q_0$ [Haider *et al.* (1999)]:

$$r(t) = a_1 q_0(t) + a_2 {q_0}^2(t) + \cdots + a_N {q_0}^N(t) = \sum_{n=1}^{N} a_n {q_0}^n(t) \tag{4.3}$$

where $q_0$ is the basis waveform for the nonlinear components, $a_n$ is the weight of the $n^{th}$-order nonlinear component, $N$ is the presumed model order. The expression of $a_n$ and $q_0$ are not detailed here. $a_n$ is a complex term depending on the medium (tissue or bubbles) and on the frequency and amplitude of the transmitted wave. The waveform $q_0$ also depends on the transmitted wave $p_0$. In a linear system, only $a_1$ would be nonzero.

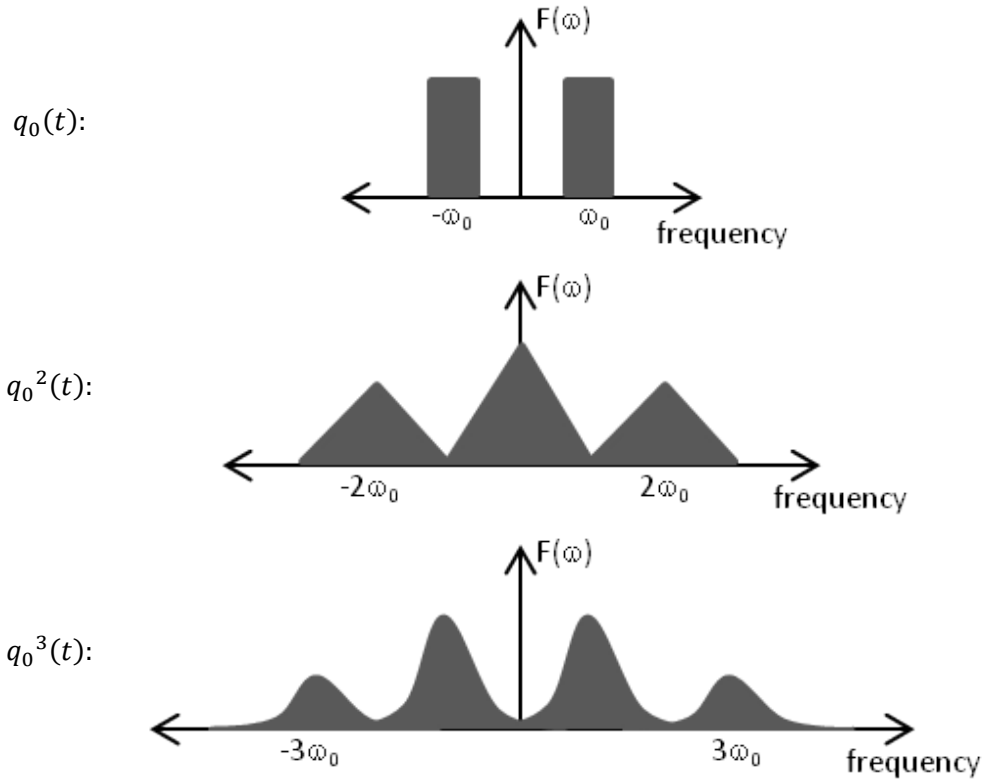


Figure 4.1 Demonstration of $n$-times auto-convolution of the spectrum of the linear term $q_0$ (after Haider *et al.* (1999)).

As Figure 4.1 shows, in the frequency domain, the time domain multiplication $q_0^n$ in Eq. (4.3) becomes $n$-times auto-convolution of the spectrum of the linear term $q_0$ (centred in $\omega_0$), this repeated convolution results in not only the spectrum component of the frequency band centred in $n\omega_0$, but also spectrum components of lower frequency band. In other words, the final signal level of the $n^{th}$ frequency band is decided by not only the $n^{th}$-order nonlinear component, but also the higher order nonlinear components. In general, odd-order nonlinear components in (4.3) create spectrum components at odd multiples of $\omega_0$, while even-order nonlinear components create spectral components at even multiples of $\omega_0$ [Haider *et al.* (1999); Eckersley *et al.* (2005)].

This property implies that the specific nonlinear component in one frequency band could be increased or decreased using multi-pulse transmission techniques. In multi-pulse transmission techniques, pulses are transmitted successively. Equation (4.2) is rewritten as the basic waveform of the transmitted pulses:

$$p_0(t) = P_0 e^{j\omega_0 t + \varphi_0} \tag{4.4}$$

Suppose $K$ pulses are transmitted into the medium and $b_k$ indicates the relationship between the $k^{th}$ transmitted pulse $p_k$ and the basic waveform $p_0$ [Haider *et al.* (1999)]:

$$p_k(t) = b_k P_0 e^{j\omega_0 t+\varphi_0} \tag{4.5}$$

$$b_k = |b_k| e^{j\varphi_k}, \quad \varphi_k \epsilon [0,2\pi], \quad k = 1,2,\dots,K \tag{4.6}$$

Then after propagating some distance in the medium and back-propagating to the probe, the pulses are received and multiplied by a weighting vector $c_k$ before being added together. The summation of these received pulses can be expressed as:

$$r_{sum}(t) = \sum_{k=1}^{K} c_k \left( \sum_{n=1}^{N} a_n b_k^n {q_0}^n(t) \right) \tag{4.7}$$

Equation (4.7) is the general expression of the sum of $K$ pulses propagating some distance and going back. The enhancement or cancellation of selective nonlinear components depends on the choice of coefficient vector $b$ and $c$:

$$b = (b_1, \dots, b_K) \tag{4.8}$$

$$c = (c_1, \dots, c_K) \tag{4.9}$$

To clearly see the dependence of each nonlinear components on the coefficient vector $b$ and $c$, (4.7) is written as:

$$r_{sum}(t) = \sum_{n=1}^{N} \left( \sum_{k=1}^{K} c_k b_k^n \right) a_n {q_0}^n(t) \tag{4.10}$$

so the weight of the $n^{th}$ nonlinear component in the final summed signal is:

$$\sum_{k=1}^{K} c_k b_k^n \tag{4.11}$$

These assumptions will be validated, in the latter part of this chapter, through the comparison between simulation results presented in this chapter and experimental results from previous literature.

### 4.2.2 Application to several multi-pulse techniques

In the following section, the formulation (4.10) is applied to several techniques presented in section 4.1. For simplicity and effective comparison, the first transmission and reception are regulated to be the same for all the following multi-pulse techniques, that is, $b_1 = c_1 = 1$. In all the cases presented in the present chapter, the fundamental and second-harmonic frequency bands are concerned, so only the linear component and third-order nonlinear component contributing to the fundamental band and the second-order nonlinear component contributing to the second-harmonic band are calculated, meaning that the presumed model order is $N = 3$.

#### *4.2.2.1 Pulse inversion (PI) and second harmonic inversion (SHI)*

For double-pulse transmissions such as PI and SHI, $\varphi_2$ defines the phase shift between the two transmitted pulses.

$$\begin{cases} b = \left(1, e^{j\varphi_2}\right) \\ c = (1,1) \end{cases} \tag{4.12}$$

For PI, $\varphi_2 = \pi$, substituting (4.12) into (4.10), the summation can be written as:

$$r_{sum}(t) = \sum_{n=1}^{N} \left(1 + e^{jn\pi}\right) a_n {q_0}^n(t) \tag{4.13}$$

Therefore, when $n$ is odd, $e^{jn\pi} = -1$; when $n$ is even, $e^{jn\pi} = 1$. That is, every odd nonlinear component is zero and every even nonlinear component doubles.

Similarly, for SHI [Pasovic *et al.* (2011)], $\varphi_2 = \frac{\pi}{2}$, so the summation (4.10) is:

$$r_{sum}(t) = \sum_{n=1}^{N} \left(1 + e^{jn\frac{\pi}{2}}\right) a_n {q_0}^n(t) \tag{4.14}$$

Therefore, when $n = 4i + 2$ $(i = 0,1,2 \ldots)$, $e^{jn\frac{\pi}{2}} = -1$. That is, every $(4i + 2)^{th}$ nonlinear component is zero.

#### *4.2.2.2 Amplitude modulation (AM)*

In the technique AM described by Brock-Fisher *et al.* [Brock-Fisher *et al.* (1996)], $b$ is a real vector.

$$\begin{cases} b = \left(1, \frac{1}{2}\right) \\ c = (1, -2) \end{cases} \tag{4.15}$$

substituting (4.15) into (4.10), the summation becomes:

$$r_{sum}(t) = \sum_{n=1}^{N} (1 - 2^{1-n}) a_n {q_0}^n(t) \tag{4.16}$$

Therefore, (4.16) becomes:

$$r_{sum}(t) = 0 + 0.5 a_2 {q_0}^2(t) + 0.75 a_3 {q_0}^3(t) \tag{4.17}$$

Equation (4.17) illustrates the linear component is cancelled in AM technique; the third-order nonlinear component, which also contributes to the signal level of the fundamental frequency band, becomes 0.75 times compared to one single transmission (refer to (4.3)) and the second-order nonlinear component becomes 0.5 times compared to one single transmission.

#### *4.2.2.3 Pulse inversion amplitude modulation (PIAM)*

In the technique proposed by Eckersley *et al.* [Eckersley *et al.* (2005)], the pulse inversion and amplitude modulation were combined.

$$\begin{cases} b = \left(1, \frac{e^{j\pi}}{2}\right) \\ c = (1,2) \end{cases} \tag{4.18}$$

substituting (4.18) into (4.10), the summation becomes:

$$r_{sum}(t) = \sum_{n=1}^{N} \left(1 + 2^{1-n} e^{jn\pi}\right) a_n {q_0}^n(t) \tag{4.19}$$

For $N = 3$, (4.19) becomes:

$$r_{sum}(t) = 0 + 1.5 a_2 {q_0}^2(t) + 0.75 a_3 {q_0}^3(t) \tag{4.20}$$

Compared to the AM technique, the linear component in PIAM technique is also cancelled; the third-order nonlinear component, which contributes to the signal level of the fundamental frequency band, remains the same; but the second-order nonlinear component is larger.

#### *4.2.2.4 Phase-coded sequences (PCS)*

For the phase-coded sequences (PCS) technique described in [Wilkening *et al.* (2000)], five transmissions with equidistant phases are transmitted. Subsets with three transmissions are investigated to cancel the linear component but to preserve the second-order and third-order nonlinear components in the fundamental frequency band. The parameters $b$ and $c$ for the three transmissions in the subsets are:

$$\begin{cases} b = \left(1, e^{j\frac{2\pi}{5}}, e^{-j\frac{2\pi}{5}}\right) \\ c = \left(1, -\dfrac{1}{2\cos\dfrac{2\pi}{5}}, -\dfrac{1}{2\cos\dfrac{2\pi}{5}}\right) \end{cases} \tag{4.21}$$

substituting (4.21) into (4.10),

$$r_{sum}(t) = \sum_{n=1}^{N} \left(1 - \frac{e^{j\frac{2n\pi}{5}} + e^{-j\frac{2n\pi}{5}}}{2\cos\frac{2\pi}{5}}\right) a_n {q_0}^n(t) \tag{4.22}$$

For $N = 3$, (4.22) becomes:

$$\begin{aligned} r_{sum}(t) &= 0 + \left[1 - \frac{\cos(4\pi/5)}{\cos(2\pi/5)}\right] a_2 {q_0}^2(t) + \left[1 - \frac{\cos(6\pi/5)}{\cos(2\pi/5)}\right] a_3 {q_0}^3(t) \\ &= 0 + 3.618 a_2 {q_0}^2(t) + 3.618 a_2 {q_0}^2(t) \end{aligned} \tag{4.23}$$

Equation (4.23) shows the linear component is also cancelled in PCS technique; the third-order nonlinear component, which also contributes to the signal level of the fundamental frequency band, becomes 3.618 times compared to one single transmission (refer to (4.3)) and the second-order nonlinear component also becomes 3.618 times compared to one single transmission.

#### *4.2.2.5 Contrast pulse sequences (CPS)*

In [PJ Phillips (2001)], eight groups of sequences called contrast pulse sequences were evaluated. For each group, selective nonlinear components are emphasized after the cooperation of $b$ and $c$. The eight sequences are listed in Table 4.1.

Considering the third sequence CPS3, for example,

$$\begin{cases} b = \left(1, \frac{e^{j\pi}}{2}, \frac{1}{2}, e^{j\pi}\right) \\ c = (1,2,-2,-1) \end{cases} \tag{4.24}$$

substituting (4.24) into (4.10),

$$r_{sum}(t) = \sum_{n=1}^{N} \left[(2^{1-n} - 1)\left(e^{jn\pi} - 1\right)\right] a_n {q_0}^n(t) \tag{4.25}$$

For $N = 3$, (4.25) becomes:

$$r_{sum}(t) = 0 + 0 + 1.5 a_3 {q_0}^3(t) \tag{4.26}$$

Therefore, the linear component and the second-order nonlinear component are cancelled while the third-order nonlinear component is 1.5 times compared to the single transmission (refer to (4.3)).

## 4.3 Simulations and discussions

To verify the generalization of the formulation, simulations for several multi-pulse techniques, namely SHI [Pasovic *et al.* (2011)], PI [Hwang (1999); Simpson *et al.* (1999)], AM [Brock-Fisher *et al.* (1996)], PIAM [Eckersley *et al.* (2005)], PCS [Wilkening *et al.* (2000)] and CPS [PJ Phillips (2001)], were conducted. Considering the experimental results have already been well presented in the mentioned literatures, only simulations were conducted. The validation of this mathematical background was done by comparing these simulation results with the previously published experimental results described in the literature.

A simulation tool, based on a finite difference method proposed by Voormolen to solve the KZK wave propagation equation, was used [Voormolen (2007)]. The harmonic images were computed with a delay and sum algorithm as proposed in CREANUIS software [Varray *et al.* (2010), (2013)]. The dimensions used for simulation of pressure field were listed in Table 4.1. UCA were considered as a non-linear medium with a higher coefficient of nonlinearity $\beta$ and a stronger reflectivity than tissue. The UCA region was simulated as a tube with a diameter of 8 mm and a tilt angle of 35°. The image depth was 100 mm. The tissue region was also considered as a non-linear medium, which is realistic, instead of a linear medium considered in most of the multi-pulse contrast imaging techniques.

The coefficient of nonlinearity $\beta$ of tissue and UCA were set according to the values of nonlinear parameter $B/A$ reported in previous literatures. The $B/A$ of the biological media was measured to be approximately in the range of 6 and 10 [Zhang *et al.* (1999), (2001)]. Then considering $\beta$ equals to $1 + B/2A$, $\beta$ value was from 4 to 6. The coefficient of nonlinearity $\beta$ of tissue was set as 4.5. The $B/A$ of two contrast agent (Albunex® and Levovist®) were measured to be an increasing function of bubble number densities [Wu *et al.* (1998)]. In our simulation, the coefficient of

nonlinearity of UCA was set as 51, that is, $B/A$ equals to 100, which corresponds to the nonlinear parameter of Levovist® with a concentration of about 1 mg/mL. For each reflector in the UCA region, the reflective echo was set to be ten times stronger than the reflector in the tissue region. Note that the values of $B/A$ and reflection coefficient vary with the microbubble type, the microbubble concentration and also the excitation frequency and pressure. However, in this chapter, we mainly focus on the evolution of $n^{th}$-order component in multi-pulse techniques, not on the exact amplitude of the frequency bands.

In order to simulate the situation close to the reality in medical use, pulses with Gaussian envelope were utilized for transmissions instead of the mono-frequency waves used in the theory. The transmitted frequency for all the transmitted pulses was 3 MHz, the transmission length was three cycles, the initial pressure $P_0$ of the basic pulse, described in (4.4), was 200 kPa. Based on the different strategies of the concerned techniques, the transmitted pressure and phases were set according to the parameter $b$, and the received RF data were weighted and summed according to the parameter $c$. To compare the CTR obtained from the different techniques, the parameters for the first transmissions of all the techniques were set to be exactly the same. That is, for all the techniques concerned, $b_1 = c_1 = 1$.

Figure 4.2 shows the images of PI, SHI, AM, PIAM, PCS and CPS3. The images of conventional B-mode imaging and second-harmonic imaging are also displayed for comparison. For the conventional second-harmonic image and SHI image, a sixth-order Butterworth bandpass filter was applied to the simulated RF data, with a frequency band from 5.4 MHz to 6.6 MHz. The images were normalized to the maximum amplitude of the one-pulse B mode image and log-compressed, with a dynamic range of 50 dB. Table 4.3 summarizes the average signal amplitudes of the ROI (within the blue lines) in UCA region, of the ROI (within the white lines) in tissue region and the CTR for each technique. The signal amplitudes in Table 4.3 were normalized to the averaged amplitude of the ROI in UCA region in one-pulse B image so that the CTR of the ROI in UCA region is 0 dB.

When only the UCA region is concerned, the comparison of Eq. (11), Eq. (15) and Eq. (18) can leads to the following observations: (1) the spectral amplitudes in the fundamental band for the three multi-pulse techniques (PI, AM, PIAM) are lower than the fundamental amplitude in the one-pulse image, because of the cancellation of the linear components, contributing to the fundamental bands, of the three multi-pulse techniques; (2) according to the coefficients of the second-order nonlinear components, the spectral amplitudes in the second harmonics band are ranked as follows: PI > PIAM > one-pulse > AM; (3) the fundamental spectral amplitude of PI keeps cancelled, because all the odd-order components, contributing to the fundamental band, are cancelled; (4) the fundamental spectral amplitudes of the AM

and PIAM are the same, because the resulting coefficient of the third-order components, contributing to the fundamental bands, of the two multi-pulse techniques are identical. Figure 4.2 shows the spectral analysis of the RF lines in the UCA region, from the one-pulse, PI, AM and PIAM images. Spectra were normalized to the maximum spectral amplitude of the one-pulse image. From the simulation results of Figure 4.3, it can be observed that the spectra agree with the observations expected from the theory. These simulations results are also in accordance with the published experimental results (Fig. 7 in [Eckersley *et al.* (2005)]). Therefore, the generalized equation is validated. This agreement confirms that a population of bubbles can be modelled as a nonlinear medium with a higher nonlinear value and a stronger reflection coefficient, if the pressure is low enough to avoid the cavitation.

In the previous paragraph, the spectral amplitudes of a single frequency band are compared. However, when several frequency bands are concerned, the comparison of the final signal level not only depends on the coefficient $\sum_{k=1}^{K} c_k b_k^n$ of each component, but also the contribution of each component $a_n {q_0}^n(t)$ itself. Therefore, the evolution of the spectral amplitude of a single frequency band for multi-pulse techniques cannot be directly observed from the image or the final signal amplitude in ROI as listed in Table 4.3.

In this chapter, tissue was simulated as a nonlinear medium. The resulting CTR is therefore different from the case when tissue was considered as linear medium. For example, in [Eckersley *et al.* (2005)], tissue was regarded as a linear medium, the CTR of PIAM was expected to be higher than that of AM because the amplitude of the signal in UCA-ROI in PIAM was measured and found to be higher than that in AM. From the first line of Table 4.3, we can see that the averaged amplitude in the UCA region increases from -8 dB in AM to 0 dB in PIAM. This means that our simulation results are in accordance with the results that the energy backscattered by UCA increases from AM to PIAM. However, the nonlinear response of tissue also increases, making the CTR of PIAM the same as the one of AM.

The SHI exhibits a lower CTR than that of the second-harmonic imaging instead of having higher CTR in [Pasovic *et al.* (2011)]. This is because in our simulation, UCA was simulated as a population of static scatterers. So although the second-harmonic signals in the tissue region were successfully reduced, the signals in the UCA region were also significantly reduced. The experimental results presented in [Pasovic *et al.* (2011)] show a combined effect of phase-shifted transmissions, bubble movements and bubble destruction. The present chapter is focused on the influence of multi-pulse transmissions, so the other effects are not considered here. However, in real life examinations, the UCA in the blood has a certain velocity and the influence of the movement of the UCA can become a positive or a negative factor to the effectiveness of a specific technique. Moreover, if the transmitted pressure is high, the UCA

bubbles can be destroyed. Therefore, these two effects will probably make the results differ from the predictions based on the generalized formulation. Note that if the bubble motion is shown, its influence could be introduced into the formulation to optimize some multi-pulse techniques [Lin *et al*., 2013a].

As expected, the speckle sizes of the resulting images from different techniques are different. This is due to the different resulting frequency band of the resulting signals. In addition, filtering is used for conventional second-harmonic imaging and SHI imaging while not used for the other techniques.

Table 4.1. Dimensions used for simulation of pressure field

| | |
|---|---|
| Number of active elements | 64 |
| Pitch | 320 μm |
| Kerf | 80 μm |
| Height | 12.5 mm |
| Elevation focus | 60 mm |
| TxFocus | 60 mm |

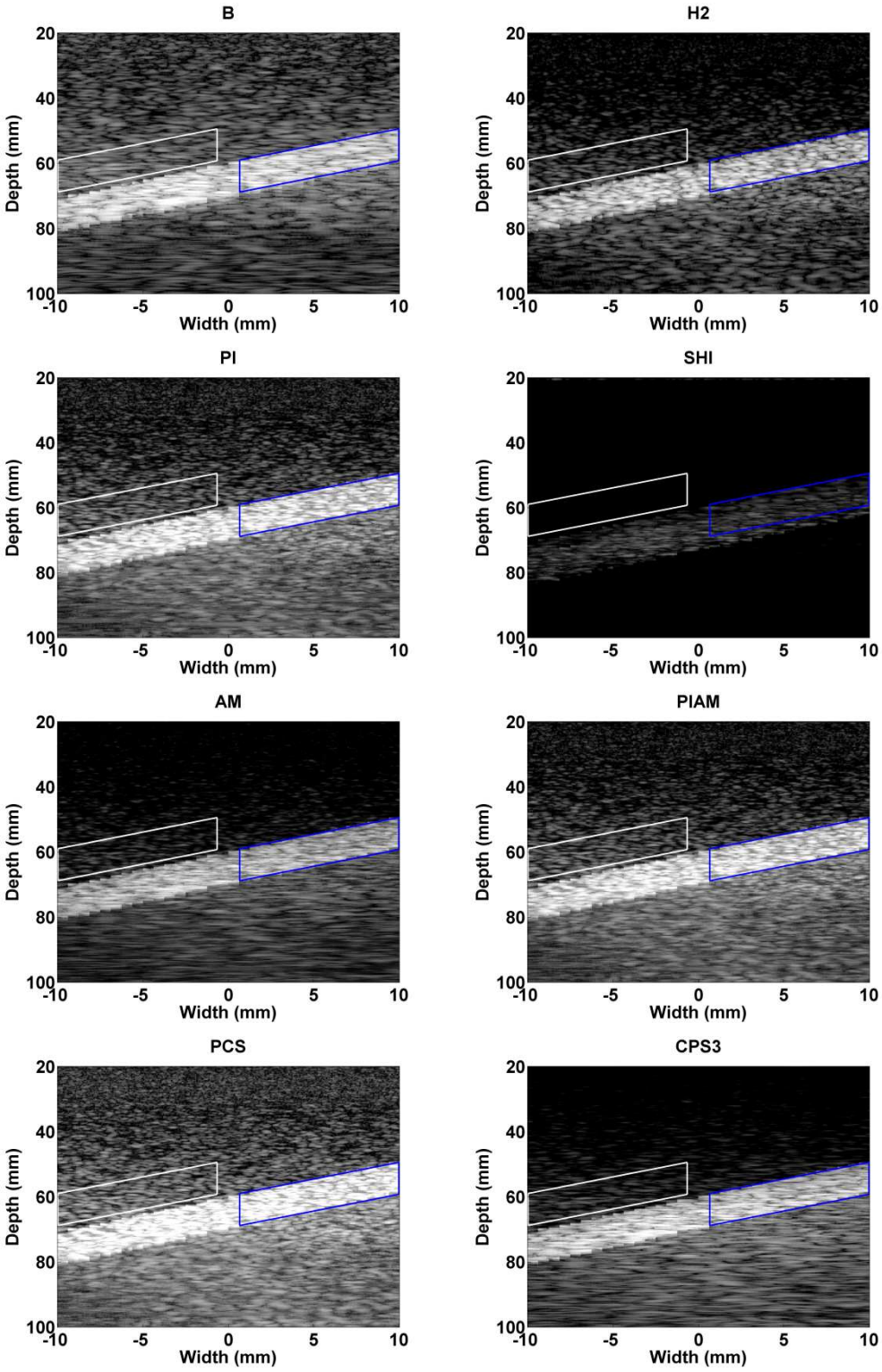


Figure 4.2 Resulting images for conventional B-mode (B), second-harmonic (H2), PI, SHI, AM, PIAM, PCS and CPS3. The dynamic range was 50 dB.

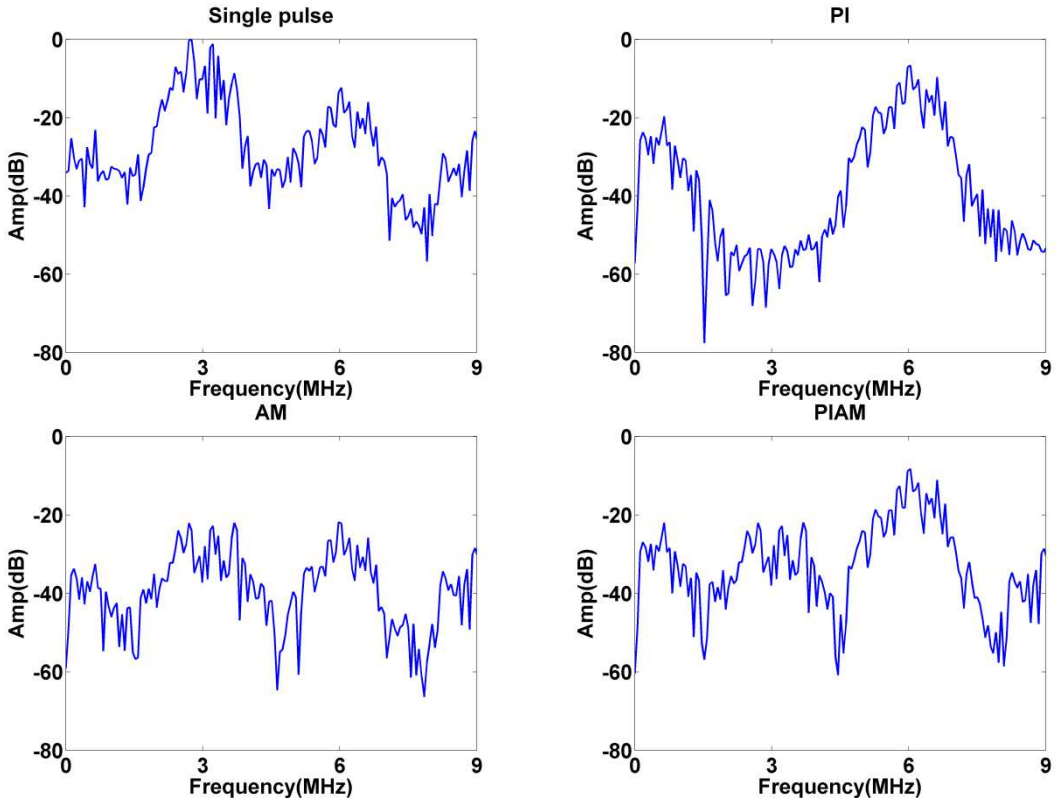


Figure 4.3 Spectral analysis of the RF lines in the UCA region, from the one-pulse, PI, AM and PIAM images, spectra were normalized to the maximum spectral amplitude of the one-pulse image.

Table 4.2. Weighting vectors $b$ and $c$ for CPS

| | $b$ | $c$ | Emphasized components |
|---|---|---|---|
| 1 | $\left(1, \frac{e^{j\pi}}{2}, \frac{1}{2}, e^{j\pi}\right)$ | $(1,8,-8,-1)$ | 1st |
| 2 | $\left(1, \frac{e^{j\pi}}{2}, \frac{1}{2}, e^{j\pi}\right)$ | $(1,2,2,1)$ | 2nd |
| 3 | $\left(1, \frac{e^{j\pi}}{2}, \frac{1}{2}, e^{j\pi}\right)$ | $(1,2,-2,-1)$ | 3rd |
| 4 | $\left(1, \frac{e^{j\pi}}{2}, \frac{1}{2}, e^{j\pi}\right)$ | $(1,0,0,1)$ | 2nd |
| 5 | $\left(1, \frac{e^{j\pi}}{2}, \frac{1}{2}, e^{j\pi}\right)$ | $(0,0,0,1)$ | All |
| 6 | $\left(1, \frac{e^{j\pi}}{2}, \frac{1}{2}\right)$ | $(1,1,1)$ | 2nd, 3rd |

| | | | |
|---|---|---|---|
| 7 | $(1, e^{j\pi}, 1)$ | (1,2,1) | $2^{nd}$ |
| 8 | (1,1,1) | $(1, -2, 1)$ | none |

Table 4.3 The CTR for each technique

| | B | H2 | PI | SHI | AM | PIAM | PCS | CPS3 |
|---|---|---|---|---|---|---|---|---|
| UCA (dB) | 0 | -6 | 1 | -32 | -8 | 0 | 6 | -4 |
| Tissue (dB) | -20 | -30 | -24 | -21 | -34 | -26 | -19 | -33 |
| CTR (dB) | 20 | 24 | 25 | 19 | 26 | 26 | 25 | 29 |

## 4.4 Conclusion

This chapter generalizes most of the multi-pulse transmission techniques used so far in ultrasound imaging. A generalized mathematical background has been presented. With the proposed formulations, the nonlinear components in each frequency band can be predicted for proposed techniques and the transmissions can be designed to increase or decrease specified components in a specified harmonic band.

Several multi-pulse techniques were simulated. The settings of the investigated medium and of the first transmissions for these simulations were the same. Therefore, the simulation results make it possible to observe and compare the results of different proposed techniques. For each technique, the evolution of the spectral amplitudes and CTR is focused on because they are the main criterion to evaluate the effectiveness of the ultrasound contrast imaging techniques.

The simulation results globally agree with the experimental results shown in the literature and the differences have been discussed. The results also show that none of the multi-pulse techniques that fit the generalized formulation can modify the signals in a given medium without altering the signals in the surrounding medium. Both UCA and tissue regions are modified simultaneously. So the final CTR results from a competition between the remaining signals from UCA and tissue, especially for cases where the nonlinear effect of tissue cannot be ignored.

The frequency of the multi-pulse transmission $\omega_0$ was considered as a constant value in the presented techniques. A more generalized formulation could be further extended to techniques with changing frequency such as multi-pulse transmission involving chirp excitations.

The formulation proposed constitutes a simple and relevant tool to imagine new multi-pulse techniques according to a specific objective.

# Chapter 5

## Influence of scatterer motion in multi-pulse techniques

## Contents

In ultrasound contrast imaging, many techniques based on multiple transmissions have been proposed to increase the contrast-to-tissue ratio (CTR). They are generally based on the response of static scatterers inside the imaged region. However, scatterer motion, for example in blood vessels, has an inevitable influence on multi-pulse techniques, which can either upgrade or degrade the technique involved. This chapter investigates the response of static nonlinear media insonated by multi-pulses with various phase shifts, and the influence of scatterer motion on multi-pulse techniques. Simulations, *in-vitro* experiments from a single bubble and clouds of bubbles, and *in-vivo* experiments from white rats show that the phase shift of the echoes backscattered from bubbles is dependent on the transmissions' phase shift, and that the bubble motion influences the efficiency of multi-pulse techniques: fundamental and second-harmonic amplitudes of the summed signal change periodically, exhibiting maximum or minimum values, according to scatterer motion. Furthermore, experimental results based on the second-harmonic inversion (SHI) technique reveal that bubble motion can be taken into account to regulate the pulse repetition frequency (PRF). With the optimal PRF, the CTR of SHI images can be improved compared to second-harmonic images.

This chapter is an extension of the work presented in the paper accepted for publication in the journal *IEEE UFFC* [Lin *et al*., 2013a] and in the conferences *IEEE IUS* [Lin *et al*., 2012b], *Acoustics 2012* [Lin *et al*., 2012a] and *Imageries du vivant* [Lin *et al*., 2012e].

## 5.1 Introduction

Ultrasound contrast agents (UCA) are suspensions of micro-bubbles injected into human blood vessels. They can pass through the lung capillary circulation and are stable, therefore increasing the bubble lifetime. Most of them have diameters less than 10 μm. The development of UCA was motivated at first by its high echogenicity and was used to enhance the backscattered signals from blood pool, leading to a better discrimination between blood and tissues [Gramiak *et al.* (1968)]. Then it was found that bubbles, if properly excited, also backscattered harmonics because of their nonlinear vibration [De Jong *et al.* (1994a), (1994b)]. If the tissues can be considered as linear reflectors, the harmonic imaging, which filters the harmonics of UCA, was naturally proposed to observe the behavior of blood. In particular, second-harmonic imaging remains the commonly adopted technique, in accordance with the limited bandwidth of traditional transducers.

However, it was observed that the transmitted wave is gradually deformed during the propagation in tissues and then also generates harmonics [Aanonsen *et al.* (1984)]. The tissues can be approximated to a linear system only when low acoustic pressures are taken into account. Therefore, the contrast-to-tissue ratio (CTR) is limited because

of the native tissue-generated harmonics. Equation (5.1) presents the definition of the $CTR_n$, used to quantify the extent of discrimination between UCA and tissues at a specific harmonic $n$:

$$CTR_n = 20log\frac{P_n^{UCA}}{P_n^{tissue}} \tag{5.1}$$

where $P_n^{UCA}$ and $P_n^{tissue}$ are backscattered pressures of $n^{th}$ harmonic from UCA and tissues, respectively.

Equation (5.1) claims that to increase CTR, the tissue response should be reduced and/or the bubble response should be enhanced.

To increase CTR, other harmonics instead of conventional second-harmonic have been used, such as in sub-harmonic imaging [Forsberg *et al.* (2000)] and in super-harmonic imaging [Bouakaz *et al.* (2002)]. Some techniques used the idea of source pre-biasing to increase $CTR_2$ by suppressing the tissue-generated second harmonics [S Krishnan *et al.* (1996), (1998); Christopher (1999); KB Krishnan *et al.* (2008); Pasovic *et al.* (2010)]. The differences among these techniques lie in how the source pre-biasing signal is designed. Shen *et al.* proposed a technique transmitting a fundamental and a phase-shifted third harmonic wave simultaneously to cancel second harmonic [Shen *et al.* (2007b), (2008b)]. The same group also used the harmonic leakage signal to produce the second-harmonic reduction signal [Shen *et al.* (2008a), (2010)].

All the methods mentioned above belong to single-pulse techniques, many multi-pulse techniques have also been proposed to increase CTR. The most common multi-pulse technique is called pulse inversion (PI) [Simpson *et al.* (1999)]. As explained in the previous chapter, a sequence of two inverted pulses is transmitted and the two received signals are summed. For a linear system (such as tissues insonified by low acoustic pressures), the response of the second pulse is an inverted copy of the response from the first pulse and the sum of the two pulses is zero. For a nonlinear system (such as bubbles and tissues insonified by high acoustic pressures), the sum is not zero. In fact, PI not only improves CTR, but also overcomes the trade-off of contrast detectability and imaging resolution [Frinking *et al.* (2000)]. However, in actual ultrasound systems, a second-harmonic band-pass filter is usually applied to remove the residual fundamental components.

Pasovic *et al.* proposed a multi-pulse method called second-harmonic inversion (SHI[2]) [Pasovic *et al.* (2011)]. Like in PI, a sequence of two pulses is transmitted and the two responses are summed, however the phase shift between the two transmitted pulses is 90°. Then the second harmonic is filtered to form a SHI image. Because the

[2] SHI doesn't refer to second-harmonic imaging, super-harmonic imaging or sub-harmonic imaging as used in some other literatures.

second-harmonic component has a quadratic relationship to the fundamental one, the phase shift between the two second-harmonic components is 180°, so the second harmonic of the summed signal is cancelled in tissues. In the UCA region, a preservation of second harmonic was observed (the maximum reduction was only 0.3 dB), therefore, the $CTR_2$ is effectively increased. The preservation of the second harmonic in UCA was explained, based on the observation of Morgan *et al.*, by the fact that the phase of reflected signals from a single bubble excited by two inverted single-cycle pulses was not significantly changed [Morgan *et al.* (1998)]. However, the preservation could be induced by the motion of the bubbles, considering that the UCA were always stirred during the acquisitions.

Besides PI and SHI, there are also several methods using multiple transmissions, which aim to increase the nonlinear response of micro-bubbles. These techniques have already been introduced in the previous chapter.

Nowadays, although lots of researches have done excellent works on estimating the models of a vibrating bubble [De Jong *et al.* (1992); Marmottant *et al.* (2005)] and the models of ultrasound propagation through contrast media [Tang *et al.* (2006)], few studies have been presented on the alteration of UCA backscattered signal according to phase-shifted transmissions. In fact, the literature reveals some conflicts: some authors believe that the phase of bubble-scattered echoes is not altered by a change in the phase of transmitted signal [Morgan *et al.* (1998); Pasovic *et al.* (2011)], while some others consider the phase of bubble-scattered echoes to be altered by the phase-shifted transmissions [Simpson *et al.* (1999); Eckersley *et al.* (2005)]. This point is of major importance for multi-pulse techniques.

Furthermore, all the multi-pulse techniques are influenced by scatterer motion during the pulse repetition interval (PRI). Note that the PRI is the reciprocal of the pulse repetition frequency ($PRI = 1/PRF$). Because the motion of the scatterers has the same effect as a phase shift, these motions can upgrade or degrade the involved techniques. Therefore, the quantification of the influence of moving UCA insonated by multi-pulses is interesting.

This chapter investigates not only the response of static nonlinear media insonated by multi-pulses with different phase shifts, but also the influence of scatterer motion to multi-pulse techniques. The chapter is organized as follows: section 5.2 introduces the theoretical background of nonlinear wave propagation and the influence of scatterer motion; section 5.3 presents the simulation results on a nonlinear medium with or without motion; section 5.4 presents the *in-vitro* experimental results on a static tissue-mimicking phantom, circulating UCA and a fluid phantom mimicking a vessel, respectively; section 5.5 presents the *in-vivo* experimental results on white rats; section 5.7 discusses several problems; and section 5.8 concludes this chapter.

## 5.2 Theory

### 5.2.1 Multi-pulse transmission with static scatterers

In multi-pulse transmission techniques, several waves are transmitted successively. Assuming the same basic waveform of the transmitted waves as in the previous chapter:

$$p_0(z=0,t) = P_0 \cos(\omega_0 t + \varphi_0) \tag{5.2}$$

where $P_0$ is the amplitude of the wave, $\omega_0$ is the angular frequency and $\varphi_0$ is the phase and $z$ is the propagation distance.

Suppose $N$ is the number of transmitted waves, $b^k$ is a complex parameter indicating the relationship between the $k^{th}$ transmitted wave and the basic waveform [Haider *et al.* (1999)]:

$$b^k = |b^k| e^{j\Delta\varphi^k}, \quad \Delta\varphi^k \epsilon [0,2\pi], \quad k = 1,2,\dots,N \tag{5.3}$$

So the pressure wave of the $k^{th}$ transmitted wave is therefore given as:

$$p^k(z=0,t) = |b^k| P_0 \cos(\omega_0 t + \varphi_0 + \Delta\varphi^k) \tag{5.4}$$

That is, the phase of the $k^{th}$ transmitted wave is:

$$\varphi^k = \varphi_0 + \Delta\varphi^k \tag{5.5}$$

After forward and back propagation of the pressure wave in the medium, because of the presence of harmonics either from nonlinear propagation or from nonlinear scattering of the bubbles, the received pressure wave is expressed as:

$$r^k(z=0,t) = \sum_{n=1}^{\infty} \alpha_n^k \cos\left(n(\omega_0 t + \varphi^k)\right) \tag{5.6}$$

where $\alpha_n^k$ is the amplitude of the $n^{th}$ harmonic. The expression of $\alpha_n^k$ is not detailed here. It is a complex term depending on the media (tissues or bubbles), and on the frequency and amplitude of the propagating wave. In our case, it can be assumed that: (i) for the $N$ phase-shifted waves transmitted with the same amplitude and frequency, and propagating in the same media, the value of $\alpha_n^k$ is the same; (ii) the phase shift of the $n^{th}$ harmonics of the received wave is $n$ times the transmitted phase shift. In the discussion part, these assumptions are compared with the experimental results.

In a multi-pulse technique, the imaging signal is a weighted sum of the received signals from the $N$ transmissions. $c^k$ is defined as the weighting factor for the received signal from the $k^{th}$ transmission. Then the summation of these received waves can be expressed as:

$$r_{sum}(z=0,t) = \sum_{k=1}^{N} \left( c^k \sum_{n=1}^{\infty} \alpha_n^k \cos\left(n(\omega_0 t + \varphi^k)\right) \right) \tag{5.7}$$

Equation (5.7) is the general expression of the weighted sum of $N$ pulses propagating in the medium and backscattered to the probe.

### 5.2.2 Influence of scatterer motion

In multi-pulse techniques, media motion is inevitable during PRI. Therefore for multi-pulse transmissions with low media motions in the direction of transmitted wave propagation, (5.4) can be written as:

$$p^k(z=0,t) = |b^k| P_0 \cos(\omega_0 t + \varphi_0 + \Delta\varphi^k + \theta^k) \tag{5.8}$$

where $\theta^k$ is the scatterer motion expressed as an additional phase shift of the transmitted wave:

$$\theta^k = \frac{4\pi\Delta z^k}{\lambda} \tag{5.9}$$

$\Delta z^k$ is the scatterer motion during the time interval between the first and $k^{th}$ transmitted wave. $\lambda$ is the wavelength of the transmitted waves. Assuming the velocity of the moving scatterers is $v$ and is constant,

$$\Delta z^k = (k-1)PRI \cdot v = (k-1)\frac{v}{PRF} \tag{5.10}$$

So the final effect depends on the combination of transmitted phase shifts and motions. The additional phase shift (5.9) becomes

$$\theta^k = (k-1)\frac{4\pi v}{\lambda \cdot PRF} \tag{5.11}$$

## 5.3 Simulation

To simulate the media response to transmitted pulses with various phase shifts and the influence of media motion to multi-pulse techniques, the simulator CREANUIS was used [Varray *et al.* (2013)]. This tool simulates nonlinear radio frequency (RF) ultrasound images containing both the fundamental and the second-harmonic evolution.

A collection of randomly distributed scatterers was simulated as a homogenous medium. The nonlinear coefficient $\beta$ of this medium was 4.5, corresponding to a typical biological medium [Zhang *et al.* (2001); Tortoli *et al.* (2009)].

The transmitted waves had a central frequency of 2 MHz, an initial pressure of 200 kPa and 4 cycles. The simulated aperture was 15.4 mm, the propagation depth was 80 mm and the focal depth was 70 mm. One RF frame consisting of several RF lines was created for each transmitted wave.

### 5.3.1 Static medium

In order to simulate static tissues, the positions of the scatterers within the medium were unchanged for all the simulations.

A series of ultrasound waves having phases $\varphi^k$ within the range of 0° to 360° were transmitted ($\varphi_0$ was set as 0° for simplicity). Every two RF frames from transmitted waves with increasing phase shifts were summed to provide one $RF_{sum}$ frame. To obtain the frequency spectra of $RF_{sum}$ frames, that is the averaged frequency spectrum of the RF lines consisted in the frame, the Fast Fourrier Transform (FFT) was applied. The spectrum amplitudes were normalized to the fundamental amplitude of a single pulse response. Figure 5.1 shows the fundamental and second-harmonic amplitude, averaged within a 20% bandwidth, of the spectra of the final $RF_{sum}$ frames versus increasing phase shifts.

In Figure 5.1, for the value of 0° phase shift, the fundamental and second harmonic amplitudes of the $RF_{sum}$ frame are the double of the amplitudes obtained from one single pulse, so there is an improvement of about 6 dB for both fundamental and second harmonic amplitudes. For the values of 180° phase shift, the fundamental is the minimum and the second harmonic is the maximum. This strategy corresponds to PI. For the values of 90° or 270° phase shift, the second harmonic passes through the minimum. It corresponds to SHI. To clearly describe PI and SHI and compare the two methods, the spectrum of the RF frame corresponding to one single transmitted pulse and that of the $RF_{sum}$ frame corresponding to two pulses with 90° or 180° phase shift are drawn together in Figure 5.2. In Figure 5.2, the fundamental amplitude of PI is reduced, while the second-harmonic amplitude is increased by 6 dB; the fundamental amplitude of SHI is increased by 3 dB, while the second-harmonic amplitude is reduced. Both Figure 5.1 and Figure 5.2 obviously show that PI reduces the fundamental frequency and emphasizes the second harmonic, while SHI reduces the second harmonic.

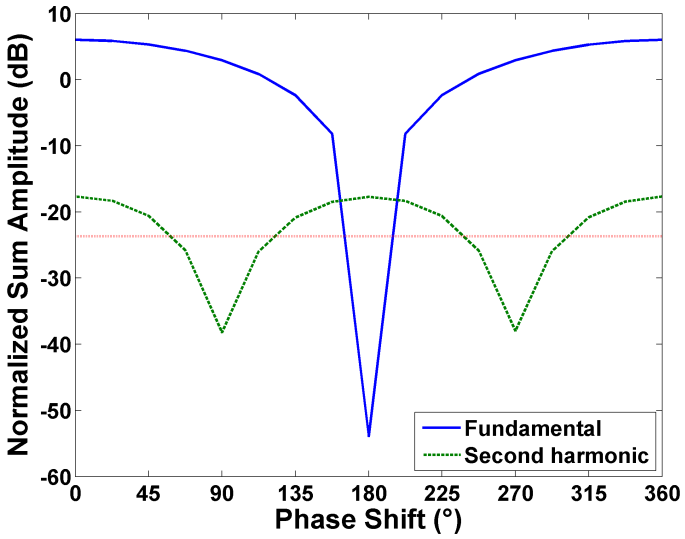


Figure 5.1 Simulated average fundamental (solid line) and second-harmonic (dashed line) amplitudes of $RF_{sum}$ frames versus transmitted phase shifts, obtained on a static medium. The $RF_{sum}$ frames were summed from two RF frames corresponding to two transmitted wave with phase shift ranging from 0° to 360°. The amplitudes were normalized to the averaged fundamental amplitude of a single pulse response. The dotted horizontal line is the amplitude of the second harmonic of one single pulse response.

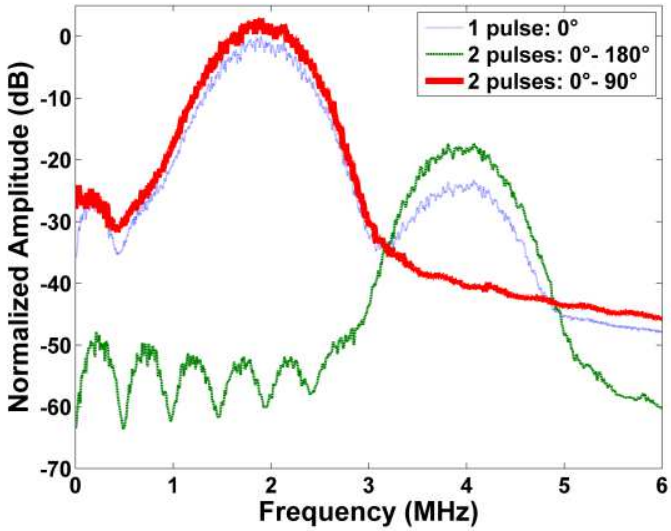


Figure 5.2 Spectra of the simulated single (dotted line) and summed RF frame corresponding to PI (thin line) or SHI (thick line), obtained on a static medium. The amplitudes were normalized to the maximum amplitude of a single pulse response.

### 5.3.2 Medium with motion

In this part, the influence of scatterer motion is investigated. For different simulations, the axial positions of scatterers were changed to simulate the scatterer motion in the wave propagation direction. The displacement profile was simulated as a rectangular pattern or a parabolic pattern (see Figure 5.3), and the mean displacement ranged from 0 to λ.

The RF frame corresponding to the pulse with 0° phase was firstly created, then the displacement of moving scatterers was set, and the second pulse with the phase of 90° or 180° was transmitted to create the second RF frame. After that, the two RF frames were summed as one $RF_{sum}$ frame. For each $RF_{sum}$ frame containing the mean displacement ranging from 0 to λ, the spectrum amplitudes were calculated as in the simulation part 5.3.1, except that these average RF spectra were calculated only for RF frame portion corresponding to the moving scatterers, instead of the whole frame as in simulation part 5.3.1.

Figure 5.4.a and Figure 5.4.b correspond to the simulations from rectangular displacement profile (see Figure 5.3.a). Figure 5.4.a presents the fundamental and second-harmonic amplitudes versus the increasing scatterer motion, corresponding to the two 180° phase-shifted transmissions, while Figure 5.4.b shows the results corresponding to the two 90° phase-shifted transmissions. These two curves demonstrate that the amplitudes oscillate with increasing scatterer motion. The oscillation period is 0.5 λ for fundamental frequency and 0.25 λ for the second harmonic.

In Figure 5.4.a, when there is no scatterer motion, the fundamental amplitude is minimum and the second-harmonic amplitude is maximum. When the scatterer motion is 0.25 λ, corresponding to an equivalent phase shift of 180°, both the fundamental and second-harmonic amplitudes are maximum. In Figure 5.4.b, the second harmonic amplitude in a one-pulse image is -24 dB. In a summed image, when no scatterer motion is applied, the second harmonic is reduced from -24 dB to -37 dB, meaning the second harmonic is reduced by about 13 dB. However, with a scatterer motion of 0.125 λ, the second harmonic is increased from -24 dB to -18 dB. That is, the second harmonic can be increased by about 6 dB with the scatterer motion, instead of being reduced with static scatterers.

To show a more realistic situation, a parabolic scatterer displacement profile, similar to the blood velocity profile in a vessel (see Figure 5.3.b)., was also simulated and the results are presented in Figure 5.4.c and Figure 5.4.d. These two curves also demonstrate that the amplitudes change periodically with increasing scatterer motion. However, for this parabolic profile, the period observed is 0.3 λ for fundamental frequency and 0.15 λ for the second harmonic. These simulation results deviate from the results of Figure 5.4.a and Figure 5.4.b, because the simulated displacements, in case of parabolic profile, varied in a range from zero to a maximum value in the

center. This variation leads to an optimal scatterer motion different from the theoretical results obtained with homogenous displacements. It is also observed that the extent of amplitude variation decreases with increasing scatterer motion, and finally the summed amplitude has a stable increase of 3 dB compared to the amplitude of a single pulse. This observation can be explained by the short signal transmitted (four-cycle pulsed waves) instead of continuous waves in theory. The summation of the two phase-shifted signals has a specific effect (PI or SHI) only on the superimposed signal portion. Therefore, when large scatterer motion is considered, the superimposed signal portions are small and the observed effects become ineffective. Theoretically, with four-cycle pulses, a scatterer motion equivalent to 2 $\lambda$ or more leads to two backscattered pulses having no common parts in their summation, and therefore PI or SHI effects cannot be observed. Then the power of the summed signal is twice the power of a single signal, so the amplitude of the summed signal is increased by a factor of $\sqrt{2}$ (or 3 dB) compared to a single signal.

Figure 5.1 and Figure 5.4 illustrate that the ultimate backscattered harmonic amplitudes are defined by two parameters: the phase shift of transmitted waves and the motion of scatterers. Therefore, the motion can be regarded as an additional phase shift to the original transmitted phase shift as described by equation (5.8) and (5.9). Note that the ultrasound imaging principle is based on the forward and backward propagation of the wave, so the value of scatterer motion should be doubled to be translated in a phase shift.

Figure 5.5.a is the simulated second-harmonic image. Figure 5.5.b presents the PI image with the moving scatterers, whose displacement profile is parabolic, within the width of −5 mm and 5 mm and static scatterers in the surrounding medium. These scatterers moved in the axial direction, and the displacement between the two frames involved in the PI image is 0.15 $\lambda$. This displacement in the central part corresponds to the maximum amplitude of the summed signal, while the static scatterers in the surrounding area cancel the fundamental amplitude (Figure 5.4.c). Figure 5.5.c presents the SHI image with a scatterer motion of 0.075 $\lambda$ in the central part and static scatterers all around. This displacement corresponds to the maximum second-harmonic amplitude of the summed signal, while the surrounding static scatterers result in a minimum second-harmonic amplitude (Figure 5.4.d). Both Figure 5.5.b and Figure 5.5.c show that the region with the scatterer motion is much brighter than the surroundings without scatterer motion.

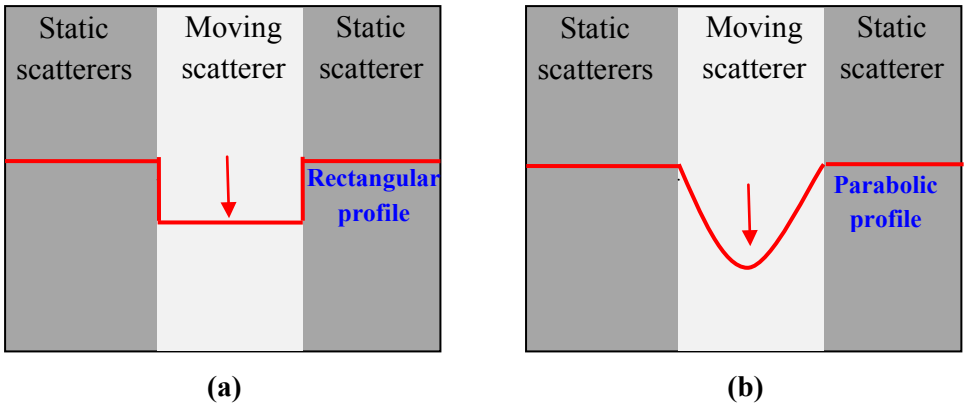


Figure 5.3 Schematic diagram of scatterer displacement profile: rectangular (a) or parabolic (b) pattern.

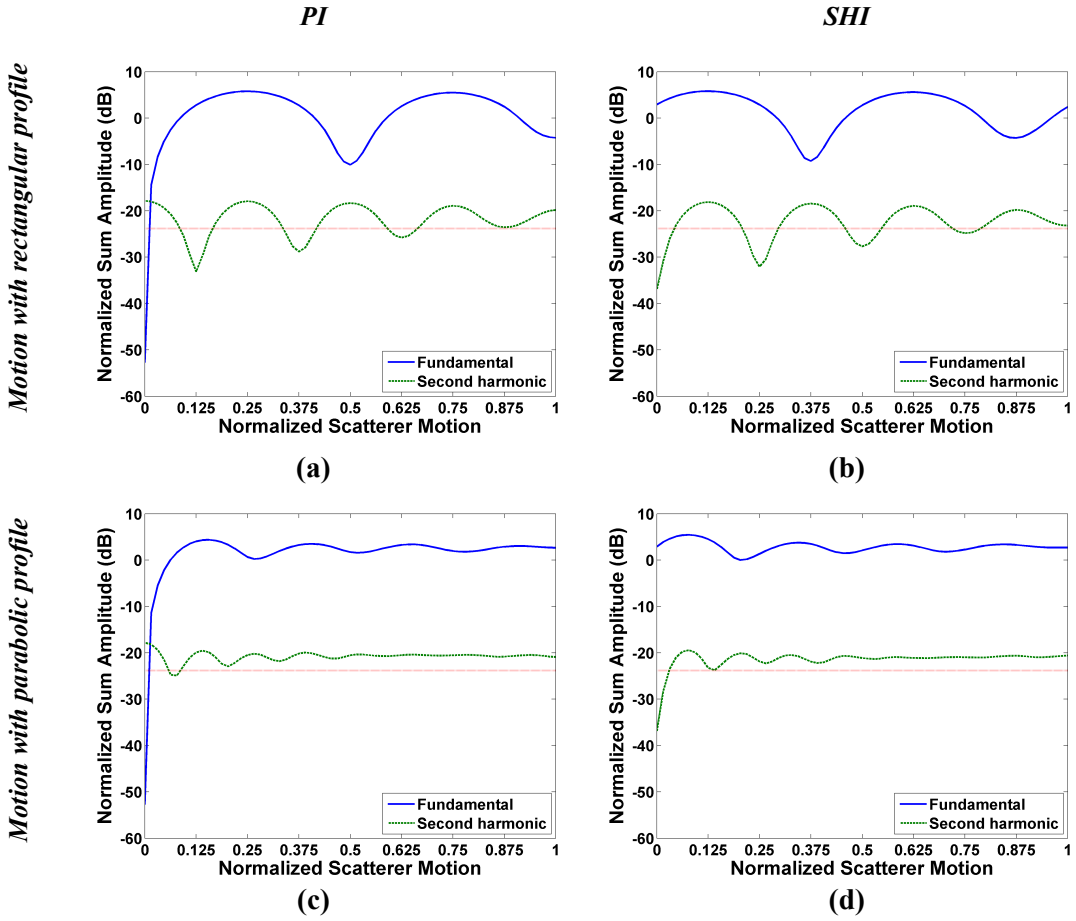


Figure 5.4 Simulated average fundamental amplitude (solid line) and second-harmonic amplitude (dashed line) of PI (a, c) or SHI (b, d) versus increasing scatterer motions (normalized to λ), obtained on a medium with moving scatterers. The motion profile was simulated as a rectangular pattern (a, b) or a parabolic pattern (c, d).The amplitudes were normalized to the averaged amplitude of a one-pulse

fundamental image. The horizontal dotted line was the amplitude of a one-pulse second-harmonic image.

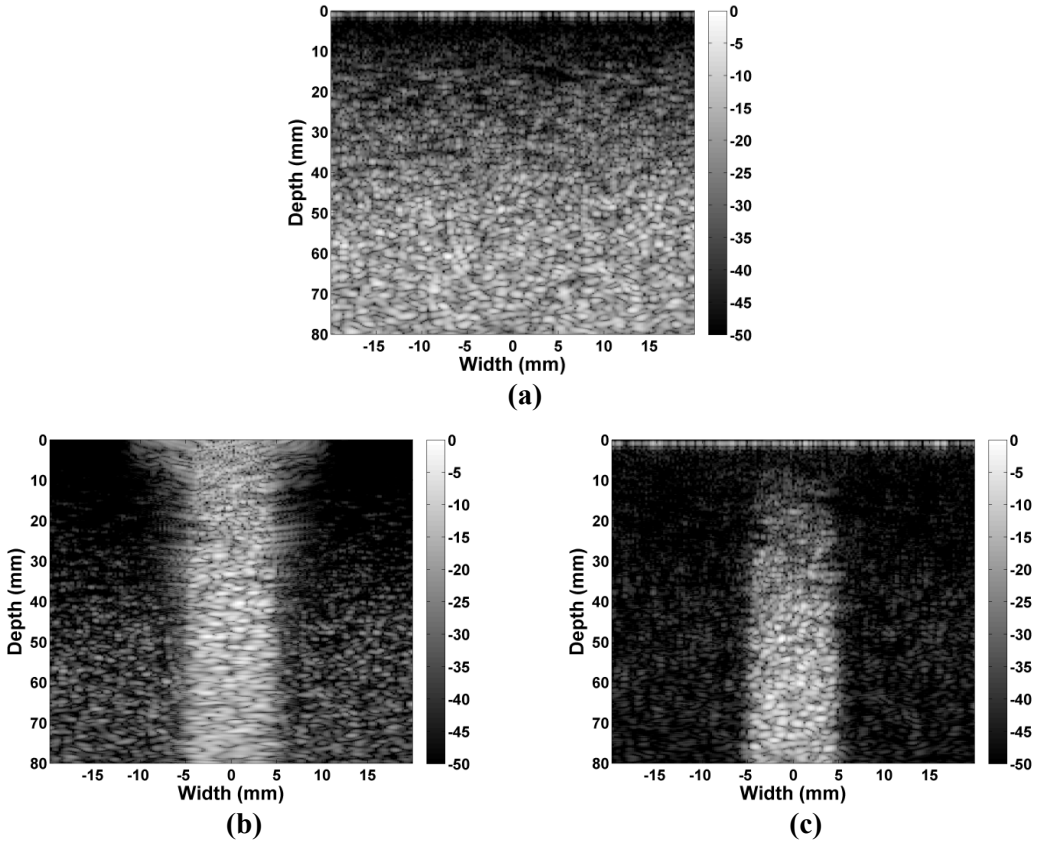


Figure 5.5 Simulated standard second-harmonic image (a), PI image (b) and SHI image (c) with axial scatterer motion within the width of −5 mm and 5 mm and static scatterers all around. In the central part of the images, the scatterer motion followed a parabolic profile, and the mean axial motion was 0.15 λ (c) or 0.075 λ (d). For the SHI image, an eight-order Butterworth filter with a bandwidth from 3.6 MHz to 4.4 MHz was used to filter the second harmonic.

## 5.4 *In-vitro* study

### 5.4.1 Tissue-mimicking phantoms

Experiments were first carried out on tissue-mimicking phantoms to validate the response of static nonlinear media insonated by multi-pulses with different phase shifts. The imaged tissue-mimicking phantom was made from 4% agar and 0.75% silice. The open ultrasound platform UlaOp (MSD Lab, Florence, Italy) equipped with the linear probe LA523 (Esaote, Italy) was used to transmit several pulses with various phases [Ricci *et al.* (2007); Tortoli *et al.* (2009)]. The probe has a 7 MHz central frequency and a -6 dB fractional bandwidth of about 100%. Transmitted pulses

were 5 MHz sine with Hanning envelope and 7 cycles. The focal point was set at 20 mm.

The two responses corresponding to transmitted pulses with a phase shift ranging from 0° to 180° were summed ($\varphi_0$ is set as 0° for simplicity). Figure 5.6 shows the averaged amplitudes of first and second-harmonic bands of the resulting signals versus increasing phase shifts. The averaged amplitudes were calculated as in the simulation 5.3.1.

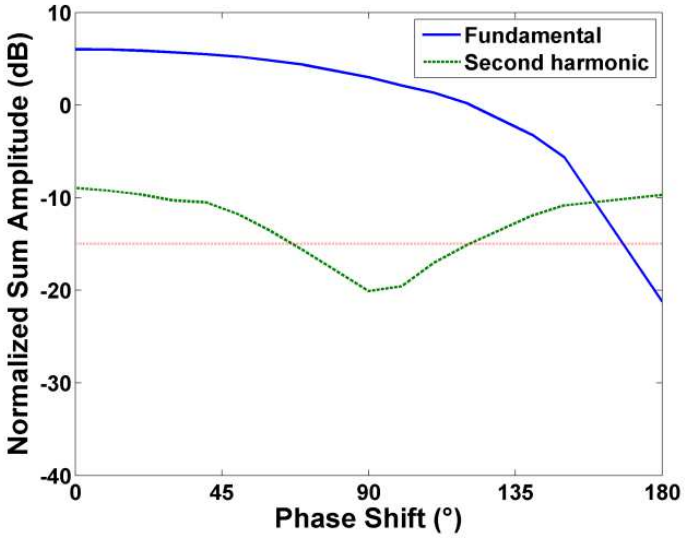


Figure 5.6 Experimental average fundamental (solid line) and second-harmonic (dashed line) amplitudes of summed RF signals versus increasing transmitted phase shifts, obtained on a tissue-mimicking phantom. The horizontal dotted line was the second-harmonic amplitude of one single pulse response. The summed RF signals came from two RF signals corresponding to two transmitted waves with different phase shifts ranging from 0° to 180°. The amplitudes were normalized to the averaged fundamental amplitude of a single pulse response.

The experimental results given in Figure 5.6 are in agreement with the simulation results shown in Figure 5.1: at 0° phase shift, both the fundamental- and second-harmonic amplitudes are increased by 6 dB; at 90° phase shift, the second-harmonic amplitude is reduced by 5 dB; at 180° phase shift, the fundamental amplitude is reduced by 21 dB. The extent of fundamental- and second-harmonic amplitude reductions depend on the amplitudes of the signals generated in tissues, which are mainly determined by the transmitted energy, the nonlinearity of the tissues and the depth of the ROI.

### 5.4.2 Circulating UCA bubbles

#### *5.4.2.1 Experimental setup and data post-processing*

To investigate the influence of scatterer motion in multi-pulse imaging techniques, experiments on circulating contrast agents were also carried out. Figure 5.7 shows the schematic diagram of the experimental setup: the net hydrostatic pressure due to the height difference forced a water flow from the water tank to the capillary fiber. The capillary fiber was made by regenerated cellulose and had an external diameter of 200 μm. The BR14 UCA bubbles (Bracco, Geneva, Switzerland), whose mean diameter is 3 μm, were injected with a syringe.

A single-element piezoelectric transducer, with a central frequency of 3 MHz, 70% fractional bandwidth and a focal distance of about 70 mm, was connected with a Bubble Behaviour Testing (BBT) controller (MSD lab, Florence, Italy) [Ricci *et al.* (2006)]. The BBT controller made it possible to transmit arbitrary waveforms, to record the signals backscattered from UCA and to set the PRF, the region of interest (ROI) and the storage data size. The transmitted signals were Tukey-windowed (0.1 tapering ratio) 10-cycle sine pulses with a central frequency of 2 MHz, 170 kPa peak negative pressures. For each transmitted wave, the RF signals backscattered from UCA were converted to 2048 digital samples with 14-bit resolution at a 64-MHz sampling rate. Pulses with 0° and 90° phases were transmitted alternately, and the received RF signals were stored. These RF data were used to investigate the relation of bubble motion and the second-harmonic amplitude of SHI.

In the experiments, to emulate different bubbles displacement between 90° phase-shifted transmissions, two transmission methods were implemented. The first method used different PRF, ranging from 0.01 kHz to 7.81 kHz. For each PRF, 2048 radio frequency (RF) signal lines were stored as one acquisition dataset. For each acquisition dataset, the successive two RF lines corresponding to two transmissions with the 90° phase shift were summed to be one SHI dataset. The second method used a single dataset acquired by constant PRF of 7.81 kHz. Various SHI datasets were then created, under-sampling the original sequence, by combining the RF line of one 0° transmission with the RF lines from different non-successive 90° transmissions. Figure 5.8.a and Figure 5.8.b summarize the two different process to obtain different SHI datasets. To avoid confusion with the PRI used during the acquisition, the time interval between the pulses used to get the SHI datasets is termed $PRI_{SHI}$.

After obtaining the SHI dataset, second-harmonic amplitudes were calculated in the frequency domain through the FFT. Figure 5.8.c presents the calculation process. The second-harmonic amplitudes of the two 90° phase-shifted RF data were calculated and averaged to give the classic second-harmonic amplitude. The second-harmonic amplitude of SHI was then normalized to the classic second-harmonic amplitude.

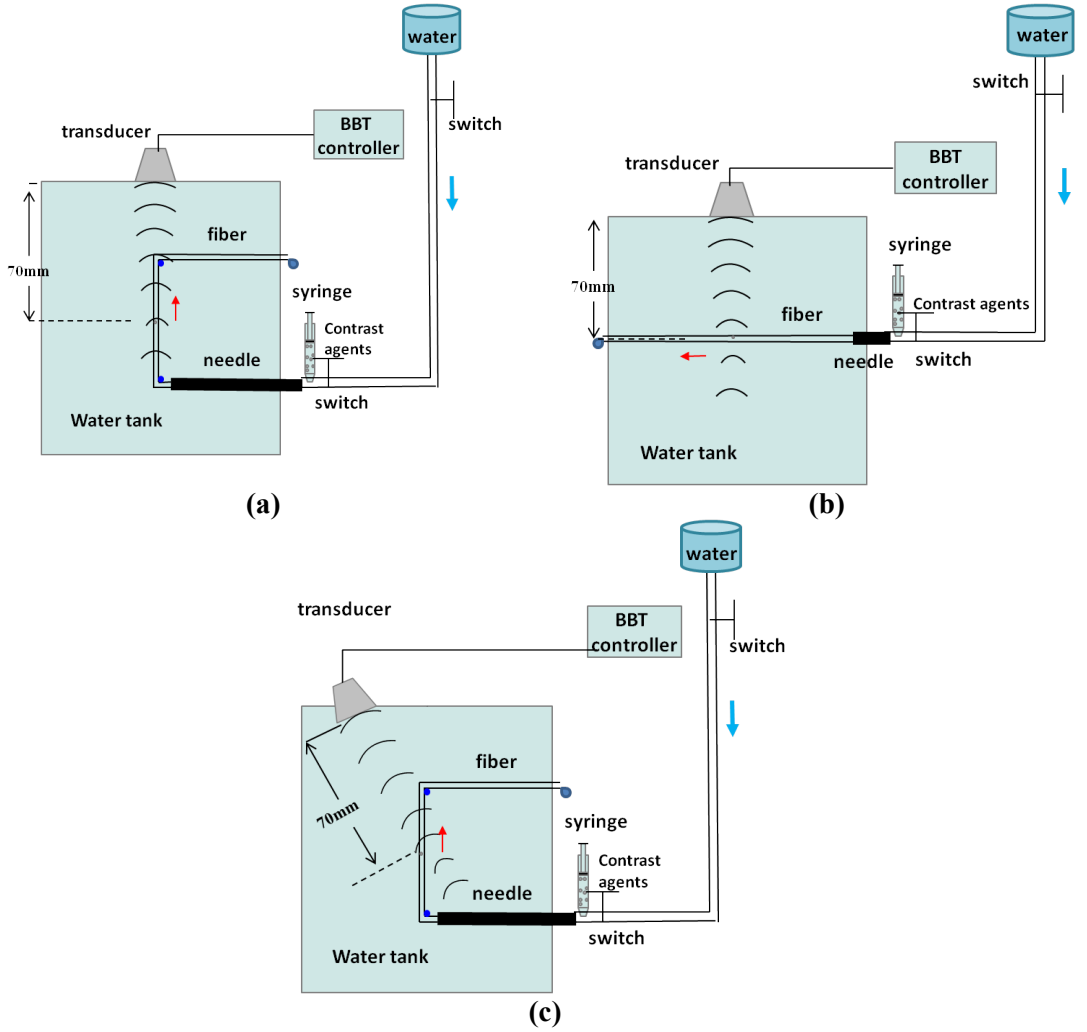


Figure 5.7 Schematic diagram of experimental setup using a single-element transducer: the hydrostatic pressure due to the height difference allows the circulation of UCA inside the fiber (200 μm diameter). Bubbles move in axial (a), lateral (b) and angled (c) direction. The BBT controller defined the transmitted pattern.

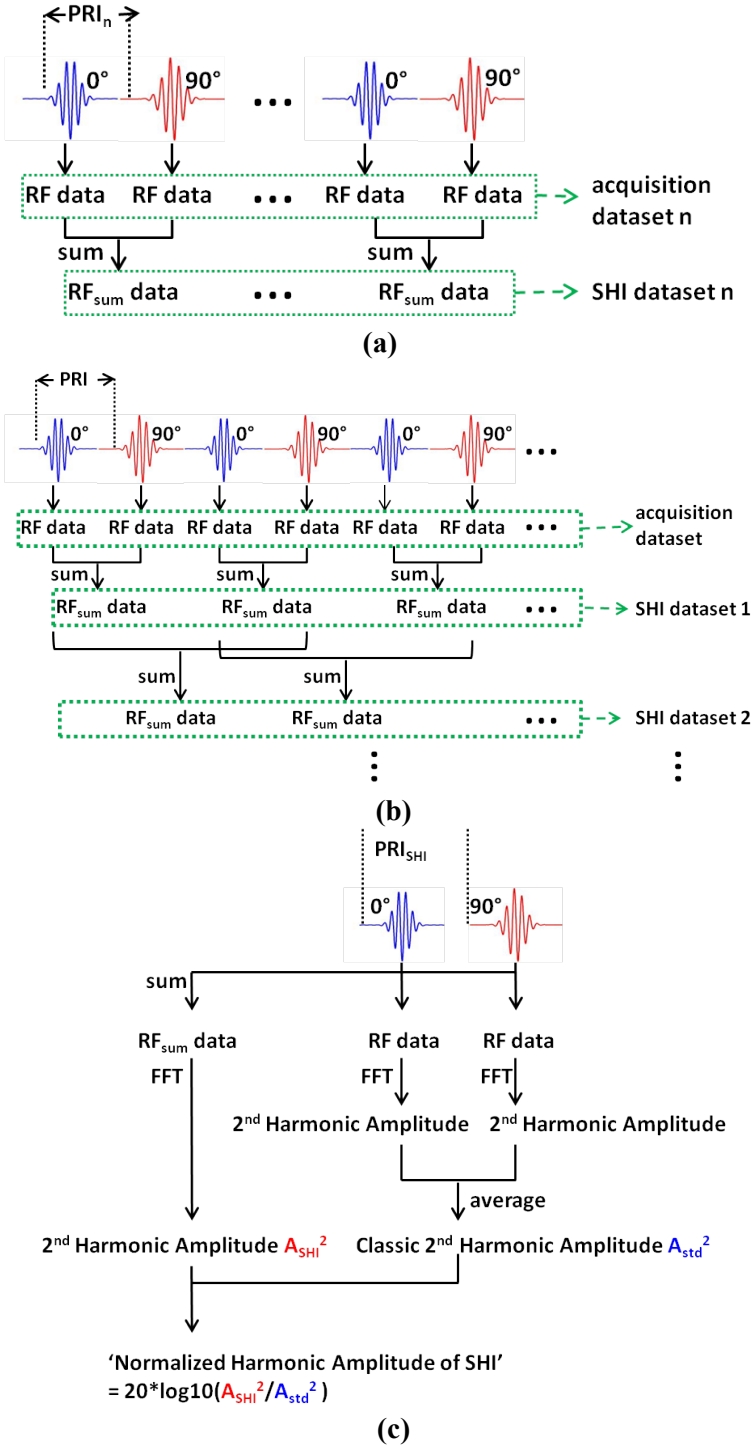


Figure 5.8 Schematic diagram of the post-processing for the experiments using a single-element transducer: (a) Different SHI datasets were obtained by successive RF data acquired with various PRF. (b) Different SHI datasets were obtained by combining non-successive RF data acquired with fixed PRF. (c) The calculation process of the second-harmonic amplitude of SHI.

### *5.4.2.2 Bubbles moving in axial direction*

In this section, the experimental results with axial bubbles motion are presented. Schematic diagram of the experimental setup was shown in Figure 5.7.a.

#### *5.4.2.2.1 With various PRF*

Figure 5.9 presents the averaged second-harmonic amplitudes of SHI versus PRI with PRF ranging from 0.01 kHz to 7.81 kHz (first method). The PRI was also translated to the ratio of bubbles motion to transmitted wavelength λ.

Figure 5.9 shows that the average second-harmonic amplitudes of SHI vary in the range from -8 dB to 4 dB with various PRI values. When PRI is less than 2 ms, the second-harmonic amplitudes of SHI increase with PRI. The SHI amplitude reaches maximum when PRI is 2 ms and decreases after 2 ms. Considering the second harmonic of tissues is always reduced under SHI strategy, the variation in bubbles second-harmonic amplitude of SHI with PRI means the effectiveness of SHI is greatly influenced by PRI.

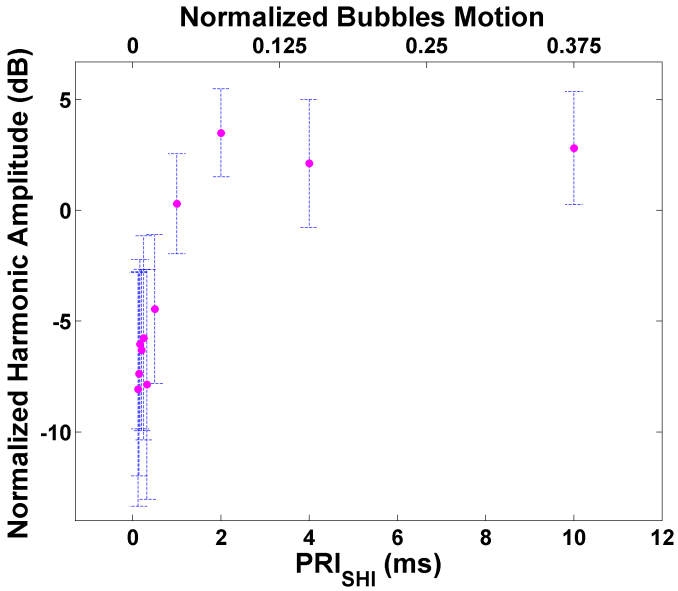


Figure 5.9 *In-vitro* experimental results from UCA moving in the axial direction obtained with first experimental method (PRF = 0.1 - 7.81 kHz): the normalized averaged second-harmonic amplitude of SHI versus PRI (lower axis) or versus the bubbles motion to transmitted wavelength ratio (upper axis).

Figure 5.9 has shown the dependence of multi-pulse technique effectiveness on the PRI. However, only the harmonic amplitudes corresponding to certain PRI values were acquired, to obtain the complete curve, more experimental points are needed. So the experiments with fixed PRF (refer to the second method described in section 5.4.2.1) were conducted, the results are presented in the following sections.

*5.4.2.2.2 With fixed PRF*

To obtain the response of a single bubble, the UCA was diluted to a low concentration (in the range of $4\times10^5$ and $7\times10^5$ microbubbles/mL). The very high sensitivity of the BBT system allows us to obtain the weak echo signal of a single event, and it is assumed that this single event comes from a single bubble (Figure 5.10). Figure 5.10.a presents the Hilbert transformation of the RF data (M-mode image) with 0° phase transmissions of a moving single bubble. The residual oscillations of the envelope come from the second harmonic present in the bubble echo. The bubble velocity was measured, from the slope of the straight lines on this M-mode image, to be 3.85 ± 0.02 cm/s. Figure 5.10.b presents the second-harmonic amplitude of SHI (normalized to the classic second-harmonic amplitude) versus $PRI_{SHI}$ from various SHI data sets. For each SHI data set, the average value and the standard deviation of the second-harmonic amplitudes are presented. The $PRI_{SHI}$ was also translated to the ratio of bubble motion to transmitted wavelength. Figure 5.10 clearly shows that the second-harmonic amplitude of SHI varies periodically with bubble motion, and the maximum value occurs when the bubble motion is 0.126 λ. Note that the theoretical maximum value is obtained with a displacement of λ/8 (or 0.125 λ).

The experimental results obtained on a population of circulating bubbles, with a concentration in the range of $4\times10^8$ and $7\times10^8$ microbubbles/mL, are shown in Figure 5.11. The maximum bubble velocity was measured to be 6.69 ± 0.3 cm/s from two different approaches (Doppler and water flow capacity measurements with the assumption of a parabolic flow). It should be noted that the bubbles velocity profile differs from the water velocity profile: it is found that bubbles behave like the red blood cells in a vessel [Keller *et al.* (1989)] having a velocity profile lightly flat, compared to the parabolic profile [Logean *et al.* (2003)]. Considering that the maximum velocity is the same for bubbles and water (as proved by the maximum Doppler shift measurements with bubbles), the mean bubble velocity is estimated to be between the mean velocity (3.35 ± 0.30 cm/s) and the maximum velocity (6.69 ± 0.30 cm/s) of the parabolic water flow. Figure 5.11 presents the second-harmonic amplitude of SHI (normalized to the classic second-harmonic amplitude) versus $PRI_{SHI}$ from various SHI data sets. For each SHI data set, the average value and the standard deviation of the second-harmonic amplitudes are presented. The $PRI_{SHI}$ was also translated to the ratio of bubble motion to transmitted wavelength. For this translation, the mean water flow velocity (3.35 cm/s, assuming a parabolic flow) was used.

The results show that the second-harmonic amplitude of SHI varies periodically with increasing $PRI_{SHI}$. The maximum averaged second-harmonic amplitude of SHI

is about 5 dB, and the minimum is about −7 dB at the beginning of the curve when a small motion is considered. So the difference of SHI amplitude reaches 12 dB. Furthermore, the amplitude is less than 0 dB when the $PRI_{SHI}$ is lower than about 0.04 λ and greater than 0 dB otherwise. These experimental results show that the effectiveness of SHI varies according to the bubble motion in the UCA region. Therefore, if the flow velocity is low, the PRF must be low enough and the $PRI_{SHI}$ high enough (higher than 0.04 λ according to this experiment) in order to guarantee an efficient SHI (second-harmonic amplitude of SHI in the region of moving bubbles greater than 0 dB).

The first cycle of the curve in Figure 5.11 ($PRI_{SHI}$ less than 0.18 λ) is the most important. At first, it corresponds to the lower $PRI_{SHI}$ values; therefore, the two backscattered signals used as the SHI pulses experience fewer transmitted pulses in between. Consequently, the resulting signals mainly reflect the influence of the bubble motion, rather than other influences coming from the transmissions. Secondly, in practical use, lower $PRI_{SHI}$ is preferred, under the premise of the same effectiveness, in order to shorten the image acquisition time.

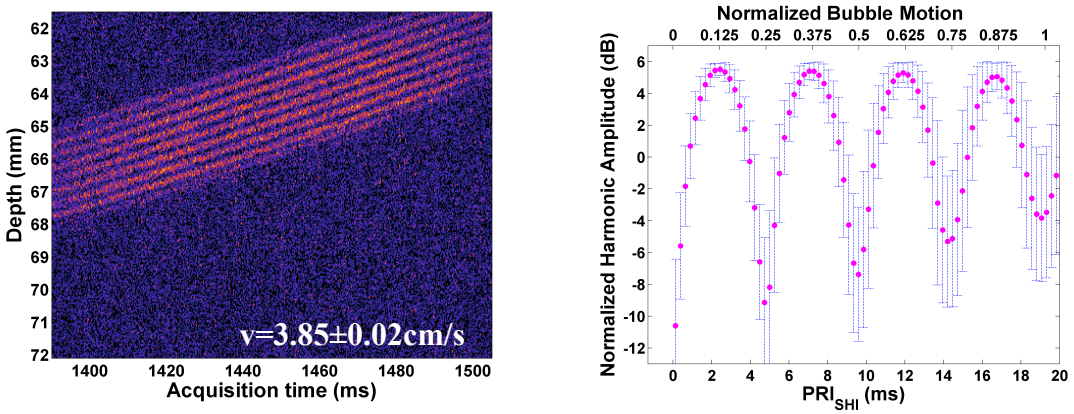


Figure 5.10 *In-vitro* experimental results from UCA moving in the axial direction obtained with second experimental method (PRF = 7.81 kHz): (a) M-mode image of a moving single bubble; (b) average (dots) and standard deviation (bars) of the second-harmonic amplitude of SHI (normalized to the classic second-harmonic amplitude and expressed in dB) versus PRI between two 90° phase-shifted pulses (lower axis) or versus the bubble motion, normalized to the transmitted wavelength (upper axis), obtained from the single bubble.

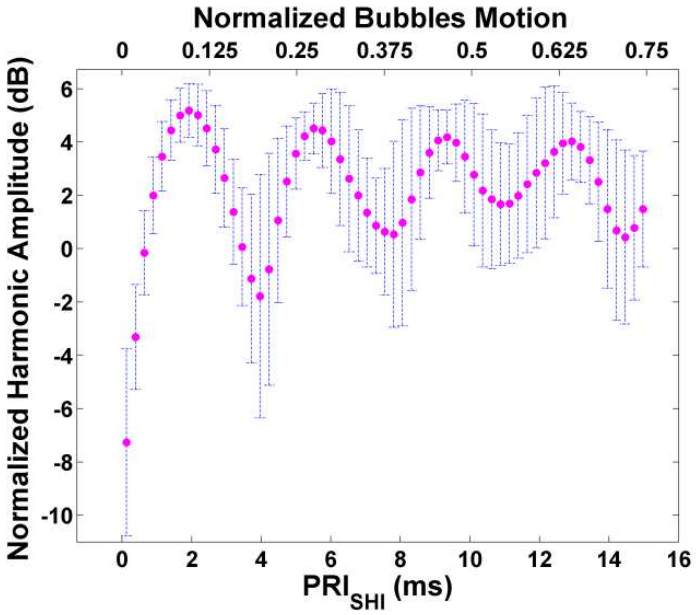


Figure 5.11 *In-vitro* experimental results from UCA moving in the axial direction obtained with second experimental method (PRF = 7.81 kHz): average (dots) and standard deviation (bars) of the second-harmonic amplitude of SHI (normalized to the classic second-harmonic amplitude and expressed in dB) versus PRI between two 90° phase shifted pulses (lower axis) or versus the bubbles motion, normalized to the transmitted wavelength (upper axis), obtained from a population of circulating bubbles.

In Figure 5.11, the maximum harmonic amplitude firstly appears when bubble motion is about 0.09 λ, while in theory the maximum harmonic amplitude should firstly appear when the bubble motion is 0.125 λ. This deviation comes from the fact that the mean water flow velocity was used to calculate the bubble displacement. Considering that the bubbles, like the red blood cells in a vessel, tend to have a higher velocity than the velocity described by a parabolic flow, when the bubbles are close to the fiber walls [Tangelder *et al.* (1986)], their real mean velocity would be greater than the mean water flow velocity and lower than the maximum water flow velocity. So the actual bubble motion should be within the range of 0.09 λ and 0.18 λ. These experimental results also agree with the simulation results of the parabolic pattern in the simulation section 5.3.2.

#### *5.4.2.3 Bubbles moving in lateral direction*

In this section, the experimental results with lateral bubbles motion are presented. Schematic diagram of the experimental setup was shown in Figure 5.7.b. The position of the capillary fiber was adjusted to be at the focal distance of the transducer.

Figure 5.12 presents the normalized harmonic amplitudes versus $PRI_{SHI}$ with a lateral bubble displacement through the second experimental method (constant PRF of

5.95 kHz). Note that, with lateral bubbles motion, the velocity could not be measured by Doppler display, the PRI was not translated to the ratio of bubbles motion to transmitted wavelength λ.

Figure 5.12 shows that the second-harmonic amplitudes of SHI are always much lower than 0 dB when the bubbles motion is in lateral direction. The curve does not exhibit an oscillation compared to the curve with axial bubbles motion.

These results infer the effectiveness of SHI depends on the axial bubbles motion between the two 90° phase-shifted transmissions. The influence of lateral bubbles motion is much less than the influence of axial bubbles motion.

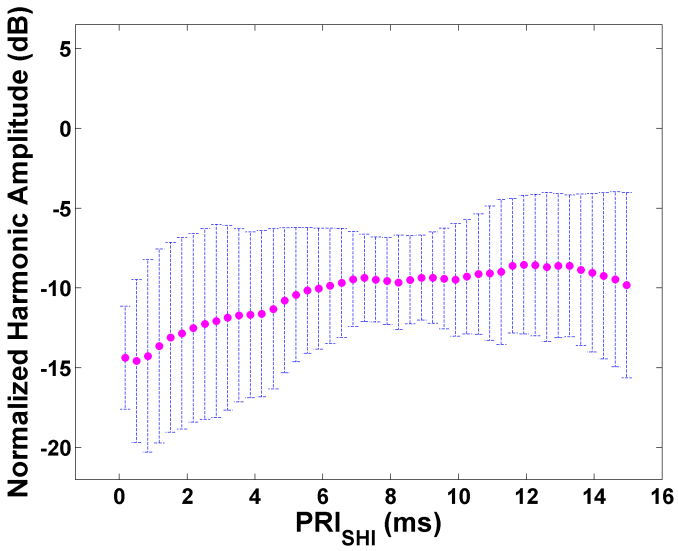


Figure 5.12 *In-vitro* experimental results from UCA moving in the lateral direction with the second experimental method (PRF = 5.95 kHz): average (dots) and standard deviation (bars) of the second-harmonic amplitude of SHI (normalized to the classic second-harmonic amplitude and expressed in dB) versus PRI between two 90° phase shifted pulses.

#### *5.4.2.4 Bubbles moving in angled direction*

In this section, the experimental results with angled bubbles motion are presented. Schematic diagram of the experimental setup was shown in Figure 5.7.c. The angle between the wave propagation direction and the bubbles movement direction was measured as 30°.

Figure 5.13 shows the Doppler display of these moving bubbles. From Figure 5.13, the maximum Doppler shift was read as 158 Hz, corresponding to 5.79 cm/s. This velocity value is the projection of the flow velocity in the wave propagation direction. Figure 5.14 presents the second-harmonic amplitude of SHI (normalized to the classic second-harmonic amplitude) versus $PRI_{SHI}$ from various SHI data sets. The $PRI_{SHI}$ was also translated to the ratio of bubble motion to transmitted wavelength. Note that

for the translation here, the mean flow velocity component projected in the wave direction (2.90 cm/s) was used.

In Figure 5.14, the maximum harmonic amplitude firstly appears when bubble motion is about 0.09 λ, which is the same as Figure 5.11. This means that it is feasible to use the velocity component projected in the wave direction during the translation from $PRI_{SHI}$ to motion-wavelength ratio.

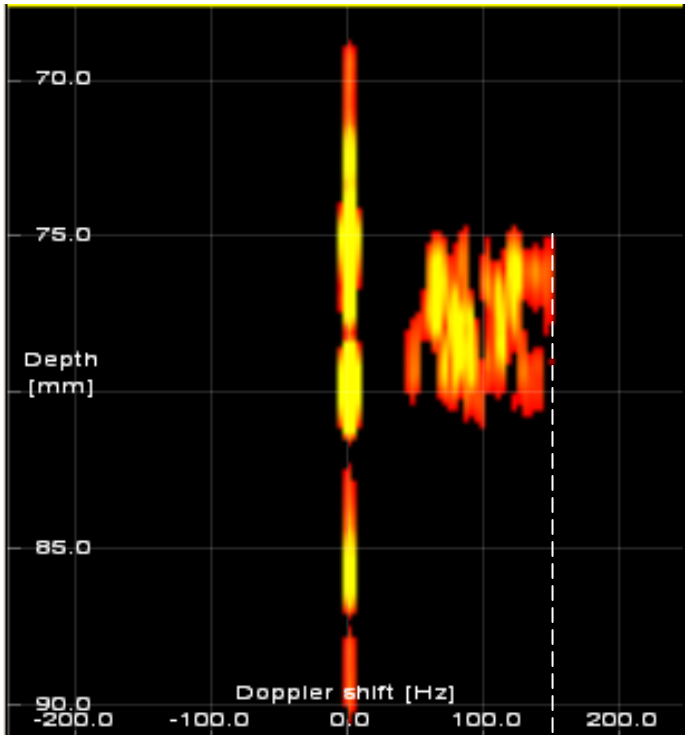


158

Figure 5.13 Doppler display of UCA bubbles moving in angled direction (displayed in the BBT controller interface).

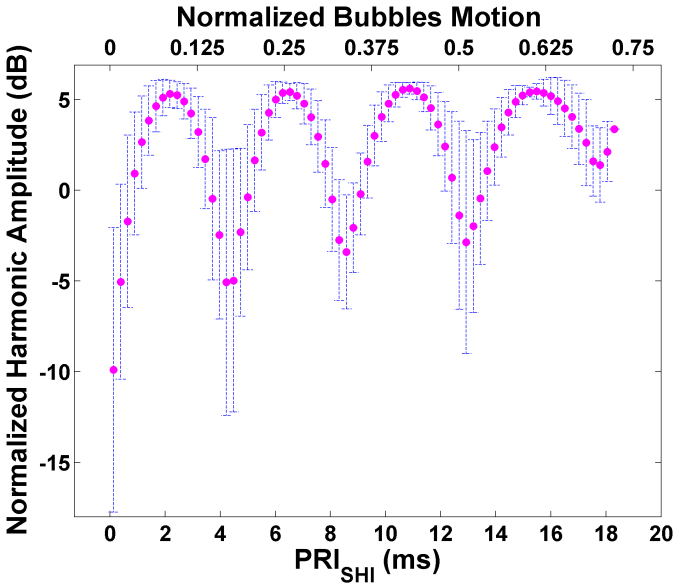


Figure 5.14 *In-vitro* experimental results from UCA moving in the angled direction of 30°: average (dots) and the standard deviation (bars) of the second-harmonic amplitude of SHI (normalized to the classic second-harmonic amplitude and expressed in dB) versus PRI between two 90° phase shifted pulses (lower axis) or versus the bubbles motion, normalized to the transmitted wavelength (upper axis), obtained from a population of circulating bubbles.

### 5.4.3 Fluid phantom mimicking a vessel

This section presents the experimental results obtained on a flow phantom model 453 (Dansk Fantom Service, Frederikssund, Denmark). The Sonovue UCA (Bracco, Geneva, Switzerland) diluted in water at a concentration of 0.09 µL/mL was circulating within the tubes embedded in the flow phantom. The tube has a diameter of 8 mm and a tilt angle of 35°. The average velocity of the flow in the tube can be controlled.

The UlaOp open platform, associated with a PA230 phased-array probe (Esaote, Italy), was used to transmit pulses. The probe has a 2.1-MHz central frequency. The transmitted pulses were seven-cycle and 1.7-MHz sine with the Hanning envelope. The peak transmitted pressure was measured as $134 \pm 9$ kPa, using a PVDF hydrophone (Precision Acoustics, Dorset, UK). These pulses with the 0° and 90° phase were transmitted for the SHI implementation. The imaging depth was 80 mm and the focal point was set at 65 mm. The received couple of successive signals corresponding to transmitted 90° phase-shifted pulses were summed and filtered at the second-harmonic band to form SHI images. The $PRF_{SHI}$ was regulated to obtain SHI images with various bubble motions.

Figure 5.15 shows the second-harmonic images (a, c) and SHI images (b, d) acquired with two different $PRF_{SHI}$ values when the nominal mean flow velocity of the flow phantom was 8.3 ± 0.7 cm/s. The $PRF_{SHI}$ was 6 kHz (a, b) and 0.432 kHz (c, d), respectively. The dynamic range of these images was 45 dB. For each image, the CTR was calculated as the ratio of the averaged amplitude in the UCA region and in the tissue region and was expressed in decibels. The CTR difference between the SHI image and the corresponding harmonic image was calculated:

$$\Delta CTR = CTR_{SHI} - CTR_{Harmonic} \tag{5.12}$$

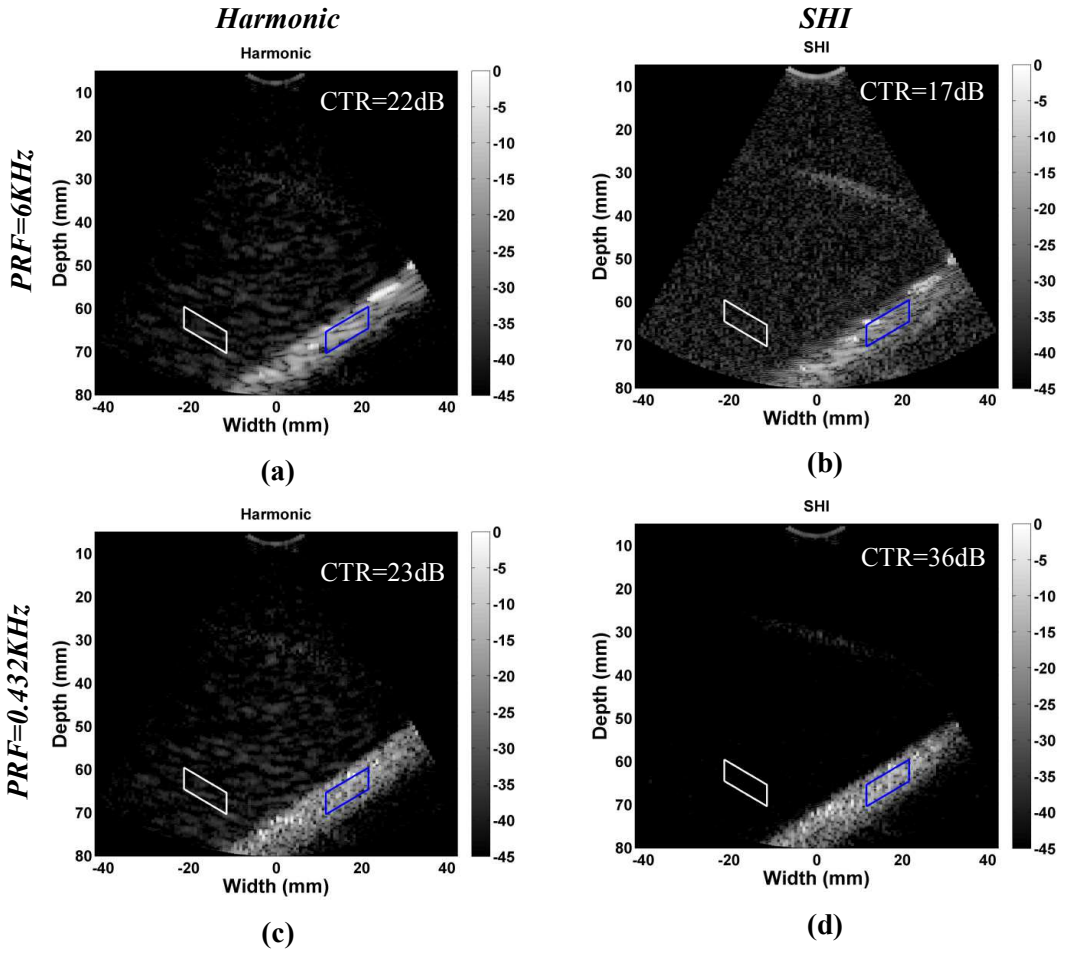


Figure 5.15 Acquired experimental second-harmonic images (a, c) and SHI images (b, d) of a fluid phantom with circulating UCA using a phased-array probe. The PRF was 6 kHz (a, b) or 0.432 kHz (c, d). The nominal average flow velocity was 8.3 ± 0.7 cm/s. For each image, the CTR was calculated between the averaged amplitude in UCA region and in tissue region.

Figure 5.15.d exhibits a much better contrast than Figure 5.15.b. When $PRF_{SHI}$ is 6 kHz, the CTR is decreased from 22 dB in second-harmonic image to 17 dB in SHI image. However, when the $PRF_{SHI}$ is 0.432 kHz, the CTR is increased from 23 dB in the second-harmonic image to 36 dB in the SHI image. That is, $\Delta CTR$ is increased

from −5 dB (difference between Figure 5.15.b and Figure 5.15.a) when $PRF_{SHI}$ is 6 kHz, to 13 dB (difference between Figure 5.15.d and Figure 5.15.c) when $PRF_{SHI}$ is 0.432 kHz. The improvement of $\Delta CTR$ reaches 18 dB. This observation shows that with moving bubbles, the effect of SHI imaging varies according to the $PRF_{SHI}$ of the transmitted pulses. Therefore, the SHI imaging effect can be guaranteed and further improved by controlling the $PRF_{SHI}$, when the flow velocity is known.

To clearly state the CTR improvement of SHI method with various $PRF_{SHI}$ values, the curves of CTR-difference between SHI image and corresponding harmonic image versus various $PRI_{SHI}$ values is presented in Figure 5.16.a for four different nominal mean flow velocities: 2.8 cm/s, 5.5 cm/s, 8.3 cm/s and 12.7 cm/s (standard deviation 0.7 cm/s). Note that these velocities values were given by the manufacturer of the fluid phantom. The $PRI_{SHI}$ is also translated to the ratio of bubbles motion relative to the transmitted wavelength in Figure 5.16.b. This translation considers the projection of the flow velocity component in the wave propagation direction, instead of the nominal flow velocity of the fluid phantom. For each $PRI_{SHI}$, 10 SHI images are acquired; the average value and the deviation of $\Delta CTR$ are calculated. The four resulting curves exhibit similar shapes, demonstrating the effectiveness of increasing CTR of SHI image by controlling the $PRI_{SHI}$. For the four different velocities, although the best $\Delta CTR$ occurs at different $PRI_{SHI}$, it always occurs when the bubble motion is translated to be around 0.075 λ. The best averaged $\Delta CTR$ is about 12 dB. In theory, the maximum $\Delta CTR$ value occurs when bubble motion is 0.125 λ. This mismatch comes from the deviation between the predefined mean water flow velocity and the actual bubble mean velocity. Several other error sources can also be identified: the actual profile of the flow and the radiation force due to the successive transmissions, slightly modifying the bubble velocities [Vos *et al.* (2007)].

In Figure 5.16, the presented results are limited to bubble motion from 0 to 0.16 λ, instead of several periods shown in the simulations and in the experiments presented in section 5.4.2.2. On one hand, to favor short acquisition time, it is less meaningful to investigate greater bubble motion. For example, with the 2.8-cm/s flow velocity, the greatest bubble motion corresponded to a $PRF_{SHI}$ as low as 73 Hz. On the other hand, this curve exhibits the greatest $\Delta CTR$ for a bubble motion lower than 0.16 λ.

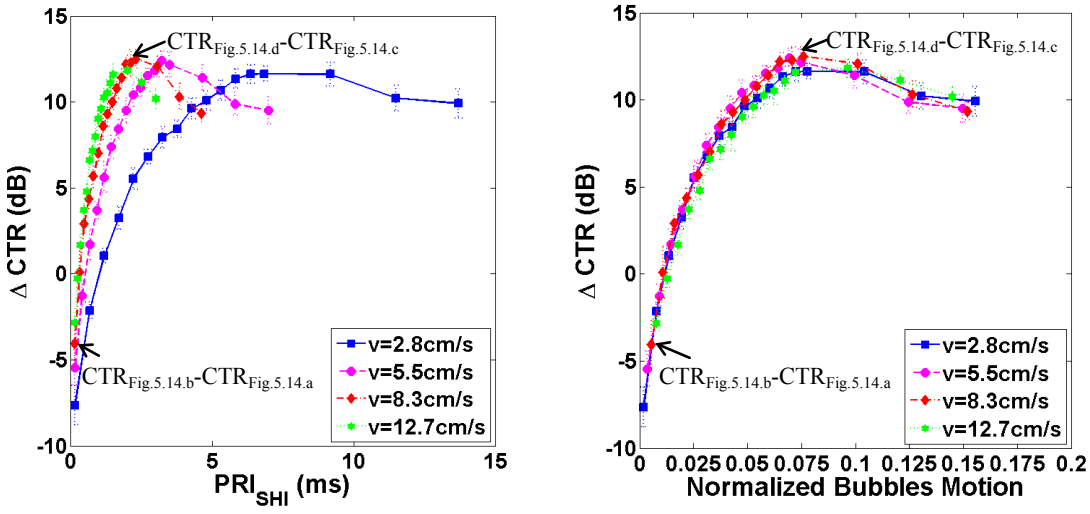


Figure 5.16 Experimental CTR-difference between SHI images and corresponding harmonic images ($\Delta CTR = CTR_{SHI} - CTR_{Harmonic}$) versus PRI between two SHI pulses (a) or the bubbles motion, normalized to the transmitted wavelength (b), obtained on a fluid phantom with circulating UCA. For each PRF, 10 SHI images were acquired to calculate the average value and the deviation of $\Delta CTR$. Results for four fluid velocities are presented.

## 5.5 *In-vivo* study

This section presents the *in-vivo* experimental results obtained on white rats. The rats weighted about 200 g. For each group of acquisitions, the Sonovue UCA (Bracco, Geneva, Switzerland) of 0.25 mL was injected from the tail and into the blood circulation system of the rat.

The open platform UlaOp, associated with the linear-array probe LA523 (Esaote, Italy), was used to transmit pulses. The probe has a 7 MHz central frequency. The transmitted pulses were 7-cycle and 5 MHz sine with Hanning envelope. These pulses with the phase of 0° and 90° were transmitted for the SHI implementation. The received couple of successive signals corresponding to transmitted 90° phase shifted pulses were summed and filtered at second harmonic band to form SHI images. PRF was regulated to obtain SHI images with various bubbles motions.

Figure 5.17 presents the acquired second-harmonic images (a, c) and SHI images (b, d) with two different PRF values, obtained from rat A. The PRF was 6 kHz (a, b) and 0.592 kHz (c, d) respectively. The dynamic range of these images was 40 dB. For each image, the CTR was calculated as the ratio of the averaged amplitude in blood vessel region and in tissue region, and was expressed in dB. In Figure 5.17.b, both signals in the blood vessel region and the tissue region were reduced. In Figure 5.17.d, the signals from the blood vessel region were strengthened while the signals from the tissue region were reduced, which leads to a higher CTR than second-harmonic image.

Figure 5.18 is the corresponding $\Delta CTR$ versus $PRI_{SHI}$ curve, obtained from acquired images with 17 different PRF values. The calculation method of $\Delta CTR$ is the same as in section 5.4.3. Figure 5.18 clearly shows that $\Delta CTR$ increases with ascending $PRI_{SHI}$.

Figure 5.19 show the images corresponding to PRF of 10 kHz (a, b) and 0.324 kHz (c, d), obtained on the same rat A but from another blood vessel. Figure 5.20 presents the $\Delta CTR$ curve from all the 17 different PRF values. Figure 5.21 and Figure 5.22 show the results obtained on another rat B.

All these *in-vivo* results demonstrate that the PRF has an important influence on the effectiveness of multi-pulse techniques. The difference in the SHI images, coming from different PRF, can be clearly observed. Suitable PRF should be found to guarantee the effectiveness of the multi-pulse techniques.

In Figure 5.18, Figure 5.20 and Figure 5.22, the latter half of the curves do not show a decrease as expected in theory or as shown by curves in previous parts. This comes from the fact that a certain quantity of the bubbles has already disappeared because of dissolution or destruction when the latter acquisitions were performed.

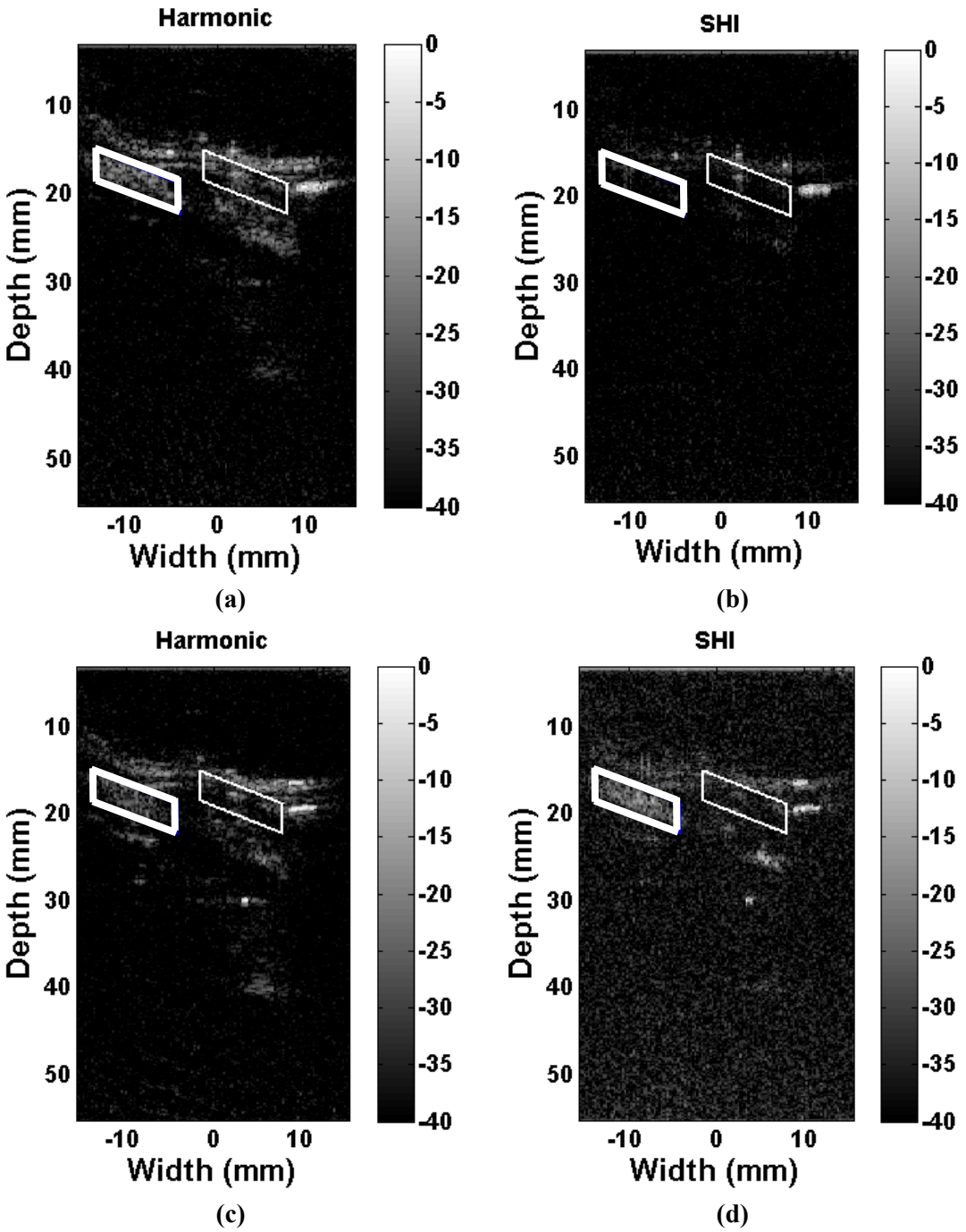


Figure 5.17 Acquired *in-vivo* second-harmonic images (a, c) and SHI images (b, d) of rat A, with circulating UCA in the blood vessel, using a linear-array probe. The PRF was 6 kHz (a, b) or 0.592 kHz (c, d). For each image, the CTR was calculated between the averaged amplitude in blood vessel region (thicker line box) and in tissue region (thinner line box).

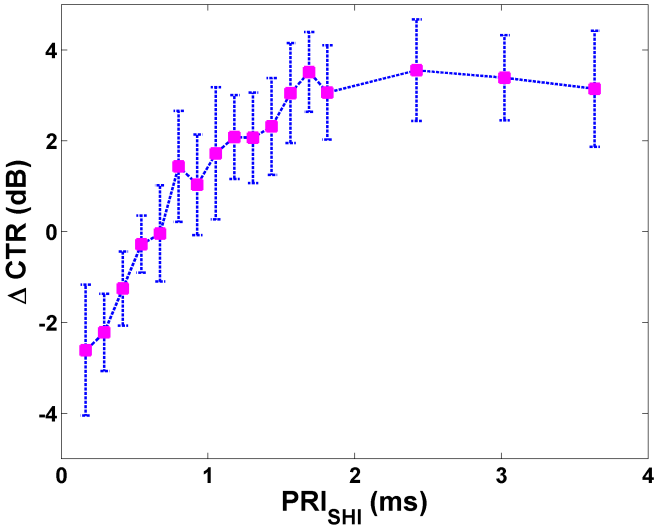


Figure 5.18 *In-vivo* experimental CTR-difference between SHI images and corresponding harmonic images ($\Delta CTR = CTR_{SHI} - CTR_{Harmonic}$) versus PRI between two SHI pulses, obtained on rat A with circulating UCA in the blood vessel. For each PRF, 10 SHI images were acquired to calculate the average value and the deviation of $\Delta CTR$.

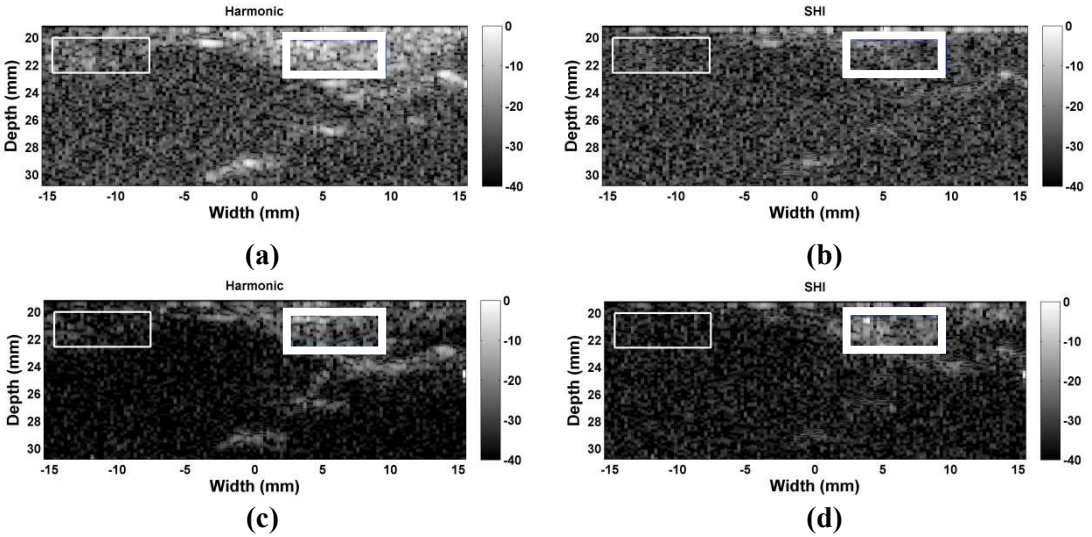


Figure 5.19 Acquired *in-vivo* second-harmonic images (a, c) and SHI images (b, d) of rat A, with circulating UCA in the blood vessel, using a linear-array probe. The PRF was 10 kHz (a, b) or 0.324 kHz (c, d). For each image, the CTR was calculated between the averaged amplitude in blood vessel region (thicker line box) and in tissue region (thinner line box).

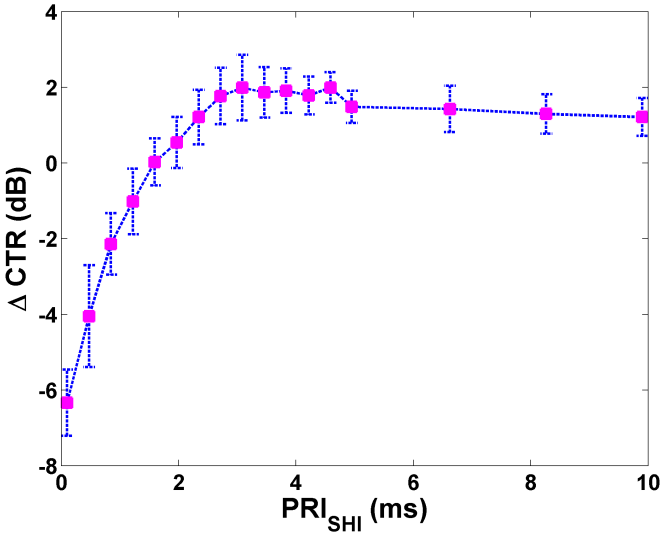


Figure 5.20 *In-vivo* experimental CTR-difference between SHI images and corresponding harmonic images ($\Delta CTR = CTR_{SHI} - CTR_{Harmonic}$) versus PRI between two SHI pulses, obtained on rat A with circulating UCA in the blood vessel. For each PRF, 10 SHI images were acquired to calculate the average value and the deviation of $\Delta CTR$.

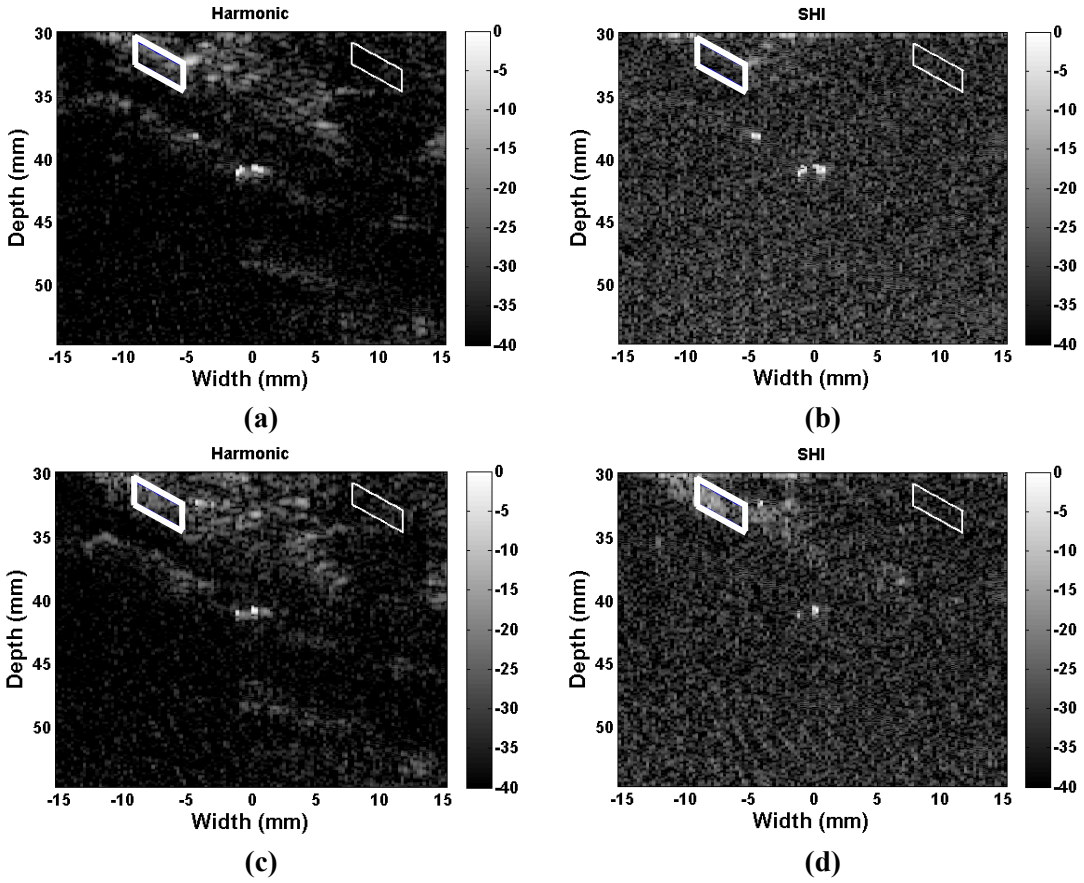

Figure 5.21 Acquired *in-vivo* second-harmonic images (a, c) and SHI images (b, d) of rat B, with circulating UCA in the blood vessel, using a linear-array probe. The PRF was 10 kHz (a, b) or 0.777 kHz (c, d). For each image, the CTR was calculated between the averaged amplitude in blood vessel region (thicker line box) and in tissue region (thinner line box).

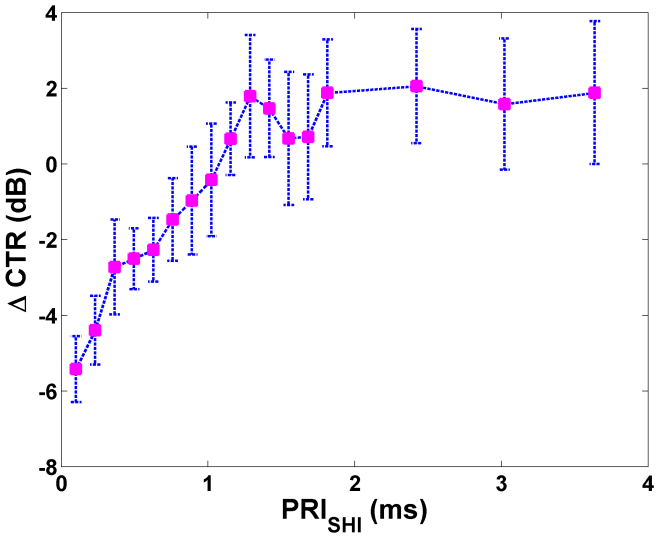


Figure 5.22 *In-vivo* experimental CTR-difference between SHI images and corresponding harmonic images ($\Delta CTR = CTR_{SHI} - CTR_{Harmonic}$) versus PRI between two SHI pulses, obtained on rat B with circulating UCA in the blood vessel. For each PRF, 10 SHI images were acquired to calculate the average value and the deviation of $\Delta CTR$.

## 5.6 Optimization of second harmonic inversion imaging

Previous work has already demonstrated that the phase shift of the echoes backscattered from bubbles is dependent on the transmissions' phase shift, and that the bubble motion influences the efficiency of multi-pulse techniques: fundamental and second-harmonic amplitudes of the summed signal change periodically, exhibiting maximum or minimum values, according to scatterer motion.

In previous sections, all the acquisitions corresponding to a dozen PRF values were used to recover the $\Delta CTR$ versus $PRI_{SHI}$ curve. After getting this curve, the optimal PRF value can be easily found. However, in clinical use, the optimal PRF value is expected to be found quickly in order to reduce the necessary acquisition time.

### 5.6.1 Method

This section investigates the feasibility of a recursive method to optimize the SHI technique.

Figure 5.23 shows the schematic diagram of the optimization procedure:

(1) the PRF is set as the initial value (as high as possible),

(2) after the first acquisition using this PRF value, CTR is calculated within the predefined ROI,
(3) the PRF value is updated by half of the previous PRF value,
(4) do the acquisition using current PRF and calculate the new CTR,
(5) if the CTR is increased, then repeat (3) and (4),
(6) if not, PRF is updated as the median of the previous value segment.
(7) The highest CTR is regarded as the optimal CTR, then the corresponding PRF is regarded as the optimal PRF.

### 5.6.2 Experimental setup

As in section 5.4.3, *in-vitro* experiments were conducted on a fluid phantom model 453 (Dansk Fantom Service, Denmark) with circulating Sonovue UCA (Bracco, Geneva, Switzerland).

The UlaOp open platform, associated with the PA230 phased-array probe (Esaote, Italy), was used to transmit pulses. The transmit settings were also the same as in section 5.4.3. Thanks to the availability of recursive command of the UlaOp platform, the optimization procedure described in section 5.6.1 can be carried out: the PRF value can be updated automatically by this ultrasound system, according to the calculated CTR. The way to calculate CTR is also the same as in section 5.4.3. At last, the UlaOp system gave out the optimal PRF.

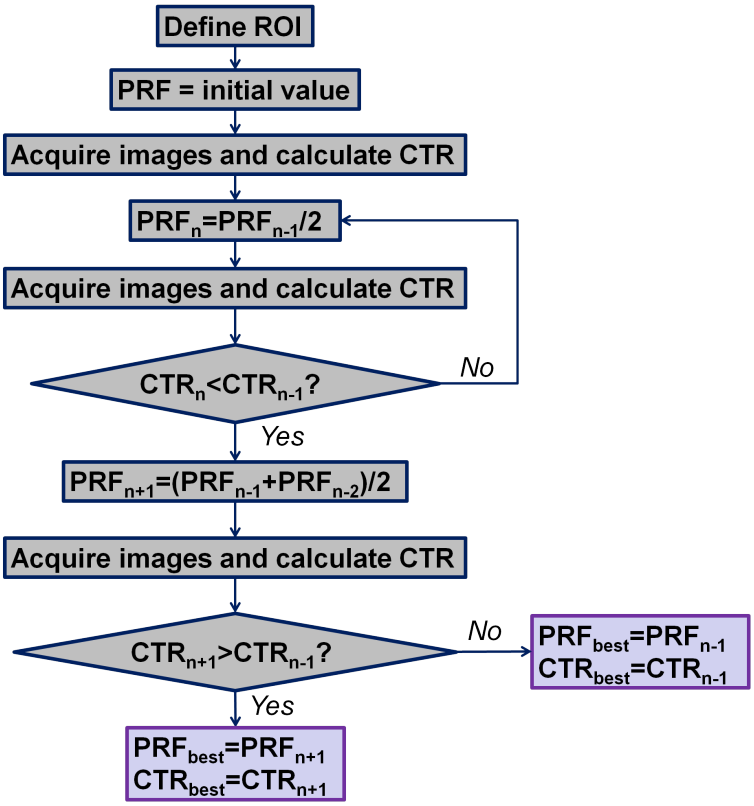


Figure 5.23 Schematic diagram of the optimization procedure.

### 5.6.3 Results

Figure 5.24.a shows the SHI image with the initial PRF value. The CTR is 15 dB. After 5 adjustments of PRF, the SHI image with the optimal PRF value was found and is presented in Figure 5.24.b. The CTR is 31 dB. In other words, the CTR was improved from 15 dB without the optimal PRF to 31 dB with the optimal PRF. So the improvement reaches 16 dB.

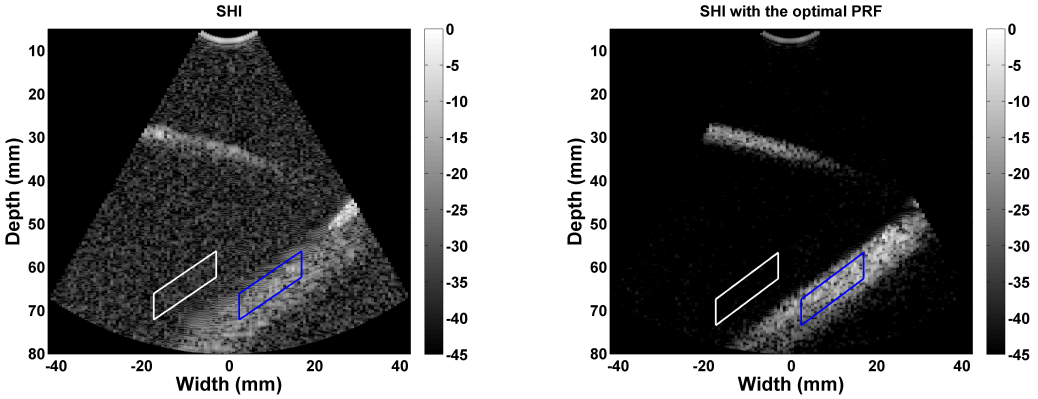


(a) (b)

Figure 5.24 SHI images of a fluid phantom with circulating contrast agents. (a) SHI image with two 90° phase-shifted transmissions. (b) SHI image with the optimal PRF after 5 adjustments of PRF. With the optimal PRF, the CTR was improved by 16 dB.

Compared to a dozen PRF value used in previous sections, the optimal PRF is found with only 5 adjustments. Therefore, the PRF can be adjusted to optimize automatically the SHI method in ultrasound contrast imaging.

## 5.7 Discussion

The effectiveness of the SHI technique depends on the preservation of the second harmonic of SHI in the UCA region and the reduction of the SHI second harmonic in the tissue region. Both *in-vitro* and *in-vivo* experimental results reveal that the effectiveness of SHI can be degraded when imaging is performed on relatively slow blood flow because the sum of the UCA second harmonic coming from the two 90° phase-shifted transmissions is also largely reduced. Based on our hypothesis, the ratio of the second-harmonic amplitude of the SHI pulse to the second-harmonic amplitude of a single pulse reaches the maximum value when the bubble motion is around $\lambda/8$, where $\lambda$ is the wavelength of the transmitted waves. Therefore, the effective preservation, or even improvement, can be achieved by properly matching the bubble motion and the wavelength of the transmitted wave.

Similarly, with PI, when the bubble motion between the two 180° phase-shifted transmissions is around $\lambda/4$, the additional phase shift of the two received pulses is $\pi$ for the fundamental frequency and $2\pi$ for the second harmonic. Therefore, the final amplitudes scattered from bubbles are maximum, that is, the CTR is maximum. However, in this situation, the resolution is lower than the PI resolution without bubble motion, because the fundamental amplitudes in the UCA region are largely increased, rather than only second-harmonic signals for PI without bubble motion.

In order to increase the UCA-scattered signals to optimize the PI or SHI technique, two alternatives can be proposed: adapt the phase of the second transmission or regulate the PRF. However, adapting the phase of the second transmission alters the surrounding tissue responses at the same time. Therefore, in order to keep the tissue signals reduced, and also for easier implementation, regulating the PRF is the preferable way to perform the optimization.

To optimize these techniques by regulating the PRF, the axial component of scatterer motion is used. Therefore, knowledge of the flow velocity and the angle between the flow direction and the wave propagation direction is required. The average value of flow velocities in the direction of wave propagation within the ROI can be used, considering that the flow velocities are not uniform and that the wave propagation directions vary within the ROI in phased-array scanning. The lateral component of scatterer motion is neglected because the phase shift of the

backscattered signals is much less sensitive to the lateral scatterer motion [Shen *et al.* (2002)], which has also been demonstrated by our *in-vitro* experiments with lateral bubbles motion (refer to section 5.4.2.3).

However, the use of axial component of scatterer motion to optimize multi-pulse techniques is also restricted by the following condition: the optimal $PRI$ should be found before all the bubbles leave the ultrasound beam, otherwise the backscattered signals directly become uncorrelated and the periodical curves such as those observed in Figure 5.10 or Figure 5.11 cannot be found. This condition can be expressed by the equation:

$$v \cdot PRI \cdot \sin(\phi) < B \tag{5.13}$$

where $v$ is the flow velocity, $PRI$ is the pulse repetition interval, $\phi$ is the angle between the flow and wave propagation direction, B is the lateral beamwidth. Taking SHI for example and based on equation (5.11), the optimal $PRI_{SHI}$ occurs when

$$\frac{4\pi v cos(\phi)}{\lambda \cdot PRF_{SHI}} = \frac{\pi}{2} \tag{5.14}$$

That is,

$$PRI_{SHI} = \frac{\lambda}{8v cos(\phi)} \tag{5.15}$$

Substitute (5.15) into (5.13), the following condition is deduced:

$$\frac{\lambda \tan(\phi)}{8} < B \tag{5.16}$$

Therefore, in case of SHI, the optimization by regulating $PRF$ is feasible when $\lambda \tan(\phi)/8 < B$.

Usually, radiologists, using ultrasound systems in clinical applications, have prior knowledge of the average velocity range of the blood flow in a ROI. For the implementation of SHI in ultrasound systems, a function can be added to command the preferred $PRI_{SHI}$ range according to $\lambda$ and the velocity range given by the operators. Consequently, the final optimal $PRI_{SHI}$ can be decided by the operator based on visual preference, by regulating the PRF within the preferred $PRI_{SHI}$ range. If the flow velocity and the direction angle are unknown, the PRF can be adjusted either manually or by the implementation of a recursive function to automatically determine the optimal $PRI_{SHI}$, using the CTR as the image quality criterion. Doppler is also an option to measure the flow velocity and help adjusting $PRI_{SHI}$. The technique can also be implemented in addition to standard fundamental imaging or harmonic imaging that is used to ensure the presence of contrast, while SHI imaging is used to improve the CTR in a ROI.

The proposed method of adjusting PRF has been presented when steady flows are concerned. However, in many applications, a pulsatile flow can be observed. In this case, although it is not possible to adjust the PRF for all the time varying velocities, a

severe degradation of the technique can be avoided through an adjustment of the PRF according to the average velocity of the pulsatile flow.

*In-vivo* experimental results agree with the *in-vitro* experimental results, in the degree that the effectiveness of multi-pulse techniques is strongly influenced by different PRF values. However, with the optimal PRF, the improvement of resulting image compared to the second-harmonic image ($\Delta CTR$), is much lower than the improvement obtained from *in-vitro* experiments. This is because of the tissue motion coming from respiration. All the *in-vitro* experiments presented in this study consider static surrounding tissues. Tissue motion is always a limitation for multi-pulse techniques because the harmonics generated due to moving tissues cannot be totally canceled, and the increased amplitude in background leads to a reduced CTR [Crocco *et al.* (2009)].

In the theoretical and simulation parts, the UCA is simply assumed to be a nonlinear medium for phase-shifted transmissions, not taking into account effects such as resonance and cavitation. However, *in-vitro* and *in-vivo* experimental results using BR14 and Sonovue bubbles demonstrate that the responses of the UCA to phase-shifted transmissions and the influence of bubble motion agree with the assumptions.

## 5.8 Conclusion

In ultrasound imaging, the contrast between UCA and tissues, that is the competition result between the echoes scattered by bubbles and tissues, is a very important criterion to judge contrast detection efficacy. To increase the discrimination between the two media, several multi-pulse techniques have been previously proposed, for example using phase modulation, amplitude modulation or combined phase and amplitude modulation. Some techniques aim to increase the harmonics produced by UCA while eliminating the linear responses within the transducer bandwidth, where tissues are regarded as linear scatterers [Brock-Fisher *et al.* (1996); Simpson *et al.* (1999); Eckersley *et al.* (2005)]. Some techniques take into account the nonlinear wave propagation in tissues and reduce the tissue-generated harmonics within the harmonic bandwidth [Pasovic *et al.* (2011)].

However, for any multi-pulse technique, the bubble motion between the transmitted pulses has an inevitable influence and can alter the results of the techniques, especially for those using phase modulation. Therefore, all the multi-pulse techniques in contrast imaging should take into account this motion influence. Most of the previous studies reported in the literature regarded bubble motion as a limitation for their multi-pulse techniques. In fact, for some techniques such as SHI, bubble motion can become a positive factor for the technique's effectiveness.

This chapter assumes that: i) for multi-pulse techniques, the phase shift of the echoes backscattered from bubbles is dependent on the transmissions' phase shift; ii)

bubble motion adds an additional phase shift and therefore influences the efficiency of multi-pulse techniques. Simulation results on a static medium insonated by transmissions with different phase shifts and on a medium with scatterer motion insonated by transmissions with constant phase shift validate the above hypothesis.

The experimental results are mainly based on the SHI technique, which transmits two 90° phase-shifted waves and the summed received echoes are filtered at the second-harmonic band to form SHI images. The $PRF_{SHI}$ is regulated to take into account various bubble motions. The experimental results on a single bubble, obtained with a single-element probe, confirm that when bubbles move in the wave propagation direction, the second-harmonic amplitude of SHI changes periodically with the increasing bubble motions between two 90° phase-shifted pulses, and the maximum value firstly appears when the bubble motion is 0.125 λ. Experimental results on a population of bubbles with a single-element probe and on a flow phantom with a phased array probe further demonstrate that the SHI image quality can be guaranteed and improved with suitable bubble motion by regulating the $PRF_{SHI}$, if the flow is not perpendicular to the wave propagation direction. The best CTR improvement reaches around 12 dB when compared to a single-pulse second-harmonic image. *In-vivo* experimental results agree with the simulation and *in-vitro* experimental results, although the CTR improvement reaches only 2-3 dB because of the presence of tissue motion.

All these experimental results validate that the phase shift of the echoes backscattered from bubbles is dependent on the transmissions' phase shift, and show how the bubble motion influences the efficiency of a multi-pulse technique.

The work presented in this chapter encourages the development of multi-pulse imaging techniques with automatic control of the phase shift between consecutive pulses or of the PRI to optimize the implemented technique and the image quality.

# Chapter 6

## Double pulse inversion

## Contents

This chapter proposes a new strategy, called double pulse inversion (DPI), by applying the PI technique twice, to reduce the tissue-generated harmonics and to improve CTR. Simulations, *in-vitro* and *in-vivo* experimental results are shown.

This work has been partly presented in the conference *IEEE IUS* [Lin *et al*., 2012c].

## 6.1 Introduction

As it has been mentioned in previous chapters, in ultrasound contrast imaging, a large discrimination between ultrasound contrast agents (UCA) and surrounding tissues is expected. However, the contrast-to-tissue ratio (CTR) is limited because of the tissue-generated harmonics during the wave propagation [Aanonsen *et al.* (1984)]. To reduce these harmonics in view to further increase the CTR, a lot of techniques have been proposed. [S Krishnan *et al.* (1998); Christopher (1999); Simpson *et al.* (1999); Eckersley *et al.* (2005); Shen *et al.* (2007a); Pasovic *et al.* (2010), (2011)]

Among these techniques, pulse inversion (PI) has been largely used in clinical ultrasound machines [Simpson *et al.* (1999)]. A sequence of two inverted pulses is transmitted and the two received signals are summed. For a linear system, the response of the second pulse is an inverted copy of the response from the first pulse and the sum of the two pulses is zero. For a nonlinear system, the sum is not zero. PI works over the entire bandwidth of the received echo signal and achieves a better image resolution.

In this chapter, a new strategy, called double pulse inversion (DPI) by applying the PI technique twice, is proposed. Inverted pulses are transmitted. First, before the arrival of UCA, the resulting PI signals, representing the remaining tissue-harmonic signals are saved. Second, after the arrival of UCA, the resulting PI signals, representing both tissues and UCA harmonics are saved. Then the resulting PI signals obtained before and after the presence of UCA are subtracted to suppress the tissue-harmonic signals. However, the presence of tissue movements will affect the effectiveness of this technique.

The chapter is organized as follows: section 6.2 introduces the theoretical background; section 6.3 presents the simulations, *in-vitro* and *in-vivo* experimental results of DPI; and section 6.4 discusses and concludes this chapter.

## 6.2 Method

The complete model of nonlinear wave propagation in tissues can be described by the KZK equation (Eq.(3.18)) [Zabolotskaya *et al.* (1969); VP Kuznetsov (1970)]. For a non-viscous homogeneous medium, a lossless Burgers' equation can be used (Eq.(3.14)) [Burgers (1948)]. Fubini provided a solution for this lossless Burgers' equation (Eq.(3.15)) [Fubini (1935)]. This Fubini solution is rewritten here:

$$p(z,\tau) = p_0 \sum_{n=1}^{\infty} \frac{2}{nz_d} J_n(nz_d)\sin(n\omega_0\tau) \tag{6.1}$$

Assuming the two successively transmitted pulses are:

$$p_1(z=0,\tau) = P_0 \cos(\omega_0\tau + \varphi_1) \tag{6.2}$$

$$p_2(z=0,\tau) = P_0 \cos(\omega_0\tau + \varphi_2) \tag{6.3}$$

where $P_0$ is the amplitude of the pulse, $\omega_0$ is the angular frequency, $\varphi_1$ and $\varphi_2$ are the phases.

Let:

$$\Delta\varphi = \varphi_2 - \varphi_1 \tag{6.4}$$

Using trigonometric properties, the summation of the two waves can be expressed as:

$$p_{sum}(z,\tau) = 4p_0 \sum_{n=1}^{\infty} \frac{J_n(nz_d)}{nz_d} \cos(n(\omega_0\tau + \varphi_1 + \frac{\Delta\varphi}{2}))\cos(\frac{n\Delta\varphi}{2}) \tag{6.5}$$

Therefore, when

$$n = \frac{k\pi}{\Delta\varphi}, where\ k = 1,3,5\ldots \tag{6.6}$$

$n^{th}$ harmonic is zero. When

$$n = \frac{2k\pi}{\Delta\varphi}, where\ k = 1,2,3\ldots \tag{6.7}$$

$n^{th}$ harmonic doubles. Therefore, for PI ($\Delta\varphi = \pi$), every odd harmonic is zero and every even harmonic doubles.

Figure 6.1 is the schematic diagram of double pulse inversion (DPI) method.

## 6.3 Results

### 6.3.1 Simulation

This part presents the results of simulations using DPI. In simulations, a tool based on a finite difference method proposed by Voormolen was used to simulate the wave pressure fields [Voormolen (2007)]. The harmonic images were computed with a delay and sum algorithm implemented in CREANUIS software [Varray *et al.* (2013)]. The dimensions used for simulation of pressure field were listed in Table 4.1.

The blood vessel was simulated as a tube with a diameter of 8 mm and a tilt angle of 35°. To simulate the presence and absence of UCA in the blood vessel, the non-linear coefficient $\beta$ and the reflectivity of reflectors in the blood vessel were set at different values. The non-linear coefficient $\beta$ of surrounding tissues was set at 4.5,

which is a conventional value for biological tissues [Zhang *et al.* (2001)], the non-linear coefficient of the blood vessel was set at 51 with the presence of UCA, and at 3.5 without the presence of UCA [Wu *et al.* (1998)]. Furthermore, the amplitude of each reflector (defining the amount of reflected signal) in the blood vessel was 10 times the amplitude set in the tissue region when UCA were concerned, and 0.8 times when no UCA were concerned in the blood vessel.

First, the blood vessel was simulated without UCA. Pulses at a frequency of 3 MHz, the initial pressure of 200 kPa and the phase shift of 180° were transmitted. The received radio frequency (RF) signals were summed. Then the same procedure was conducted when the blood vessel was simulated as having UCA. At last, the two kinds of RF signals before and after the presence of UCA were subtracted to get DPI RF signals.

Figure 6.2 presents the simulated images of PI and DPI. The images were normalized and log-compressed. The dynamic range was 45 dB. The average signals within the blue lines in the UCA region and the white lines in the tissue region were calculated respectively. Then the CTR was calculated from the averaged signals in the UCA region and in the tissue region.

Figure 6.2 shows that the DPI image exhibits a much better contrast than the PI image. The CTR is improved by about 28 dB.

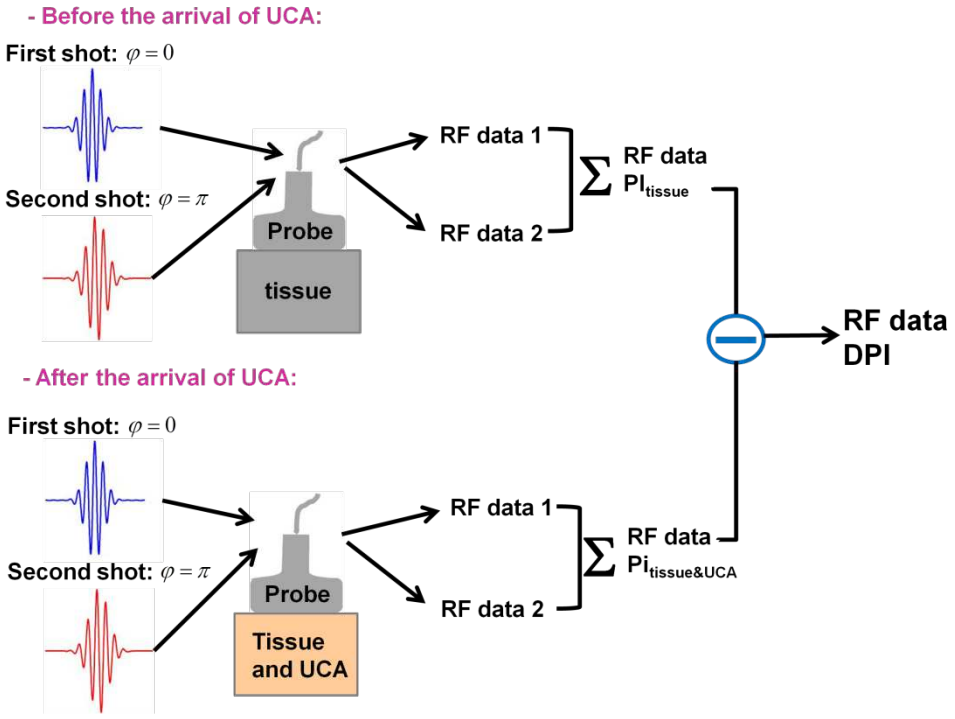


Figure 6.1 Schematic diagram of double pulse inversion (DPI) method

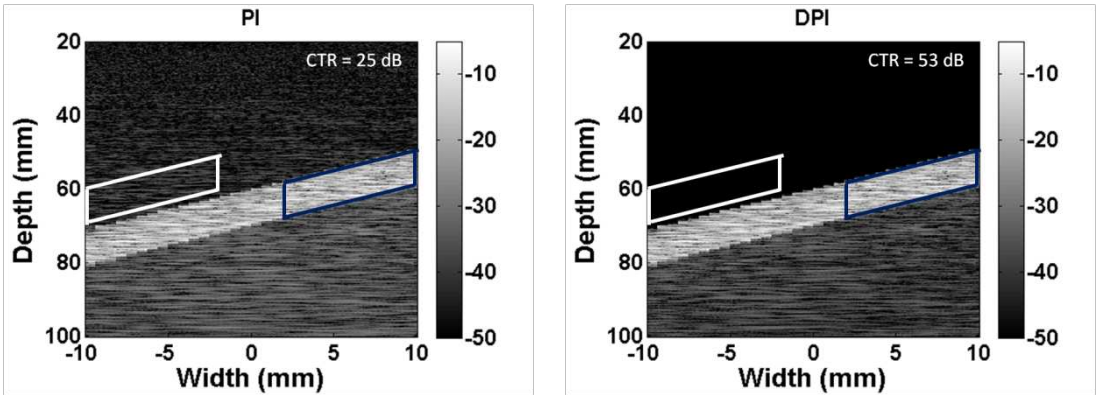


(a) (b)

Figure 6.2 Simulated images of PI (a) and DPI (b). The CTR was calculated from the averaged signals in the UCA region (within the blue lines) and in the tissue region (within the white lines) The CTR is improved by about 28 dB.

### 6.3.2 *In-vitro* study

This part presents the *in-vitro* experimental results using DPI. A fluid phantom model 453 (Dansk Fantom Service, Denmark) was used. The Sonovue UCA (Bracco, Geneva, Switzerland) diluted to a concentration of about 0.09 μL/mL was circulating within the tubes embedded in the fluid phantom. The tube has a diameter of 8 mm and a tilt angle of 35°.

The open platform UlaOp (MSD Lab, Italy), associated with the phased-array probe PA230 (Esaote, Italy), was used to transmit pulses. The probe has a 2.1 MHz central frequency. The transmitted pulses were 7-cycle and 1.7 MHz sine with a Hanning envelope. The imaging depth was 80 mm and the focal point was set at 30 mm.

Before the presence of UCA, the pulses with the phase shift of 180° were transmitted. The received RF signals were summed and saved, that is, the remaining tissue-harmonic signals were saved. Then after the arrival of UCA, PI was applied once again and the summed signals are saved, that is, both tissues and UCA harmonics were saved. At last, the resulting PI signals obtained before and after the presence of UCA were subtracted.

Figure 6.3 presents the PI image and DPI image. The CTR was calculated from the averaged signals in the UCA region and tissue region as described in the simulation part.

Figure 6.3 also shows that the DPI image has a better contrast than the PI image. The CTR is increased from 23 dB in PI image to 28 dB in DPI image, meaning a CTR improvement of about 5 dB.

To clearly state the reduction of tissue-harmonic signals, the spectrum of one RF line from DPI and PI are shown together in Figure 6.4 . Figure 6.4.a is the spectrum in the surrounding tissue region, a reduction in the second-harmonic band could be

observed after using DPI. Figure 6.4.b is the spectrum in the UCA region, where the spectrum amplitude stays unchanged. Therefore, the CTR is increased.

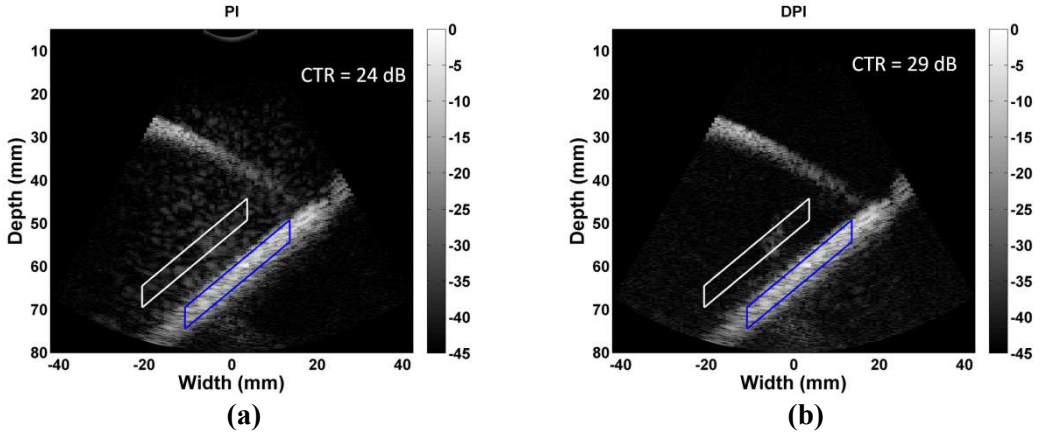


Figure 6.3 *In-vitro* experimental results: PI image (a) and DPI image (b) of a fluid phantom with circulating UCA. The CTR was calculated from the averaged signals in the UCA region (within the blue lines) and in the tissue region (within the white lines). The CTR is improved by about 5 dB.

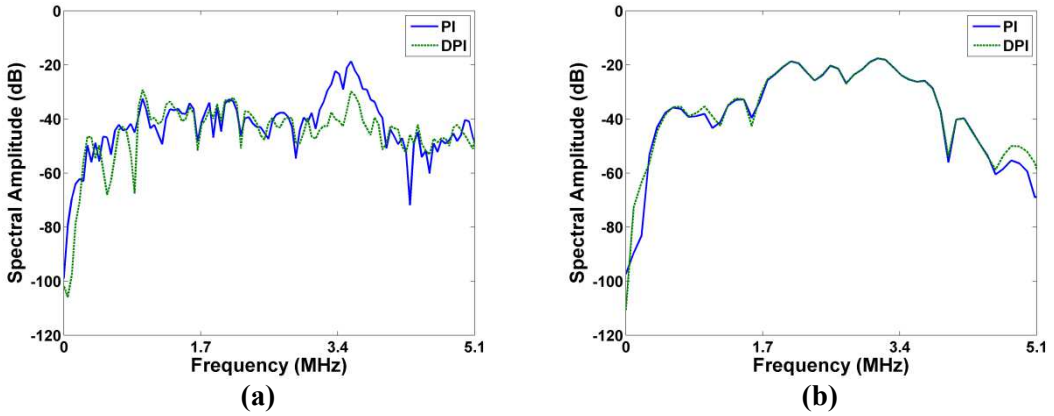


Figure 6.4 The spectrum of the central RF line from a fluid phantom with circulating UCA; the spectrum amplitude was normalized to the fundamental amplitude of a single pulse response; the signals from PI (solid line) and DPI (dashed line) in the tissue region (a) and UCA region (b) are presented. The fundamental frequency was 1.7 MHz.

### 6.3.3 *In-vivo* study

This part presents the *in-vivo* experimental results obtained on white rats. The rats weighted about 200 g. The open platform UlaOp, associated with the linear-array probe LA523 (Esaote, Italy), was used to transmit pulses. The probe has a 7 MHz central frequency. The transmitted pulses were 7-cycle and 5 MHz sine with Hanning envelope. Pulses with the phase of 0° and 180° were transmitted for the PI implementation. The received couple of successive signals corresponding to transmitted 180° phase shifted pulses were summed to form PI images. Before and

after the injection, the PI image was acquired respectively. For each injection, 0.25 mL Sonovue UCA (Bracco, Geneva, Switzerland) was used.

As in the simulation part and the *in-vitro* experimental part, PI and DPI images are presented in the Figure 6.5. The spectrum of one RF line, in the UCA part and in the tissue part respectively, is presented in Figure 6.6.

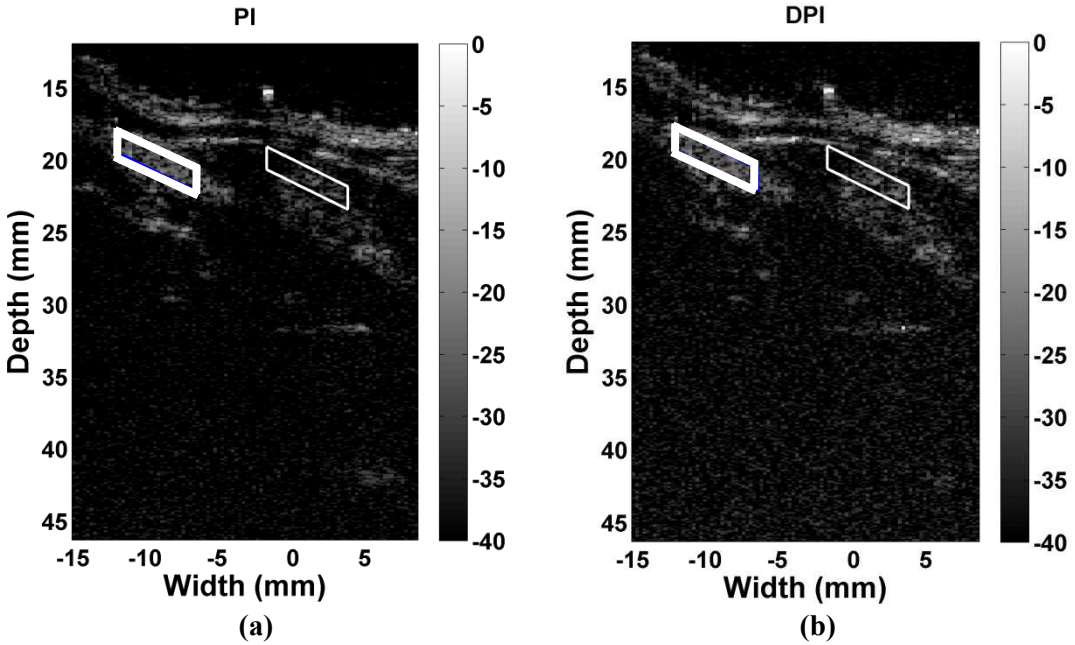


Figure 6.5 *In-vivo* experimental results: PI image (a) and DPI image (b) of a rat with UCA in the blood vessel. The CTR was calculated from the averaged signals in the UCA region (within the thicker lines) and in the tissue region (within the thinner lines).

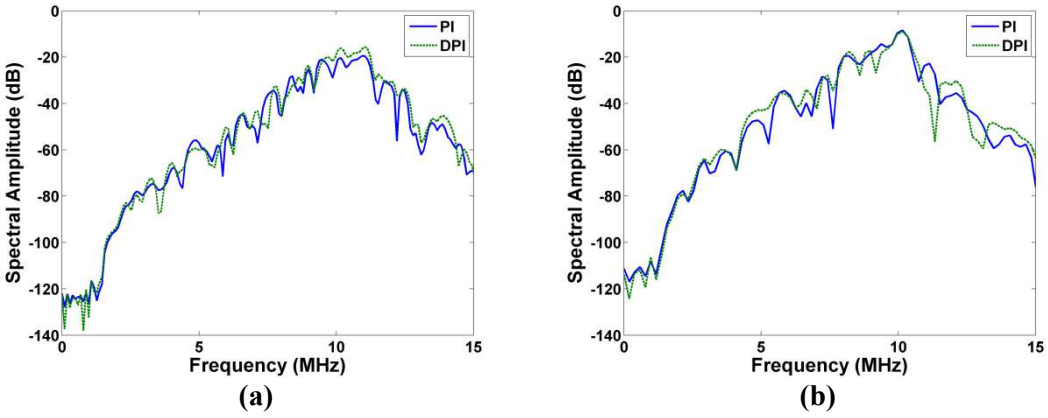


Figure 6.6 The spectrum of the central RF line from a rat; the spectrum amplitude was normalized to the fundamental amplitude of a single pulse response; the signals from PI (solid line) and DPI (dashed line) in the tissue region (a) and UCA region (b) are presented. The fundamental frequency was 5 MHz.

Figure 6.5 shows that the CTR value in the DPI image is not improved as in the simulations and *in-vitro* experiments. From the signal analysis in Figure 6.6, the reduction of tissue-harmonics is not found in the tissue region (Figure 6.6.a). This probably comes from the presence of tissue motion, which makes the technique inefficient. The implementation of this technique requires that the acquisitions are performed on static media.

## 6.4 Discussion and conclusion

Both simulation and *in-vitro* experimental results demonstrate the effectiveness of reducing surrounding tissue harmonic signals of this new strategy. Using DPI, the CTR is increased by 5 dB for *in-vitro* experiments when compared with conventional PI technique. The level of CTR improvement depends on the amplitude of generated second harmonic in tissues which is mainly decided by the transmitted energy, the non-linearity of the tissues and the depth of ROI.

This DPI technique is easy to implement. Considering that it spends some time for the UCA to arrive at the ROI after being injected into the human body, the signals of the imaged tissue before the arrival of UCA could be collected, for the implementation of DPI.

However, motions of the probe or of tissues before and after the arrival of UCA should be avoided because the effectiveness of this technique depends on the similarity between the tissue-harmonic signals with and without the presence of UCA. *In-vivo* experimental results confirm that the tissue motion of the rat during the acquisition is a strong limit of this technique. Therefore, this technique must be mainly applied to static tissues.

# IV. CONCLUSION AND PERSPECTIVE

# Chapter 7

## Conclusion and perspective

### Contents

## 7.1 Conclusions

This thesis firstly generalizes most of the multi-pulse techniques in ultrasound contrast imaging. A formulation is presented to predict the nonlinear components in each frequency band and to design new transmission sequences to either increase or decrease specified nonlinear components in each harmonic band. Simulations on several multi-pulse techniques have been done and have been compared with experimental results given in previous literatures. The agreement between simulation and experimental results validates the generalization of such a mathematical background for multi-pulse transmissions.

Then, the influence of bubble motion to multi-pulse techniques has been investigated. Simulations, *in-vitro* experiments from a single bubble and clouds of bubbles, and *in-vivo* experiments from white rats have been done. All these results show that the phase shift of the echoes backscattered from bubbles is dependent on the transmissions' phase shift, and that the bubble motion influences the efficiency of multi-pulse techniques: fundamental and second-harmonic amplitudes of the summed signal change periodically, exhibiting maximum or minimum values, according to scatterer motion. Furthermore, experimental results based on the second-harmonic inversion (SHI) technique reveal that bubble motion can be taken into account to regulate the pulse repetition frequency (PRF). With the optimal PRF, the CTR of SHI images can be improved compared to second-harmonic images.

Besides of these, a new technique, called double pulse inversion (DPI), has also been proposed. The PI technique is applied twice before and after the arrival of the contrast agents to the region of interest. The resulting PI signals are reduced to suppress the tissue-generated harmonics and to improve CTR. Simulations and *in-vitro* experimental results have shown an improved CTR of DPI. However, *in-vivo* experimental results confirm that the tissue motion of the rat during the acquisition is an inevitable barrier of this technique.

## 7.2 Perspectives

**Generalization:** New excitations, based on the generalized formulation, can be designed to strengthen the responses of contrast agents or to weaken the responses of tissue, to improve the CTR in contrast imaging.

**Influence of bubble motion:** Understanding how bubbles respond to phase-shifted transmissions and how bubble movements influence the effectiveness of multi-pulse techniques is important to better evaluate the existing techniques or to design new contrast detection techniques. Results in this part show that the PRF tuning according to the bubble displacement can be meaningful in some cases to improve the efficacy of some multi-pulse techniques. An automatic PRF tuning could be envisaged on a

specific imaging device, allowing rapid changes of the PRF, defined by feedback, in accordance to an image quality criterion calculated in real time, such as the CTR for example. The PRF tuning can be complementary to usual techniques, such as standard fundamental imaging or harmonic imaging to improve the CTR in a ROI. Moreover, it can be used, by the addition of some nonlinear method by mixing different images computed with different PRF, to enhance the benefits and improve the CTR not only in a ROI but throughout the image.

# VERSION BREVE EN FRANCAIS

## Contents

# I. Introduction

## 1. Ultrasons médicaux

Chaque jour, nous touchons avec le son, un phénomène physique très commun et intuitif. Alors qu'est-ce que le son? Le son est une onde mécanique: une vague créée par des objets oscillants qui se propage à travers un milieu (gaz, liquide ou solide). Un paramètre important pour décrire le son, ou onde acoustique, est la fréquence $f$. Selon la fréquence, le son peut être classé en infrasons, sons audibles et ultrasons. La fréquence du signal sonore qui est perceptible par l'oreille humaine, est d'environ 20 Hz à 20 kHz. L'onde acoustique ayant une fréquence supérieure à 20 kHz est appelé ultrasons tandis que l'onde d'une fréquence inférieure à 20 Hz est appelé infrasons. Comme une onde mécanique, la propagation du son dépend des propriétés du milieu. Ainsi, les grandeurs physiques liées au milieu, comme la densité $\rho$ et la vitesse du son $c$, sont également importantes. Les effets tels que la réflexion, la réfraction, la diffusion, l'atténuation, l'absorption sont généralement impliqués dans la propagation du son.

L'one ultrasonore, en raison de propriétés telles que une bonne directivité, une haute résolution spatiale ou une haute énergie, a été appliquée dans divers domaines : la détection sous-marine, la détection des défauts industriels, la mesure de distance, le nettoyage de pièces mécaniques, et production d'alliage. En plus de ces domaines, les ultrasons sont également largement utilisés dans le diagnostic médical et la thérapie médicale. En imagerie diagnostic, les ultrasons présentent de nombreux avantages par rapport aux autres modalités d'imagerie : très grande sécurité pour le patient et les praticiens (pas d'ondes ionisantes), une imagerie temps réel et à faible coût.

Pour l'échographie médicale, le milieu de propagation est constitué par les tissus des organes du corps humain. Etant donné que les tissus ont une teneur élevée en eau, la propagation des ondes dans le corps est souvent modélisée comme dans les liquides [Szabo, 2004]. Dans les tissus biologiques, la vitesse moyenne du son est d'environ 1540 m/s. La fréquence des ultrasons en diagnostic est habituellement dans la gamme comprise entre 1,5 MHz et 15 MHz. Ainsi, la longueur d'onde de l'onde ultrasonore est comprise entre 1 mm et 0,1 mm. Comme la longueur d'onde est plus grande que la particule du milieu, ou de l'obstacle, la diffusion est l'effet dominant lorsque l'onde ultrasonore se propage à travers le milieu biologique. Les signaux rétrodiffusés à partir de toutes les particules au cours de la trajectoire de l'onde sont capturés par le transducteur et affichés sous forme d'une image ultrasonore, qui peut montrer la structure de l'anatomie de la région insonifiée.

## 2. Objectif de la thèse

De façon classique, les signaux rétrodiffusés sont collectés pour former une image ultrasonore. Aujourd'hui, l'imagerie non-linéaire qui utilise les signaux non-linéaires rétrodiffusés, est devenue une branche importante dans le domaine de l'imagerie par ultrasons, principalement parce qu'elle fournit une meilleure résolution. L'imagerie non-linéaire, aussi appelé imagerie harmonique, peut être divisée en imagerie harmonique tissulaire et imagerie harmonique de contraste, selon la nature des diffuseurs non-linéaires.

L'imagerie harmonique de contraste a été développée parce que les agents de contraste, qui sont injectés par voie intraveineuse pour améliorer les faibles échos rétrodiffusés à partir de cellules sanguines, peuvent vibrer non linéairement lorsqu'ils sont soumis à une pression acoustique supérieure à un seuil. Les signaux rétrodiffusés par des agents de contraste sont collectés pour former des images harmoniques qui permettent de distinguer les échos linéaires rétrodiffusés par le tissu environnant. L'imagerie harmonique de contraste est couramment utilisée pour aider au diagnostic des maladies cardio-vasculaires en observant la structure anatomique des vaisseaux et du cancer des organes abdominaux en observant la dynamique de la perfusion tissulaire.

Cependant, les signaux non linéaires déjà mentionnés ci-dessus peuvent également provenir des tissus. Au cours de la propagation des ondes dans les tissus, l'interaction entre l'onde acoustique et les tissus modifie la forme de l'onde transmise, de sorte que les harmoniques de l'onde transmise sont générés. La présence de signaux harmoniques de tissus se confond avec les signaux harmoniques des agents de contraste et dégrade la qualité d'image lorsque l'imagerie harmonique de contraste est mise en œuvre.

Par conséquent, l'objectif de cette thèse est de mieux distinguer les échos provenant des agents de contraste et les échos provenant des tissus, que ce soit à travers la proposition de nouvelles modalités, ou l'optimisation de modalités existantes.

## II. Contexte

### 3. Agents de contraste ultrasonores

Les agents de contraste ultrasonores (UCA) sont constitués de plusieurs millions de microbulles, injectés par voie intraveineuse dans le corps humain pour augmenter la diffusion des ultrasons par le sang. Les microbulles de gaz injectées dans le sang ont la capacité d'augmenter très fortement la réflectivité du milieu soumis à une onde ultrasonore [Gramiak *et al.* (1968)].

Les agents de contraste doivent être assez persistants pour effectuer un diagnostic, de petites tailles pour circuler dans les capillaires et passer à travers la circulation pulmonaire, et être assez inerte pour ne pas altérer l'hémodynamique. De nos jours, les

agents de contraste sont généralement remplis de gaz et encapsulés. Les propriétés acoustiques des agents de contraste sont fortement influencées par le type de matériau de la capsule.

Le diamètre d'une microbulle est de l'ordre du micron. Comme elle est beaucoup plus petite que la longueur d'onde ultrasonore (entre 0,1 et 1 mm), en présence d'une onde ultrasonore, la bulle se comporte comme un diffuseur de Rayleigh. La bulle dans l'eau a une section équivalente 100 millions de fois supérieure à celle d'une sphère de fer ayant le même rayon, en raison de la compressibilité différente de la bulle de gaz [De Jong (1993)].

Lorsque l'amplitude de pression est grande, une bulle se dilate plus facilement qu'elle se comprime. Récemment, il a également été constaté que certaines bulles peuvent se comprimer uniquement [De Jong *et al.* (2007)]. Ces vibrations asymétriques conduisent à des réponses non linéaires des bulles.

A la différence des bulles d'air, un agent de contraste a généralement une coque qui enferme le gaz. La majorité de ces gaz sont des perfluorocarbones ou de l'air, et les coques sont à base d'albumine sérique, de lipide, de polymère, de surfactant etc. Le diamètre des agents de contraste est d'environ 1 à 10 $\mu m$ et l'épaisseur de la coque est de l'ordre de 10 à 200 $nm$.

Le comportement des agents de contraste sous excitation acoustique dépend de la pression et de la fréquence d'excitation, et de la structure des microbulles. La présence de la coque, limite l'expansion de l'agent de contraste et la fréquence de résonance est plus élevée.

Pour bien comprendre le comportement des agents de contraste, des efforts ont été faits pour modéliser la vibration des microbulles d'agent de contraste [Leighton (1994)], [De Jong *et al.* (1992)], Hoff modèle [Hoff *et al.* (2000)] [Marmottant *et al.* (2005)].

L'application d'agents de contraste ultrasonores se divise en deux secteurs: le diagnostic et la thérapie. Une application diagnostique majeure est l'opacification d'une région par l'augmentation de la diffusion du milieu. Cela se traduit sur l'image ultrasonore par l'apparition d'une région claire correspondant à la présence de vascularisation. Une autre application diagnostique est la quantification de la perfusion, qui est la quantité de sang livré dans un volume local de tissu par unité de temps [Szabo (2004)]. Pour l'application thérapeutique, les agents de contraste sont conçus pour transporter des médicaments à des sites ciblés et libérer le médicament par la fragmentation des bulles induite par ultrasons. Cette approche permet d'éviter le gaspillage de grandes quantités de médicaments dans l'organisme, de limiter les effets secondaires indésirables, et de s'assurer que les médicaments sont délivrés sur des sites ciblés [Lindner (2001)].

## 4. Propagation non linéaire des ultrasons

Lorsque la propagation des ondes est étudiée, l'hypothèse que les ondes obéissent au principe de linéarité est faite. La linéarité signifie que les ondes gardent la même forme au cours de la propagation quelle que soit leur amplitude et que les différentes réalisations des ondes au même endroit peuvent être sommées pour former des ondes plus élaborées.

Lorsque la pression $p$ de la perturbation de l'onde traverse le milieu, les particules sont déplacées de leur équilibre initial à une vitesse $\vec{u}$. Si la viscosité du milieu est négligée, la propagation de l'onde ultrasonore obéit aux équations linéarisées d'Euler. Une autre hypothèse consiste à considérer que le processus est adiabatique, ce qui signifie qu'il n'y a pas de transfert de chaleur pendant les fluctuations rapides de l'onde acoustique. Sous cette hypothèse et pour des amplitudes infinitésimales, la linéarité est satisfaite et la pression est décrite par:

$$p - p_0 = \left[\rho_0 \left(\frac{\partial p}{\partial \rho}\right)_{S,\rho=\rho_0}\right]\left(\frac{\rho - \rho_0}{\rho_0}\right) = \rho_0 c_0^2 \left(\frac{\rho - \rho_0}{\rho_0}\right) \qquad \text{(VF-Eq.1)}$$

où $p_0$ et $\rho_0$ sont la pression et la densité à l'équilibre, $\rho_0 c_0^2$ est une constante lorsque $\rho = \rho_0$ et à une entropie spécifique $S$.

En réalité, le tissu est non linéaire, tout comme une grande partie du monde qui nous entoure. Cette non-linéarité modifie l'équation de la propagation des ondes. L'équation d'état VF-Eq.1 devient [Beyer (1960)]:

$$\begin{aligned} p - p_0 = &\left[\rho_0 \left(\frac{\partial p}{\partial \rho}\right)_{S,\rho=\rho_0}\right]\left(\frac{\rho - \rho_0}{\rho_0}\right) \\ &+ \frac{1}{2!}\left[{\rho_0}^2 \left(\frac{\partial^2 p}{\partial \rho^2}\right)_{S,\rho=\rho_0}\right]\left(\frac{\rho - \rho_0}{\rho_0}\right)^2 + \cdots \end{aligned} \qquad \text{(VF-Eq.2)}$$

Dans cette équation, un développement en série de Taylor est utilisé pour obtenir une expression de la pression en fonction de la densité.

De l'équation VF-Eq.2, la non-linéarité est exprimée par le paramètre non linéaire $B/A$, où

$$A = \rho_0 \left(\frac{\partial p}{\partial \rho}\right)_{S,\rho=\rho_0} = \rho_0 c_0^2 \qquad \text{(VF-Eq.3)}$$

$$B = {\rho_0}^2 \left(\frac{\partial^2 p}{\partial \rho^2}\right)_{S,\rho=\rho_0} \qquad \text{(VF-Eq.4)}$$

Plus fréquemment c'est le coefficient de non-linéarité, $\beta$, qui est utilisé:

$$\beta = 1 + \frac{B}{2A} \qquad \text{(VF-Eq.5)}$$

La dépendance quadratique de la pression par rapport à la densité conduit à un changement de la vitesse du son entre la demi-période positive et la demi-période négative de la pression.

VF-Figure. 1.a et VF-Figure. 1.b illustrent la forme initiale d'une onde de pression sinusoïdale et la distorsion après propagation. Ce phénomène peut aussi été observé dans le domaine des fréquences. Pour l'onde initiale, seulement la composante fondamentale est présente (VF-Figure. 1.c). Pour l'onde déformée, plusieurs composantes harmoniques apparaissent (VF-Figure. 1.d).

Le modèle complet de la propagation des ondes non linéaires dans un milieu peut être décrit par l'équation Khokhlov-Zabolotskaya-Kuznetsov (KZK) [Zabolotskaya *et al.* (1969); VP Kuznetsov (1970)]:

$$\frac{\partial p}{\partial z} = \frac{c_0}{2}\Delta_{\perp} p + \frac{\delta}{2c_0^3}\frac{\partial^2 p}{\partial \tau^2} + \frac{\beta p}{\rho_0 c_0^3}\frac{\partial p}{\partial \tau} \qquad \text{(VF-Eq.6)}$$

Les trois termes dans la partie droite de (VF-Eq.6) représentent l'effet de diffraction de la sonde, l'atténuation du milieu et la distorsion non linéaire du milieu, respectivement. $\Delta_{\perp} p$ dépend de la forme du transducteur.

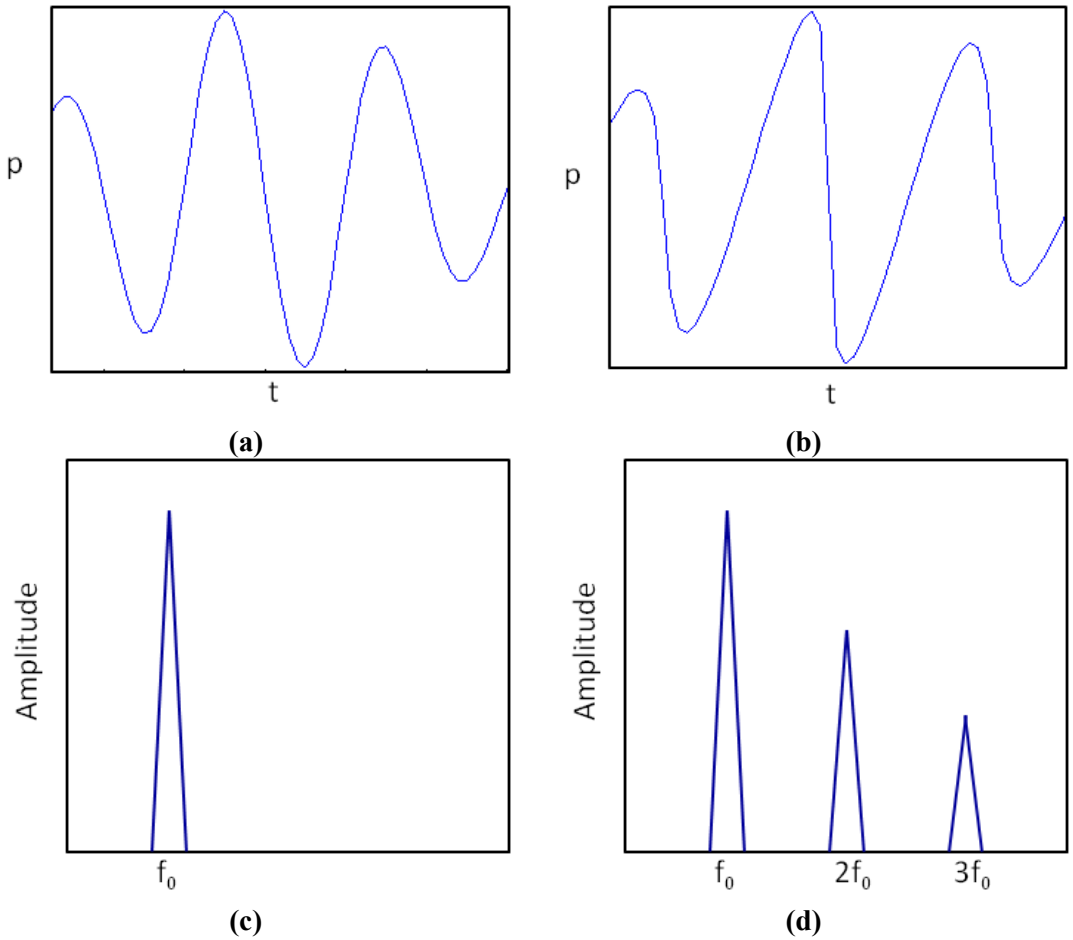


VF-Figure. 1 Illustration de la forme initiale d'une onde de pression sinusoïdale (a) et de la forme d'onde après propagation et déformation (b). Dans le domaine fréquentiel, une seule composante fondamentale est présente pour l'onde initiale (c), tandis que les composantes harmoniques apparaissent avec la déformation de l'onde (d).

## III. Contribution

### 5. Généralisation des techniques multi-impulsions

Afin d'augmenter le rapport de l'intensité de l'agent de contraste sur l'intensité du tissu (CTR pour "Contrast to Tissue Ratio") pour l'imagerie de contraste, de nombreuses techniques de transmission multi-impulsions ont été proposées. La plupart d'entre elles modulent un ou plusieurs paramètres parmi la fréquence d'émission et de réception, l'amplitude d'impulsion, la phase d'impulsion, la durée d'impulsion, le nombre d'impulsions et la fréquence de répétition des impulsions (PRF).

Dans la technique d'inversion d'impulsion (PI), une séquence de deux impulsions en opposition de phase est transmise [Simpson *et al.* (1999)]. Pour un système linéaire, la réponse à la deuxième impulsion est une copie inversée de la réponse à la première et la somme des deux réponses est égale à zéro. Pour un système non linéaire, la somme n'est pas nulle, les composantes du second harmonique des deux signaux s'ajoutent. L'inversion d'impulsion fonctionne sur toute la largeur de bande du signal d'écho reçu et permet d'obtenir une meilleure résolution de l'image.

Pasovic *et al.* ont proposé une méthode appelée "second harmonic inversion" (SHI) [Pasovic *et al.* (2011)]. Comme pour le PI, une séquence de deux impulsions est transmise et les deux réponses sont sommées, mais le décalage de phase entre les deux impulsions d'émission est de 90°. Etant donné que la composante de seconde harmonique a une relation quadratique à la fondamentale, le déphasage entre les deux composantes de deuxième harmonique est de 180°, de sorte que le second harmonique est annulé dans la région du tissu lors de la sommation.

Il existe également plusieurs méthodes pour augmenter la réponse non-linéaire des microbulles. Borsboom *et al.* ont proposé une méthode appelée "pulse subtraction time delay imaging". Cette méthode transmet trois impulsions. Les deux premières ne se recouvrent pas temporellement et la troisième est la somme des deux premières. Aux échos provenant de la troisième impulsion sont soustraites ceux des deux premières impulsions [Borsboom *et al.* (2009)]. Brock-Fisher *et al.* ont utilisé une modulation d'amplitude (AM) [Brock-Fisher *et al.* (1996)]. Les échos linéaires sont annulés, alors que les composantes d'ordres impaires sont conservées. La combinaison de la modulation de phase et d'amplitude dans un procédé de détection non-linéaire plus général a été suggérée par Haider et Chiao [Haider *et al.* (1999)]. Phillips a évalué cette idée sur trois agents de contraste différents avec plusieurs séquences appelées "contrast pulse sequence" (CPS) [PJ Phillips (2001); P Phillips *et al.* (2004)]. Eckersley *et al.* [Eckersley *et al.* (2005)] ont combiné PI et AM où la seconde impulsion a été inversée et son amplitude est la moitié de celle de la première impulsion. La réponse à la seconde impulsion est multipliée par deux avant d'être

additionnée à la réponse à la première impulsion. Le CTR a été renforcée de 4±1 dB. Wilkening *et al.* ont transmis cinq impulsions avec des phases équidistantes, une sommation pondérée des échos reçus supprime les harmoniques sélectionnés [Wilkening *et al.* (2000), (2001)] .

Nous proposons une base mathématique de généralisation de la plupart des techniques d'imagerie par ultrasons multi-impulsions. La formulation présentée peut être utilisée pour prédire les composantes non linéaires dans chaque bande de fréquence et concevoir de nouvelles séquences de transmission afin d'augmenter ou diminuer des composantes non linéaires spécifiées dans chaque bande.

Pour vérifier la généralisation de la formulation, des simulations de plusieurs techniques multi-impulsions ont été réalisées. Etant donné que des résultats expérimentaux ont déjà été présentés dans les littératures mentionnées ([Brock-Fisher *et al.* (1996); Haider *et al.* (1999); Simpson *et al.* (1999); Wilkening *et al.* (2000); Eckersley *et al.* (2005); Pasovic *et al.* (2011)]), seules les simulations ont été réalisées ici. La validation de cette formulation mathématique a été faite en comparant les résultats de simulation avec les résultats expérimentaux publiés dans la littérature. Les résultats de la simulation sont globalement en accord avec les résultats expérimentaux présentés dans la littérature. Les écarts observés ont fait l'objet de discussions.

Ces travaux ont été présentés dans un article de revue soumis à *Ultrasonics* [Lin et al., 2013b].

## 6. Influence du mouvement des diffuseurs dans les techniques multi-impulsions

Aujourd'hui, bien que beaucoup de travaux aient été faits sur des modèles d'une bulle vibrante [De Jong *et al.* (1992); Marmottant *et al.* (2005)] et sur les modèles de propagation des ultrasons à travers les agents de contraste [Tang *et al.* (2006)], peu d'études ont été présentées sur la modification du signal rétrodiffusé par les agents de contraste lorsque les signaux d'excitation présentent différentes phases. En fait, la littérature révèle certains conflits: certains auteurs estiment que la phase des échos de bulles n'est pas altérée par un changement dans la phase du signal transmis [Morgan *et al.* (1998); Pasovic *et al.* (2011)], tandis que d'autres considèrent que la phase des échos de bulles peut être modifiée par la phase des signaux transmis [Simpson *et al.* (1999); Eckersley *et al.* (2005)]. Ce point est d'une importance majeure pour les techniques multi-impulsions.

En outre, toutes les techniques d'impulsions multiples sont influencées par le mouvement des diffuseurs pendant l'intervalle de répétition des impulsions (PRI). Notons que le PRI est l'inverse de la fréquence de répétition des impulsions (PRI = 1/PRF). Parce que le mouvement des diffuseurs entre les tirs consécutifs a le même effet qu'un décalage de phase, ces mouvements peuvent améliorer ou dégrader les

techniques impliquées. Par conséquent, la quantification de l'influence du mouvement des agents de contraste excités par des impulsions multiples est intéressante.

Ce travail examine non seulement la réponse des milieux non-linéaires statiques excités par des impulsions multiples avec des déphasages différents, mais aussi l'influence du mouvement des diffuseurs dans les techniques des impulsions multiples. Des simulations, des expériences *in-vitro* sur une seule bulle et sur un nuage de bulles, et des expériences *in-vivo* sur des rats blancs ont été réalisées.

VF-Figure. 2 montre le schéma de principe du dispositif expérimental: la pression hydrostatique, en raison de la différence de hauteur, force un débit d'eau du réservoir dans la fibre capillaire, et assure la circulation. La fibre capillaire, en cellulose régénérée, a un diamètre extérieur de 200 μm. L'agent de contraste BR14 (Bracco, Genève, Suisse), dont le diamètre moyen est de 3 μm, est injecté avec une seringue.

Un transducteur piézoélectrique mono élément, avec une fréquence centrale de 3 MHz, 70% de bande passante et une distance focale d'environ 70 mm, est relié à un contrôleur 'Bubble Behaviour Testing' (BBT) (laboratoire MSD, Florence, Italie) [Ricci *et al.* (2006)]. Le contrôleur BBT permet de transmettre des signaux arbitraires, d'enregistrer les signaux rétrodiffusés, de régler le PRF, la région d'intérêt (ROI) et la taille de stockage de données. Les transmissions de 10 cycles sinusoïdaux avec une enveloppe de Tukey, une fréquence centrale de 2 MHz, et une pression négative de pointe de 170 kPa. Pour chaque onde émise, les signaux RF rétrodiffusés par l'agent de contraste sont numérisés sur 2048 échantillons avec une résolution de 14 bits à une fréquence d'échantillonnage de 64 MHz. Des impulsions sont transmises avec les phases de 0° et de 90° en alternance. Ces données RF sont utilisées pour étudier la relation entre le mouvement de la bulle et l'amplitude de l'harmonique en mode SHI.

Pour obtenir différentes valeurs de déplacement de la bulle entre deux transmissions déphasées de 90°, un seul ensemble de données acquises avec le PRF constant de 7,81 kHz est utilisé. Différents ensembles de données de SHI sont ensuite créés, en sous-échantillonnant les données d'origine, en combinant la ligne RF d'une transmission de 0° avec les lignes RF de transmissions de 90° différentes et non-successives.

Après l'obtention de l'ensemble de données de SHI, les amplitudes du second harmonique sont calculées dans le domaine fréquentiel par FFT. Les amplitudes du second harmonique des deux données RF déphasés de 90° sont calculées et moyennées, pour donner l'amplitude du second harmonique classique. L'amplitude du second harmonique de SHI est ensuite normalisée par rapport à l'amplitude du second harmonique classique.

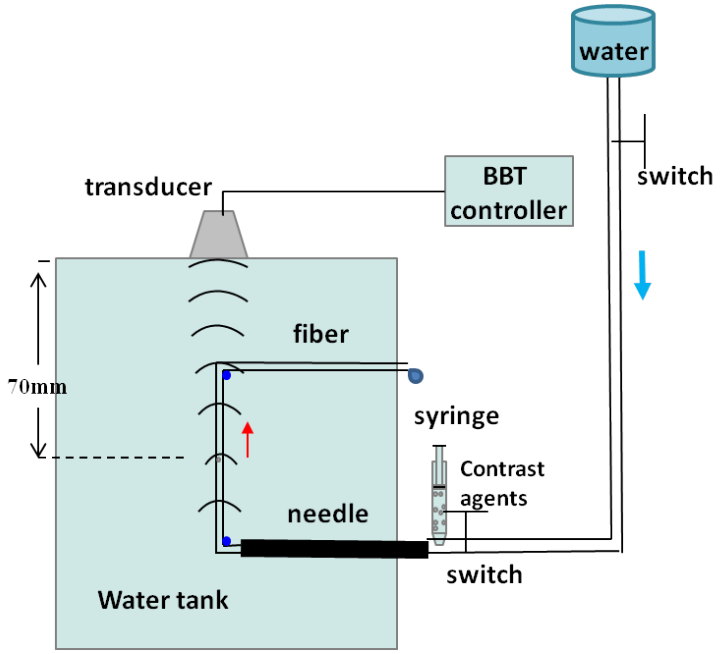


VF-Figure. 2 Schéma du montage expérimental utilisant un transducteur mono élément: la pression hydrostatique due à la différence de hauteur permet la circulation de l'agent de contraste à l'intérieur de la fibre (200 µ m de diamètre). Les bulles se déplacent dans la direction axiale. Le contrôleur BBT définit les signaux transmis.

Pour obtenir la réponse d'une seule bulle, l'agent de contraste est dilué à une concentration faible (de l'ordre de $4 \times 10^5$ puis $7 \times 10^5$ microbulles/ml). La très grande sensibilité du système BBT permet d'obtenir le faible écho d'un événement unique. Il est supposé que cet événement unique provient d'une seule bulle (VF-Figure. 3).

VF-Figure. 3.a présente la transformée de Hilbert des données (l'image M-mode) avec la transmission de phase 0° sur une seule bulle en mouvement. Les oscillations résiduelles de l'enveloppe proviennent du second harmonique présent dans l'écho de bulle. La vitesse de la bulle est mesurée à partir de la pente des lignes droites sur l'image en mode M. Elle est de 3,85 ± 0,02 cm/s. VF-Figure. 3.b présente l'amplitude du second harmonique en mode SHI (normalisée par rapport à l'amplitude du second harmonique d'une émission unique) versus $PRI_{SHI}$ de divers ensembles de données. $PRI_{SHI}$ est l'intervalle de temps entre deux transmissions décalées de la phase de 90° dans la technique SHI. Pour chaque ensemble de données SHI, la valeur moyenne et l'écart type de l'amplitude du second harmonique sont représentés. Le $PRI_{SHI}$ est également traduit en fonction du rapport du mouvement de la bulle à longueur d'onde transmise. VF-Figure. 3 montre clairement que l'amplitude de l'harmonique de SHI varie périodiquement avec le mouvement de la bulle, et la valeur maximale se produit lorsque le mouvement de la bulle est de 0,126 λ. Notez que la valeur théorique maximale est obtenue avec un déplacement de λ/8 (ou 0,125 λ).

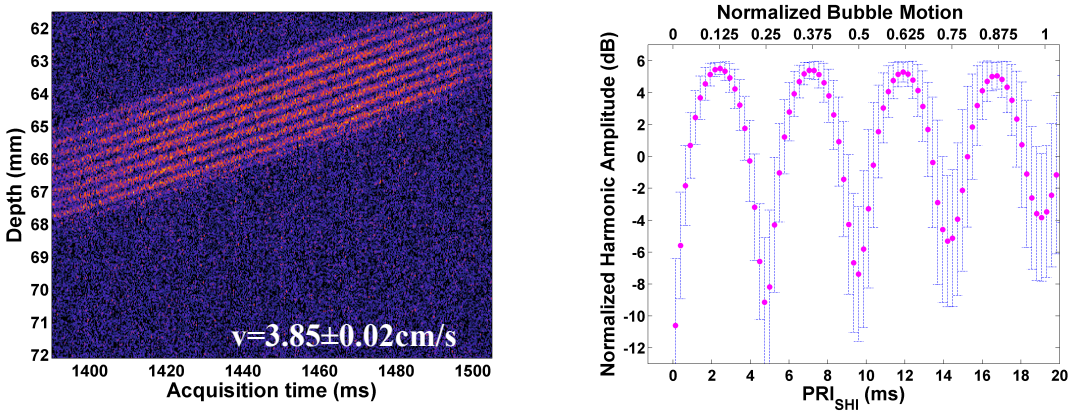


VF-Figure. 3 Résultats expérimentaux *in-vitro* de l'agent de contraste se déplaçant dans la direction axiale obtenu avec un PRF constant(PRF = 7.81 kHz): (a) l'image en mode M d'une seule bulle en mouvement; (b) moyenne (points) et écart type (barres) de l'amplitude de l'harmonique de SHI (normalisé à l'amplitude de l'harmonique classique et exprimée en dB) en fonction du PRI entre deux impulsions déphasées de 90° (axe inférieur) ou du mouvement de la bulle, normalisée à la longueur d'onde transmise (axe supérieur), obtenu à partir d'une seule bulle.

Des expériences sur des bulles circulant dans un fantôme de flux (Dansk Fantom Service, Frederikssund, Danemark) ont également été faites. L'agent de contraste Sonovue (Bracco, Genève, Suisse) dilué dans l'eau à une concentration de 0,09 µL/mL circule dans le tube noyé dans le fantôme de flux. Le tube a un diamètre de 8 mm et un angle d'inclinaison de 35°. La vitesse moyenne de l'écoulement dans le tube peut être réglée.

La plate-forme d'imagerie ouverte UlaOp, associée à une sonde PA230 (Esaote, Italie), est utilisée pour transmettre des impulsions. La sonde présente une fréquence centrale de 2,1 MHz. Les impulsions transmises sont formées de sept-cycles sinusoïdaux à 1,7 MHz et modulées en amplitude avec une enveloppe de Hanning. La pression maximale transmise est mesurée à 134 ± 9 kPa, à l'aide d'un hydrophone PVDF (Precision Acoustics, Dorset, Royaume-Uni). Des impulsions avec une phase de 0° et de 90° sont transmises successivement pour la mise en œuvre de SHI. La profondeur d'imagerie est de 80 mm et le point focal est fixé à 65 mm. Les deux signaux reçus correspondant à des impulsions transmises déphasés de 90° sont additionnés, puis filtrés dans la bande du second harmonique pour former des images de SHI. Le $PRI_{SHI}$ est réglé pour obtenir des images de SHI avec divers déplacements de bulles.

VF-Figure. 4 montre les images du second harmonique (a, c) et les images SHI (b, d) acquis avec deux $PRI_{SHI}$ de valeurs différentes lorsque la vitesse d'écoulement moyenne nominale dans le fantôme est de 8,3 ± 0,7 cm/s. Le $PRI_{SHI}$ est de 6 kHz (a, b) et de 0,432 kHz (c, d), respectivement. La dynamique de ces images est de 45 dB.

Pour chaque image, la CTR est calculé comme le rapport de l'amplitude moyenne dans la région de l'UCA et dans la région du tissu et est exprimée en décibels. La différence de CTR entre l'image SHI et l'image harmonique correspondant est calculée:

$$\Delta CTR = CTR_{SHI} - CTR_{Harmonic} \qquad \text{(VF-Eq.7)}$$

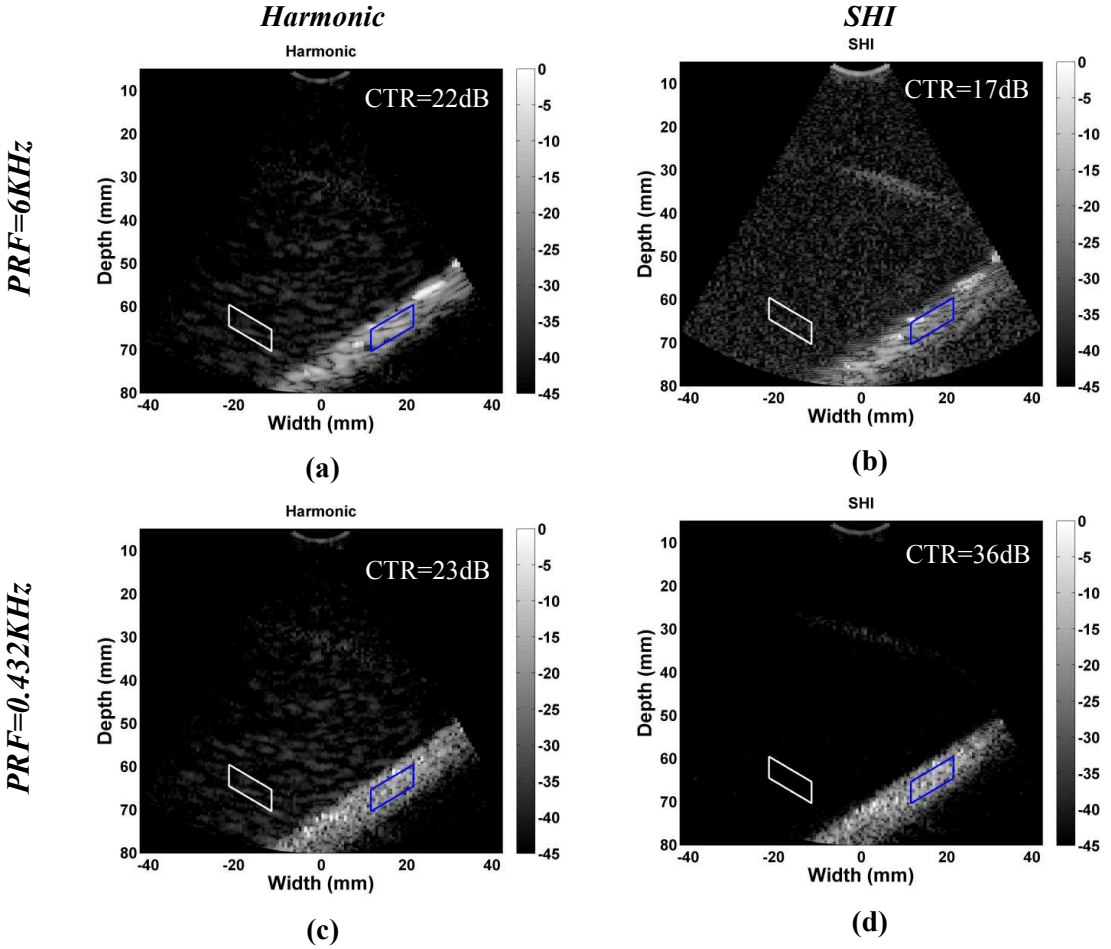


VF-Figure. 4 Les images du second harmonique (a, c) et les images SHI (b, d) d'un fantôme de flux avec circulation d'agent de contraste. Le PRF est de 6 kHz (a, b) et de 0,432 kHz (c, d). La vitesse d'écoulement moyenne nominale est de 8,3 ± 0,7 cm/s. Pour chaque image, le CTR est calculé entre l'amplitude moyenne dans la région de l'UCA et dans la région de tissu.

VF-Figure. 4.d présente un contraste plus fort que VF-Figure. 4.b. Quand $PRI_{SHI}$ est de 6 kHz, le CTR est passée de 22 dB dans l'image du second harmonique à 17 dB dans l'image de SHI. Toutefois, lorsque le $PRI_{SHI}$ est 0.432 kHz, le CTR est passée de 23 dB dans l'image du second harmonique à 36 dB dans l'image de SHI. Autrement dit, ΔCTR est passé de -5 dB lorsque $PRI_{SHI}$ est de 6 kHz, à 13 dB lorsque $PRI_{SHI}$ est de 0.432 kHz. L'amélioration de ΔCTR atteint 18 dB. Cette observation montre que avec des bulles circulantes, l'effet de l'imagerie SHI varie selon la $PRI_{SHI}$ des

impulsions émises. Par conséquent, l'effet de l'imagerie SHI peut être garanti et amélioré par le contrôle du $PRI_{SHI}$, lorsque la vitesse d'écoulement est connue.

Pour énoncer clairement l'amélioration de CTR de la méthode de SHI avec diverses valeurs de $PRI_{SHI}$, les courbes de CTR-différence entre l'image SHI et l'image harmonique correspondant pour différentes valeurs de $PRI_{SHI}$ sont présentées en VF-Figure. 5.a pour quatre vitesses moyennes de flux différentes: 2,8 cm/s, 5,5 cm/s, 8,3 cm/s et 12,7 cm/s (écart type de 0,7 cm/s). Ces valeurs de vitesses sont données par le fabricant du fantôme. Le $PRI_{SHI}$ peut également être représenté comme le rapport entre le déplacement des bulles et la longueur d'onde transmise, et des résultats sont présentés dans la VF-Figure. 5.b. Cette définition considère la projection de la composante de vitesse d'écoulement dans la direction de propagation de l'onde, et non de la vitesse d'écoulement nominale du fluide dans le fantôme. Pour chaque $PRI_{SHI}$, 10 images de SHI sont acquises, la valeur moyenne et l'écart type de ΔCTR sont calculés. Les quatre courbes obtenues présentent des formes similaires, ce qui démontre l'efficacité de l'augmentation de CTR dans l'image de SHI en contrôlant le $PRI_{SHI}$. Pour les quatre vitesses différentes, bien que le meilleur ΔCTR ait lieu à différents $PRI_{SHI}$, il se produit toujours lorsque le mouvement de la bulle est à environ 0.075 λ. Le meilleur ΔCTR moyen est d'environ 12 dB. En théorie, la valeur maximale de ΔCTR survient lorsque le mouvement de la bulle est de 0,125 λ. Ce décalage provient de l'écart entre la vitesse moyenne d'écoulement de l'eau prédéfinie et la vitesse moyenne réelle de la bulle. Plusieurs autres sources d'erreur peuvent également être identifiées: le profil réel de l'écoulement et la force de radiation en raison des transmissions successives, modifient légèrement les vitesses de bulles [Vos *et al.* (2007)].

Des expériences *in-vivo* obtenues sur des rats blancs d'environ 200 g ont également été réalisées. Pour chaque groupe d'acquisitions, 0,25 ml d'agent de contraste Sonovue (Bracco, Genève, Suisse) est injecté dans le système de circulation sanguin à partir de la queue.

La plate-forme ouverte UlaOp, associée à la sonde linéaire LA523 (Esaote, Italie), est utilisée pour transmettre des impulsions. La sonde présente une fréquence centrale de 7 MHz. Les impulsions émises sont sinusoïdales comportant 7-cycles à 5 MHz avec une enveloppe de Hanning. Ces impulsions avec une phase de 0° et de 90° sont transmises pour la mise en œuvre de SHI. Les signaux reçus correspondant à des impulsions transmises à 90° déphasés sont additionnés et filtrés dans la bande du second harmonique pour former des images de SHI. La PRF est réglée pour obtenir des images de SHI avec différents déplacements des bulles.

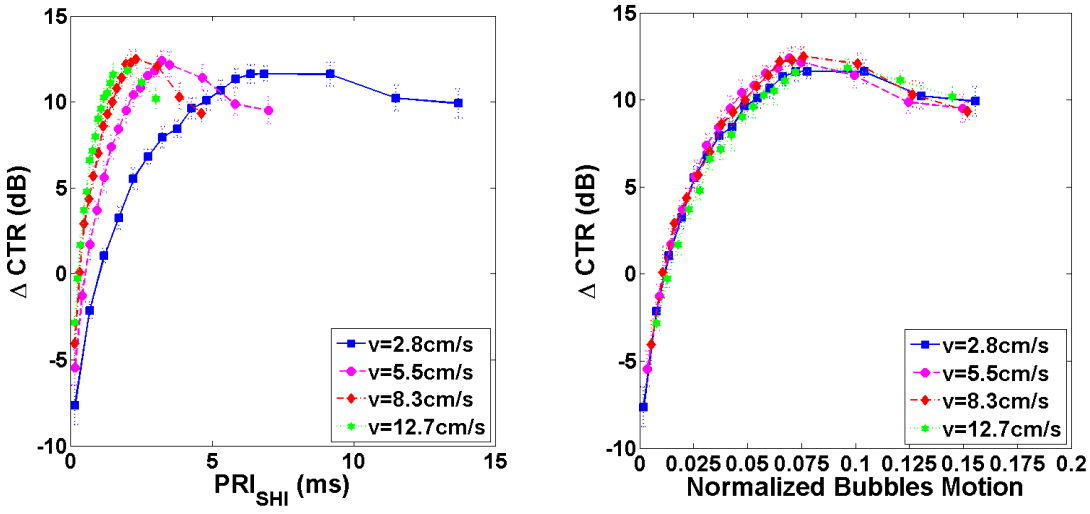


(a) (b)

VF-Figure. 5 CTR-différence entre les images de SHI et les images de seconds harmoniques correspondantes ($\Delta CTR = CTR_{SHI} - CTR_{Harmonic}$) en fonction du PRI entre deux impulsions SHI (a) ou du mouvement des bulles, normalisés à la longueur d'onde d'émission (b), obtenus sur un fantôme de flux avec circulation d'agent de contraste. Pour chaque PRF, 10 images de SHI sont acquises pour le calcul de la valeur moyenne et de l'écart type de ΔCTR. Les résultats pour quatre vitesses de fluide sont présentés.

VF-Figure. 6 présente les images de second harmonique (a, c) et des images SHI (b, d) acquises avec deux valeurs différentes du PRF. Le PRF est de 6 kHz (a, b) et de 0,592 kHz (c, d) respectivement. La dynamique de ces images est de 40 dB. Pour chaque image, le CTR est calculé comme le rapport de l'amplitude moyenne dans la région du vaisseau sanguin et dans la région du tissu, et est exprimée en dB. Dans la VF-Figure. 6.b, les deux signaux dans la région du vaisseau sanguin et la région tissulaire sont d'une amplitude réduite. Dans la VF-Figure. 6.d, les signaux provenant de la région du vaisseau sanguin sont renforcés tandis que les signaux provenant de la zone de tissu sont réduits, ce qui conduit à un meilleur CTR que pour l'image de second harmonique. VF-Figure. 7 est la courbe correspondant au ΔCTR en fonction de $PRI_{SHI}$, obtenue à partir d'images acquises avec 17 valeurs différentes de $PRI_{SHI}$. Le calcul de ΔCTR est le même que dans la partie précédente. VF-Figure. 7 montre clairement que ΔCTR augmente avec l'augmentation du $PRI_{SHI}$.

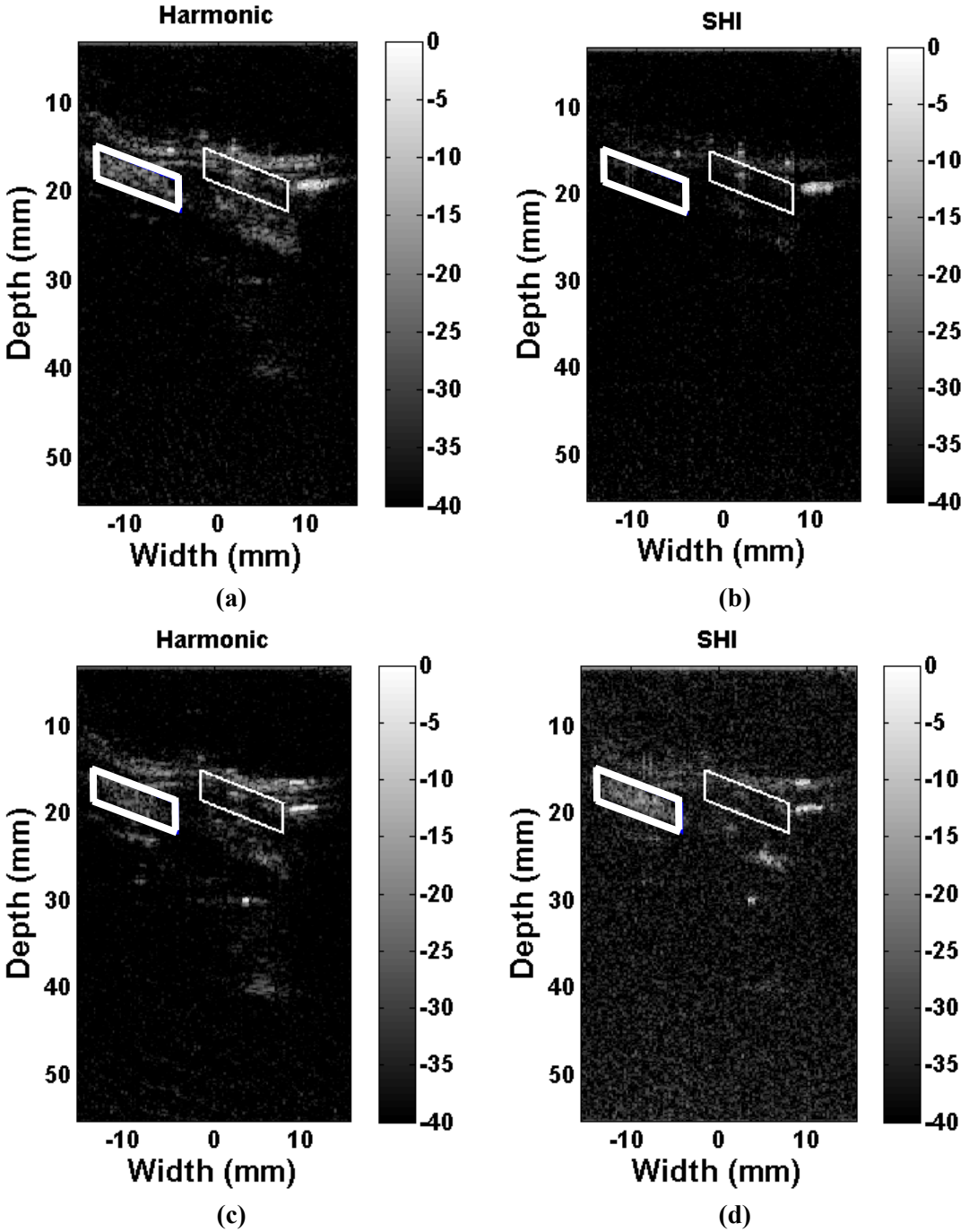


VF-Figure. 6 Les images *in-vivo* de second harmonique (a, c) et de SHI (b, d) à partir d'un rat, avec un agent de contraste circulant dans le vaisseau sanguin, en utilisant une sonde linéaire. Le PRF est de 6 kHz (a, b) ou de 0,592 kHz (c, d). Pour chaque image, le CTR est calculée entre l'amplitude moyenne de la région du vaisseau sanguin (cadre épais) et de la région de tissu (cadre fin).

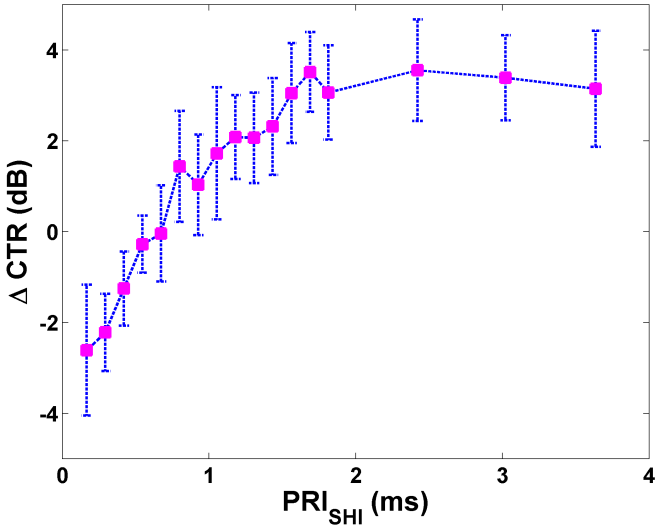


VF-Figure. 7 Résultats *in-vivo*: CTR-différence entre les images de SHI et les images de seconds harmoniques correspondantes ($\Delta CTR = CTR_{SHI} - CTR_{Harmonic}$) par rapport au PRI entre deux impulsions de SHI, obtenue sur un rat avec circulation d'UCA dans le vaisseau sanguin. Pour chaque PRF, 10 images de SHI sont acquises pour le calcul de la valeur moyenne et de l'écart type de ΔCTR.

Les résultats expérimentaux sur une seule bulle, obtenus avec une sonde mono élément, confirment que lorsque des bulles se déplacent dans la direction de propagation de l'onde, l'amplitude de l'harmonique de SHI change périodiquement avec l'augmentation des mouvements de bulles entre les deux impulsions déphasées de 90°, et la valeur maximale apparaît d'abord lorsque le mouvement de la bulle est de 0.125 λ. Des résultats expérimentaux sur une population de bulles dans un fantôme de flux démontrent en outre que la qualité d'image SHI peut être garantie et améliorée dans le cas des bulles en mouvement lorsque un $PRI_{SHI}$ approprié est choisi, si le flux n'est pas perpendiculaire à la direction de propagation des ondes. La meilleure amélioration de CTR atteint environ 12 dB par rapport à une image de second harmonique. Les résultats expérimentaux *in-vivo* sont en accord avec les résultats expérimentaux *in-vitro*, même si l'amélioration du CTR atteint seulement 3.2 dB en raison de la présence d'un mouvement tissulaire.

Tous ces résultats expérimentaux valident le fait que le décalage de phase des échos rétrodiffusés à partir de bulles dépend du décalage de phase des transmissions, et montre comment le mouvement de la bulle influence l'efficacité d'une technique d'impulsions multiples.

Le travail présenté encourage le développement des techniques d'imagerie multi-impulsions avec contrôle automatique du décalage de phase entre impulsions consécutives ou du PRI pour optimiser la technique mise en œuvre et améliorer la qualité d'image.

Ces travaux ont été présentés dans un article de revue accepté par *IEEE TUFFC* [Lin et al., 2013a], et dans les congrès *IEEE IUS* [Lin *et al*., 2012b], *Acoustics 2012* [Lin *et al*., 2012a] et *Imageries du vivant* [Lin *et al*., 2012e].

## 7. Double inversion d'impulsions

Cette partie propose une nouvelle stratégie, appelée *double pulse inversion* (DPI), en appliquant deux fois la technique PI, afin de réduire les harmoniques générés par les tissus et améliorer le CTR. Des impulsions en opposition de phase sont transmises à la région d'intérêt (ROI). Tout d'abord, une acquisition PI est réalisée avant l'arrivée du produit de contraste. Les informations portées par cette image correspondent aux harmoniques produits par les tissus environnant le vaisseau. Une deuxième acquisition est réalisée après l'arrivée de l'agent de contraste. Les signaux de PI résultant représentent à la fois les harmoniques de tissu et les harmoniques de l'agent de contraste. Ensuite, les signaux résultants de PI, obtenus avant et après la présence de l'agent de contraste sont soustraits pour supprimer les signaux harmoniques produits par les tissus.

VF-Figure. 8 présente l'image PI et l'image DPI. Le CTR est calculé à partir des signaux moyennés dans la région de l'agent de contraste et la région tissulaire. VF-Figure. 8 montre également que l'image DPI a un meilleur contraste que l'image PI. Le CTR est passée de 23 dB dans l'image PI à 28 dB dans l'image DPI, ce qui signifie une amélioration du CTR d'environ 5 dB.

Pour énoncer clairement la réduction des signaux harmoniques de tissu par cette méthode, les spectres d'une ligne RF de DPI et PI sont présentés ensemble dans VF-Figure. 9. VF-Figure. 9.a est le spectre dans la région de tissu environnant, une réduction de l'amplitude sans la bande du second harmonique a pu être observée après l'utilisation de DPI. VF-Figure. 9.b est le spectre dans la région de l'agent de contraste, où l'amplitude du spectre reste inchangée. Par conséquent, le CTR est augmenté.

VF-Figure. 10 et VF-Figure. 11 présentent les résultats expérimentaux *in-vivo* obtenus sur des rats blancs d'environ 200 g. La plate-forme ouverte UlaOp, associée à la sonde linéaire LA523 (Esaote, Italie), est utilisée pour transmettre des impulsions. Les impulsions émises sont de 7 cycles sinusoïdaux à 5 MHz avec une enveloppe de Hanning. Avant et après l'injection, l'image PI est acquise respectivement. Pour chaque injection, 0,25 mL Sonovue UCA (Bracco, Genève, Suisse) est utilisé.

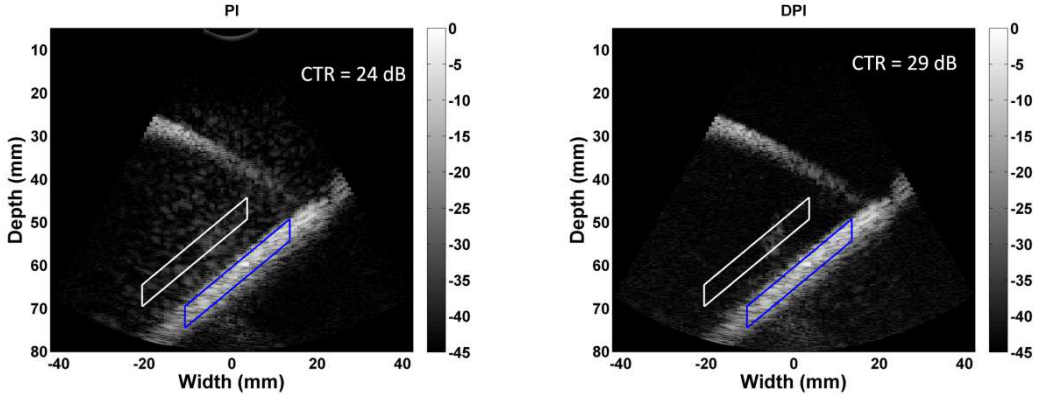


VF-Figure. 8 Résultats expérimentaux *in-vitro*: l'image PI (a) et l'image DPI (b) d'un fantôme avec UCA circulant. Le CTR est calculé à partir des signaux moyennés de la région de l'agent de contraste (à l'intérieur de la ligne bleue) et dans la région de tissu (au sein de la ligne blanche). Le CTR est amélioré d'environ 5 dB.

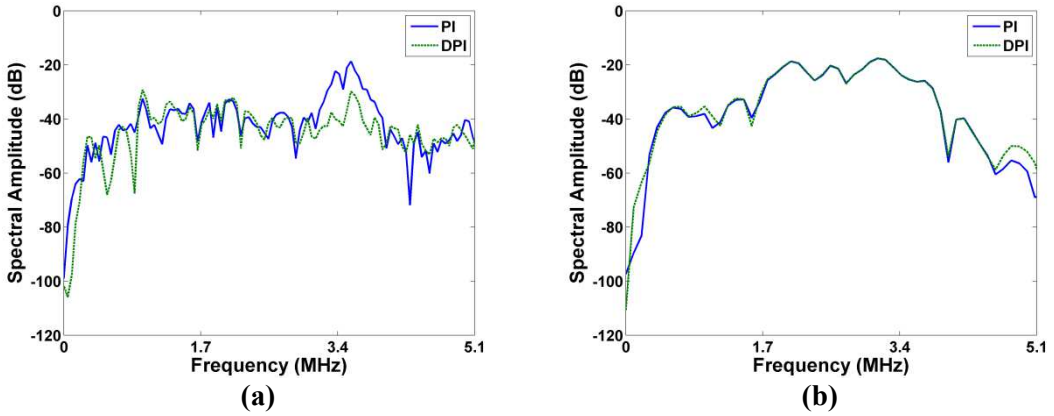


VF-Figure. 9 Le spectre de la ligne centrale à partir d'un fantôme de flux avec circulation de l'agent de contraste; l'amplitude du spectre est normalisé à l'amplitude fondamentale de la réponse à une seule impulsion; les spectres des signaux de PI (ligne continue) et DPI (ligne en pointillés) dans la région de tissu (a) et dans la région de l'agent de contraste (b) sont présentés. La fréquence fondamentale est de 1,7 MHz.

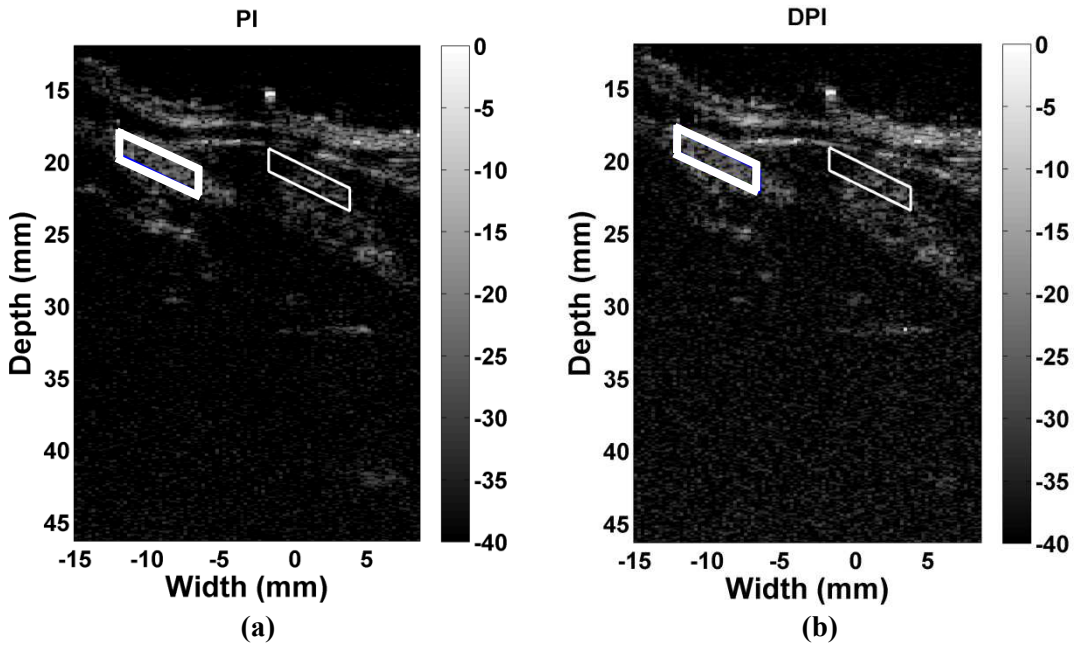


VF-Figure. 10 Résultats expérimentaux *in-vivo*: l'image PI (a) et l'image DPI (b) d'un rat avec UCA dans le vaisseau sanguin. Le CTR est calculée à partir des signaux moyennés de la région de l'agent de contraste (au sein de la ligne bleue) et dans la région de tissu (au sein de la ligne blanche).

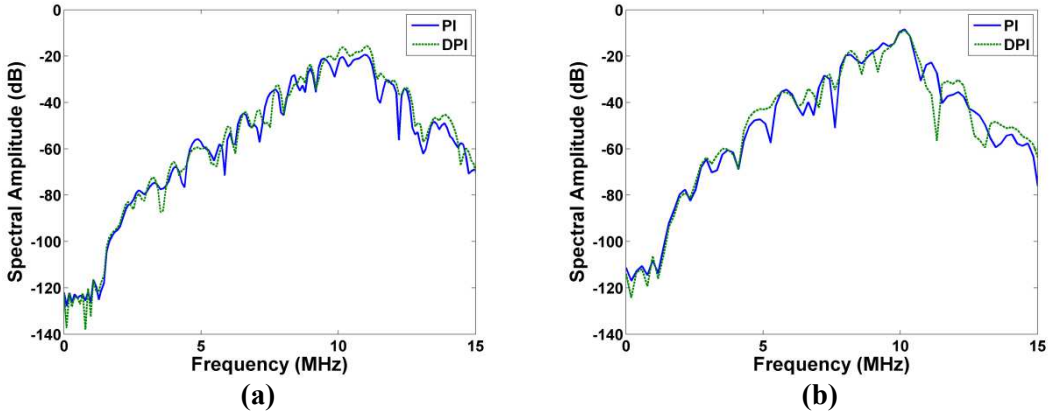


VF-Figure. 11 Le spectre de la ligne centrale d'une image de rat, l'amplitude du spectre est normalisée à l'amplitude fondamentale de la réponse à une seule impulsion, les signaux de PI (ligne continue) et DPI (ligne en pointillés) pour la région de tissu (a) et pour la région de l'agent de contraste (b) sont présentés. La fréquence fondamentale est de 5 MHz.

L'image PI et l'image DPI sont présentées dans VF-Figure. 10. Les spectres d'une ligne RF, dans la région de l'agent de contraste et dans la région du tissu, respectivement, sont présentés dans VF-Figure. 11.

VF-Figure. 10 montre que la valeur de CTR dans l'image DPI n'est pas améliorée, contrairement aux expériences *in-vitro*. De l'analyse du signal dans VF-Figure. 11, la réduction du tissu-harmonique n'apparait pas détectable (VF-Figure. 11.a). Cela

provient probablement de la présence de mouvement des tissus, ce qui rend la technique inefficace.

Ce travail a été partiellement présenté à la conférence *IEEE IUS* [Lin *et al*., 2012c].

## IV. Conclusion

Ce travail propose d'abord une généralisation de la plupart des techniques multi-impulsions en imagerie de contraste ultrasonore. La formulation présentée permet de prédire les composants non-linéaires dans chaque bande de fréquence et de concevoir de nouvelles séquences de transmission pour augmenter ou diminuer des composants non-linéaires spécifiés dans chaque bande harmonique. Des simulations sur plusieurs techniques multi-impulsions ont été faites et ont été comparées avec les résultats expérimentaux donnés dans la littérature. L'accord entre la simulation et les résultats expérimentaux valide la généralisation d'une telle formulation pour les transmissions multi-impulsions.

Ensuite, l'influence du mouvement de la bulle sur des techniques multi-impulsions a été étudiée. Des simulations, des expériences *in-vitro* à partir d'une seule bulle et de nuages de bulles, et des expériences *in-vivo* à partir de rats blancs ont été réalisées. Tous ces résultats montrent que le déphasage des échos rétrodiffusés par des bulles dépend du déphasage des transmissions, et que le mouvement de la bulle influence l'efficacité des techniques multi-impulsions. Les amplitudes du fondamental et du second harmonique des signaux sommés changent périodiquement, présentant des valeurs maximales ou minimales, selon le déplacement des diffuseurs entre deux acquisitions. En outre, les résultats expérimentaux basés sur l'inversion du second harmonique (SHI) révèlent que le mouvement de la bulle peut être pris en compte pour régler la fréquence de répétition des impulsions (PRF). Avec le PRF optimal, le CTR des images de SHI peut être amélioré par rapport aux images standards de second harmonique.

Par ailleurs, une nouvelle technique, appelée double pulse inversion (DPI), a également été proposée. La technique PI est appliquée deux fois avant et après l'arrivée de l'agent de contraste dans la région d'intérêt. La soustraction des signaux de PI vise à supprimer les harmoniques générées par les tissus et à améliorer le CTR. Les simulations et les résultats expérimentaux *in-vitro* ont montré une amélioration du CTR par la technique DPI. Cependant, les résultats *in-vivo* expérimentaux confirment que le mouvement des tissus lors de l'acquisition est un obstacle inévitable de cette technique.

# PUBLICATIONS

## Journal article

[Lin *et al*., 2013a] **F. Lin**, C. Cachard, R. Mori, F. Varray, F. Guidi and O. Basset, "Ultrasound Contrast Imaging: Influence of Scatterer motion in Multi-pulse Techniques*", IEEE Transactions on Ultrasonics, Ferroelectrics, and Frequency Control,* vol. 60, no. 10, pp. 2065-2078

[Lin *et al*., 2013b] **F. Lin**, C. Cachard, F. Varray and O. Basset, "Generalization of Multi-pulse Transmission Techniques for Ultrasound Imaging*", Ultrasonics, Submitted*

## International conference paper

[Lin *et al*., 2013c] **F. Lin**, J. Sanchez, C. Cachard , O. Basset and R. Lavarello, "First experimental implementation of a bandwidth enhancement pulse compression technique on an ultrasound array imaging system", *IEEE International Symposium on Biomedical Imaging* , *Submitted*

[Lin *et al*., 2012c] **F. Lin**, C. Cachard, A. Bernard, A. Guibal, F. Varray and O. Basset, "Double Pulse Inversion Imaging for Ultrasound Contrast Imaging*", IEEE International Ultrasonics Symposium,* Dresden, Germany, pp. 1307-1310, 2012

[Lin *et al*., 2012b] **F. Lin**, C. Cachard, R. Mori, J. Viti, F. Varray, F. Guidi and O. Basset, "Influences of Bubble Motion to Second-Harmonic Inversion Imaging", *IEEE International Ultrasonics Symposium*, Dresden, Germany, pp. 675-678, 2012

[Lin *et al*., 2012a] **F. Lin**, C. Cachard, F. Varray and O. Basset, "Investigation into the effectiveness of ultrasound SHI Imaging according to static and dynamic parameters of contrast agents", *Acoustics,* Nantes, France, pp. 1605-1610, 2012

[Lin *et al*., 2011] **F. Lin**, F. Varray, A. Guibal, C. Cachard, and O. Basset, Experimental Implementation of the Second Harmonic Inversion Imaging on an Open Ultrasonic Scanner", *IEEE International Ultrasonics Symposium*, Orlando, USA, pp. 2440-2443, 2011

## National communication

[Lin *et al*., 2012e] **F. Lin**, C. Cachard, A. Bernard and O. Basset, "Optimization of Multi-pulse Methods in Ultrasound Contrast Imaging", *Imagerie-vivant: Nouvelles méthodologies en imagerie du vivant*, Lyon, France, Dec. 11-13, 2012

[Lin *et al*., 2012d] **F. Lin**, C. Cachard and O. Basset, "Improvement of ultrasound contrast harmonic imaging*", Journées scientifique 2012: New investigations and innovative techniques in imaging and therapy ultrasound,* Lyon, France, Oct. 15-16, 2012

# BIBLIOGRAPHIES

[Aanonsen *et al.*, (1984)] Aanonsen, T. Barkve, J. N. Tjøtta, and S. Tjøtta. Distortion and Harmonic Generation in the Nearfield of a Finite Amplitude Sound Beam. *J Acoust Soc Am*, 1984, vol. 75, no. 3, pp. 749–768

[Allen *et al.*, (2002)] Allen, D. J. May, and K. W. Ferrara. Dynamics of Therapeutic Ultrasound Contrast Agents. *Ultrasound in Medicine & Biology*, 2002, vol. 28, no. 6, pp. 805–816

[Beyer, (1960)] Beyer. Parameter of Nonlinearity in Fluids. *J Acoust Soc Am*, 1960, vol. 32, no. 6, pp. 719–721

[Borsboom *et al.*, (2009)] Borsboom, A. Bouakaz, and N. De Jong. Pulse Subtraction Time Delay Imaging Method for Ultrasound Contrast Agent Detection. *IEEE Trans Ultrason Ferroelectr Freq Control*, 2009, vol. 56, no. 6, pp. 1151–1158

[Bouakaz *et al.*, (2003)] Bouakaz and N. de Jong. Native Tissue Imaging at Superharmonic Frequencies. *IEEE Trans Ultrason Ferroelectr Freq Control*, 2003, vol. 50, no. 5, pp. 496–506

[Bouakaz *et al.*, (2002)] Bouakaz, S. Frigstad, F. J. Ten Cate, and N. De Jong. Super Harmonic Imaging: a New Imaging Technique for Improved Contrast Detection. *Ultrasound Med Biol*, 2002, vol. 28, no. 1, pp. 59–68

[Brock-Fisher *et al.*, (1996)] Brock-Fisher, M. D. Poland, and P. G. Rafter. Means for Increasing Sensitivity in Non-linear Ultrasound Imaging Systems. *US Patent 5,577,505*, 1996

[Burgers, (1948)] Burgers. A Mathematical Model Illustrating the Theory of Turbulence. *Advances In Applied Mechanics*, 1948, vol. 1, pp. 171–199

[Burns *et al.*, (1992)] Burns, J. E. Powers, and T. Fritzsch. Harmonic Imaging: a New Imaging and Doppler Method for Contrast Enhanced Ultrasound. *Radiology*, 1992, vol. 185, pp. 142–142

[Burns *et al.*, (1996)] Burns, J. E. Powers, D. Hope Simpson, V. Uhlendorf, and T. Fritzsch. Harmonic Imaging: Principles and Preliminary Results. *Angiology*, 1996, vol. 47, no. 7, pp. S63–S74

[Burns *et al.*, (1994)] Burns, J. E. Powers, D. H. Simpson, A. Brezina, A. Kolin, C. T. Chin, V. Uhlendorf, and T. Fritzsch. Harmonic Power Mode Doppler Using

Microbubble Contrast Agents: An Improved Method For Small Vessel Flow Imaging. *IEEE Ultrasonics Symposium*, 1994, vol. 3, pp. 1547–1550

[Chiao *et al.*, (2003)] Chiao and X. H. Hao. Coded Excitation for Diagnostic Ultrasound: a System Developer's Perspective. *IEEE Ultrasonics Symposium*, 2003, vol. 52, no. 2, pp. 160–170

[Christopher, (1999)] Christopher. Source Prebiasing for Improved Second Harmonic Bubble-response Imaging. *IEEE Trans Ultrason Ferroelectr Freq Control*, 1999, vol. 46, no. 3, pp. 556–563

[Church, (1995)] Church. The Effects of an Elastic Solid Surface Layer on the Radial Pulsations of Gas Bubbles. *J Acoust Soc Am*, 1995, vol. 97, no. 3, pp. 1510–1521

[Couture *et al.*, (2008)] Couture, J. F. Aubry, G. Montaldo, M. Tanter, and M. Fink. Suppression of Tissue Harmonics for Pulse-inversion Contrast Imaging Using Time Reversal. *Phys Med Biol*, 2008, vol. 53, pp. 5469–5480

[Crocco *et al.*, (2009)] Crocco, M. Palmese, C. Sciallero, and A. Trucco. A Comparative Analysis of Multi-pulse Techniques in Contrast-enhanced Ultrasound Medical Imaging. *Ultrasonics*, 2009, vol. 49, no. 1, pp. 120–125

[De Jong, (1993)] de Jong. Acoustic Properties of Ultrasound Contrast Agents. Erasmus University Rotterdam, 1993

[De Jong *et al.*, (1994a)] De Jong, R. Cornet, and C. Lancee. Higher Harmonics of Vibrating Gas-filled Microspheres. Part One: Simulations. *Ultrasonics*, 1994, vol. 32, no. 6, pp. 447–453

[De Jong *et al.*, (1994b)] De Jong, R. Cornet, and C. Lancee. Higher Harmonics of Vibrating Gas-filled Microspheres. Part Two: Measurements. *Ultrasonics*, 1994, vol. 32, no. 6, pp. 455–459

[De Jong *et al.*, (2007)] de Jong, M. Emmer, C. T. Chin, A. Bouakaz, F. Mastik, D. Lohse, and M. Versluis. "Compression-only" Behavior of Phospholipid-coated Contrast Bubbles. *Ultrasound Med Biol*, 2007, vol. 33, no. 4, pp. 653–656

[De Jong *et al.*, (1993)] de Jong and L. Hoff. Ultrasound Scattering Properties of Albunex Microspheres. *Ultrasonics*, 1993, vol. 31, no. 3, pp. 175–181

[De Jong *et al.*, (1992)] De Jong, L. Hoff, T. Skotland, and N. Bom. Absorption and Scatter of Encapsulated Gas Filled Microspheres: Theoretical Considerations and Some Measurements. *Ultrasonics*, 1992, vol. 30, no. 2, pp. 95–103

[Duck, (1990)] Duck. Physical Properties of Tissue: a Comprehensive Reference Book. Academic Press, 1990,

[Eckersley *et al.*, (2005)] Eckersley, C. T. Chin, and P. N. Burns. Optimising Phase and Amplitude Modulation Schemes for Imaging Microbubble Contrast Agents at Low Acoustic Power. *Ultrasound Med Biol*, 2005, vol. 31, no. 2, pp. 213–219

[Faez *et al.*, (2013)] Faez, M. Emmer, K. Kooiman, M. Versluis, A. van der Steen, and N. de Jong. 20 Years of Ultrasound Contrast Agent Modeling. *IEEE Trans Ultrason Ferroelectr Freq Control*, 2013, vol. 60, no. 1, pp. 7–20

[Forsberg *et al.*, (2000)] Forsberg, W. T. Shi, and B. . Goldberg. Subharmonic Imaging of Contrast Agents. *Ultrasonics*, 2000, vol. 38, no. 1, pp. 93–98

[Frinking *et al.*, (2000)] Frinking, A. Bouakaz, J. Kirkhorn, T. Cate, J. Folkert, and N. De Jong. Ultrasound Contrast Imaging: Current and New Potential Methods. *Ultrasound Med Biol*, 2000, vol. 26, no. 6, pp. 965–975

[Frinking *et al.*, (2001)] Frinking, E. I. Cespedes, J. Kirkhorn, H. G. Torp, and N. de Jong. A New Ultrasound Contrast Imaging Approach Based on the Combination of Multiple Imaging Pulses and a Separate Release Burst. *IEEE Trans Ultrason Ferroelectr Freq Control*, 2001, vol. 48, no. 3, pp. 643–651

[Fubini, (1935)] Fubini. Anomalie Nella Propagazione Diffonde Acustiche Di Grande Ampiezza. *Alta Freq*, 1935, vol. 4, p. 530

[Gramiak *et al.*, (1968)] Gramiak and P. M. Shah. Echocardiography of the Aortic Root. *Invest Radiol*, 1968, vol. 3, no. 5, pp. 356–366

[Haider *et al.*, (1999)] Haider and R. Y. Chiao. Higher Order Nonlinear Ultrasonic Imaging. *IEEE Ultrasonics Symposium*, 1999, vol. 2, pp. 1527–1531

[Hamilton, (1988)] Hamilton. On the Coefficient of Nonlinearity β in Nonlinear Acoustics. *J Acoust Soc Am*, 1988, vol. 83, no. 1, p. 74

[Hoff *et al.*, (2000)] Hoff, P. Sontum, and J. M. J. Hovem. Oscillations of Polymeric Microbubbles: Effect of the Encapsulating Shell. *J Acoust Soc Am*, 2000, vol. 107, no. 4, pp. 2272–2280

[Hwang, (1999)] Hwang. Two Pulse Technique for Ultrasonic Harmonic Imaging. *US Patent 5,951,478*, 1999

[Keller *et al.*, (1989)] Keller, S. S. Segal, S. Kaul, and B. Duling. The Behavior of Sonicated Albumin Microbubbles Within the Microcirculation: a Basis for Their

Use During Myocardial Contrast Echocardiography. *Circulation Research*, 1989, vol. 65, no. 2, pp. 458–467

[KB Krishnan *et al.*, (2008)] K. B. Krishnan and K. E. Thomenius. Improved Contrast Ultrasound with Tissue Harmonic Minimizing Pulse. *IEEE Trans Ultrason Ferroelectr Freq Control*, 2008, vol. 55, no. 1, pp. 249–253

[S Krishnan *et al.*, (1998)] S. Krishnan, J. D. Hamilton, and M. O'Donnell. Suppression of Propagating Second Harmonic in Ultrasound Contrast Imaging. *IEEE Trans Ultrason Ferroelectr Freq Control*, 1998, vol. 45, no. 3, pp. 704–711

[S Krishnan *et al.*, (1996)] S. Krishnan and M. O'Donnell. Transmit Aperture Processing for Nonlinear Contrast Agent Imaging. *Ultrason Imaging*, 1996, vol. 18, no. 2, pp. 77–105

[Leighton, (1994)] Leighton. The Acoustic Bubble. Academic Press, 1994, 613 p. ISBN 012441908

[Lindner, (2001)] Lindner. Targeted Ultrasound Contrast Agents: Diagnostic and Therapeutic Potential. *IEEE Ultrasonics Symposium*, 2001. 2001, pp. 1695–1703

[Logean *et al.*, (2003)] Logean, L. Schmetterer, and C. E. Riva. Velocity Profile of Red Blood Cells in Human Retinal Vessels Using Confocal Scanning Laser Doppler Velocimetry. *Laser Methods in Medicine and Biology*, 2003, vol. 13, no. 1, pp. 45–51

[Mahue *et al.*, (2011)] Mahue, J. M. J. M. Mari, R. J. R. Eckersley, and M.-X. Tang. Comparison of Pulse Subtraction Doppler and Pulse Inversion Doppler. *IEEE Trans Ultrason Ferroelectr Freq Control*, 2011, vol. 58, no. 1, pp. 73–81

[Marmottant *et al.*, (2005)] Marmottant, S. van der Meer, M. Emmer, M. Versluis, N. de Jong, S. Hilgenfeldt, and D. Lohse. A Model for Large Amplitude Oscillations of Coated Bubbles Accounting for Buckling and Rupture. *J Acoust Soc Am*, 2005, vol. 118, no. 6, p. 3499

[Morgan *et al.*, (1998)] Morgan, M. Averkiou, and K. Ferrara. The Effect of the Phase of Transmission on Contrast Agent Echoes. *IEEE Trans Ultrason Ferroelectr Freq Control*, 1998, vol. 45, no. 4, pp. 872–875

[Noltingk *et al.*, (1950)] Noltingk and E. Neppiras. Cavitation Produced by Ultrasonics. *Proceedings of the Physical Society. Section B*, 1950. 1950, pp. 674–685

[Novell *et al.*, (2009)] Novell, M. Legros, N. Felix, and A. Bouakaz. Exploitation of Capacitive Micromachined Transducers for Nonlinear Ultrasound Imaging. *IEEE Trans Ultrason Ferroelectr Freq Control*, 2009, vol. 56, no. 12, pp. 2733–2743

[Pasovic *et al.*, (2011)] Pasovic, M. Danilouchkine, T. Faez, P. L. M. J. van Neer, C. Cachard, A. F. W. van der Steen, O. Basset, and N. de Jong. Second Harmonic Inversion for Ultrasound Contrast Harmonic Imaging. *Phys Med Biol*, 2011, vol. 56, no. 11, pp. 3163–3180

[Pasovic *et al.*, (2010)] Pasovic, M. Danilouchkine, G. Matte, V. Der Steen, A. FW, O. Basset, N. De Jong, and C. Cachard. Broadband Reduction of the Second Harmonic Distortion During Nonlinear Ultrasound Wave Propagation. *Ultrasound Med Biol*, 2010, vol. 36, no. 10, pp. 1568–1580

[P Phillips *et al.*, (2004)] P. Phillips and E. Gardner. Contrast-agent Detection and Quantification. *Eur Radiol*, 2004, vol. 14, pp. 4–10

[PJ Phillips, (2001)] P. J. Phillips. Contrast Pulse Sequences (CPS): Imaging Nonlinear Microbubbles. *IEEE Ultrasonics Symposium*, 2001, vol. 2, pp. 1739–1745

[Plesset, (1949)] Plesset. The Dynamics of Cavitation Bubbles. *J. Appl. Mech*, 1949, vol. 16, no. 3, pp. 227–282

[Poritsky, (1952)] Poritsky. The Collapse or Growth of a Spherical Bubble or Cavity in a Viscous Fluid. *First U.S. National Congress on Applied Mechanics*, 1952. 1952, pp. 813–821

[Porter *et al.*, (2010)] Porter and F. Xie. Myocardial Perfusion Imaging with Contrast Ultrasound. *JACC Cardiovasc Imaging*, 2010, vol. 3, no. 2, pp. 176–187

[Rayleigh, (1917)] Rayleigh. On the Pressure Developed in a Liquid During the Collapse of a Spherical Cavity. *Phil Mag*, 1917, vol. 34, no. 200, pp. 94–98

[Reddy *et al.*, (2002)] Reddy and A. J. Szeri. Optimal Pulse-inversion Imaging for Microsphere Contrast Agents. *Ultrasound Med Biol*, 2002, vol. 28, no. 4, pp. 483–494

[Ricci *et al.*, (2007)] Ricci, L. Bassi, E. Boni, A. Dallai, and P. Tortoli. Multichannel FPGA-based Arbitrary Waveform Generator for Medical Ultrasound. *Electronics Letters*, 2007, vol. 43, no. 24, pp. 1335–1336

[Ricci *et al.*, (2006)] Ricci, E. Boni, F. Guidi, T. Morganti, and P. Tortoli. A Programmable Real-time System for Development and Test of New Ultrasound

Investigation Methods. *IEEE Trans Ultrason Ferroelectr Freq Control*, 2006, vol. 53, no. 10, pp. 1813–1819

[Shen *et al.*, (2008a)] Shen and Y. C. Hsieh. Optimal Transmit Phasing on Tissue Background Suppression in Contrast Harmonic Imaging. *Ultrasound Med Biol*, 2008, vol. 34, no. 11, pp. 1820–1831

[Shen *et al.*, (2002)] Shen and P. C. Li. Motion Artifacts of Pulse Inversion-based Tissue Harmonic Imaging. *IEEE Trans Ultrason Ferroelectr Freq Control*, 2002, vol. 49, no. 9, pp. 1203–1211

[Shen *et al.*, (2011)] Shen and T. Y. Shi. Third Harmonic Transmit Phasing for SNR Improvement in Tissue Harmonic Imaging with Golay-encoded Excitation. *Ultrasonics*, 2011, vol. 51, no. 5, pp. 554–560

[Shen *et al.*, (2008b)] Shen, H. W. Wang, and Y. Y. Chiu. Contrast Harmonic Detection with Chirp Excitation in 3f0 Transmit Phasing. *Ultrason Imaging*, 2008, vol. 30, no. 4, pp. 251–261

[Shen *et al.*, (2007a)] Shen, Y. C. Wang, and Y. C. Hsich. Third Harmonic Transmit Phasing for Tissue Harmonic Generation. *IEEE Trans Ultrason Ferroelectr Freq Control*, 2007, vol. 54, no. 7, pp. 1370–1381

[Shen *et al.*, (2007b)] Shen, Y. C. Wang, and Y. C. Hsieh. A Feasibility Study of Tissue Harmonic Generation with 3f0 Transmit Phasing. *IEEE Ultrasonics Symposium*, 2007. 2007, pp. 1748–1751

[Shen *et al.*, (2010)] Shen, Y. C. Yang, and W. S. Chen. Optimal Transmit Phasing for Harmonic-Background Suppression with Bipolar Square-Wave Pulser. *Ultrason Imaging*, 2010, vol. 47, no. 1, pp. 33– 47

[Simpson *et al.*, (1999)] Simpson, C. T. Chin, and P. N. Burns. Pulse Inversion Doppler: a New Method for Detecting Nonlinear Echoes from Microbubble Contrast Agents. *IEEE Trans Ultrason Ferroelectr Freq Control*, 1999, vol. 46, no. 2, pp. 372–382

[Szabo, (2004)] Szabo. Diagnostic Ultrasound Imaging: Inside Out. Academic Press, 2004, 549 p. ISBN 0126801452

[Tang *et al.*, (2006)] Tang and R. J. Eckersley. Nonlinear Propagation of Ultrasound Through Microbubble Contrast Agents and Implications for Imaging. *IEEE Trans Ultrason Ferroelectr Freq Control*, 2006, vol. 53, no. 12, pp. 2406–2415

[Tangelder *et al.*, (1986)] Tangelder, D. W. Slaaf, a. M. Muijtjens, T. Arts, M. G. oude Egbrink, and R. S. Reneman. Velocity Profiles of Blood Platelets and Red

Blood Cells Flowing in Arterioles of the Rabbit Mesentery. *Circulation Research*, 1986, vol. 59, no. 5, pp. 505–514

[Tortoli *et al.*, (2009)] Tortoli, L. Bassi, E. Boni, A. Dallai, F. Guidi, and S. Ricci. ULA-OP: An Advanced Open Platform for Ultrasound Research. *IEEE Trans Ultrason Ferroelectr Freq Control*, 2009, vol. 56, no. 10, pp. 2207–2216

[Van Neer *et al.*, (2011)] van Neer, M. Danilouchkine, G. Matte, A. van der Steen, and N. de Jong. Dual-pulse Frequency Compounded Superharmonic Imaging. *IEEE Trans Ultrason Ferroelectr Freq Control*, 2011, vol. 58, no. 11, pp. 2316–2324

[Varray *et al.*, (2013)] Varray, O. Basset, P. Tortoli, and C. Cachard. CREANUIS: A Nonlinear Radio Frequency Ultrasound Image Simulator. *Ultrasound Med Biol*, 2013

[Varray *et al.*, (2010)] Varray, C. Cachard, P. Tortoli, and O. Basset. Nonlinear Radio Frequency Image Simulation for Harmonic Imaging: Creanuis. *IEEE Ultrasonics Symposium*, 2010. 2010, pp. 2179 – 2182

[Varray *et al.*, (2011)] Varray, A. Ramalli, C. Cachard, P. Tortoli, and O. Basset. Fundamental and Second-harmonic Ultrasound Field Computation of Inhomogeneous Nonlinear Medium with a Generalized Angular Spectrum Method. *IEEE Trans Ultrason Ferroelectr Freq Control*, 2011, vol. 58, no. 7, pp. 1366–1376

[Voormolen, (2007)] Voormolen. 3D Harmonic Echocardiogray. Erasmus University Rotterdam, 2007

[Vos *et al.*, (2007)] Vos, F. Guidi, E. Boni, and P. Tortoli. Method for Microbubble Characterization Using Primary Radiation Force. *IEEE Trans Ultrason Ferroelectr Freq Control*, 2007, vol. 54, no. 7, pp. 1333–1345

[VP Kuznetsov, (1970)] VP Kuznetsov. Equation of Nonlinear Acoustics. *Soviet Physics Acoustics*, 1970, vol. 16, pp. 467–470

[Ward *et al.*, (1997)] Ward, A. C. Baker, and V. F. Humphrey. Nonlinear Propagation Applied to the Improvement of Resolution in Diagnostic Medical Ultrasound. *J Acoust Soc Am*, 1997, vol. 101, no. 1, pp. 143–154

[Wilkening *et al.*, (2001)] Wilkening, B. Brendel, H. Jiang, J. Lazenby, and H. Ermert. Optimized Receive Filters and Phase-coded Pulse Sequences for Contrast Agent and Nonlinear Imaging. *IEEE Ultrasonics Symposium*, 2001. 2001, pp. 1733–1737

[Wilkening *et al.*, (2000)] Wilkening and M. Krueger. Phase-coded Pulse Sequence for Non-linear Imaging. *IEEE Ultrasonics Symposium*, 2000, pp. 1559–1562

[Wu *et al.*, (1998)] Wu and J. Tong. Measurements of the Nonlinearity Parameter B/A of Contrast Agents. *Ultrasound Med Biol*, 1998, vol. 24, no. 1, pp. 153–159

[Zabolotskaya *et al.*, (1969)] Zabolotskaya and R. V Khokhlov. Quasi-plane Waves in the Nonlinear Acoustics of Confined Beams. *Soviet Physics Acoustics*, 1969, vol. 15, pp. 35–40

[Zhang *et al.*, (1999)] Zhang and X. Gong. Experimental Investigation of the Acoustic Nonlinearity Parameter Tomography for Excised Pathological Biological Tissues. *Ultrasound Med Biol*, 1999, vol. 25, no. 4, pp. 593–599

[Zhang *et al.*, (2001)] Zhang, X. Gong, and X. Chen. Experimental Imaging of the Acoustic Nonlinearity Parameter B/A for Biological Tissues via a Parametric Array. *Ultrasound Med Biol*, 2001, vol. 27, no. 10, pp. 1359–1365

FOLIO ADMINISTRATIF

THESE SOUTENUE DEVANT L'INSTITUT NATIONAL DES SCIENCES APPLIQUEES DE LYON

**NOM** : LIN **DATE de SOUTENANCE** : 14/11/2013

**Prénoms** : Fanglue

**TITRE** : Ultrasound Contrast Imaging with Multi-pulse Transmission

**NATURE** : Doctorat **Numéro d'ordre** : 2013ISAL0117

**Ecole doctorale** : Electronique, Electrotechnique, Automatique

**Spécialité :**

**RESUME** :

In ultrasound imaging domain, nonlinear imaging, which utilizes the nonlinear backscattered signals, has become an important branch. Nonlinear imaging, also named harmonic imaging, can be divided into tissue harmonic imaging and contrast harmonic imaging, according to where the nonlinear signals come from. Contrast harmonic imaging emerges because contrast agents, which are intravenously injected to enhance the weak echoes backscattered from blood cells, can vibrate nonlinearly when they undergo a acoustic pressure higher than a threshold. Then, these nonlinear signals backscattered by contrast agents are collected to form harmonic images where the linear echoes backscattered from surrounding tissue are supposed to be removed. However, during the wave propagation in tissue, the interaction between the acoustic wave and tissue medium modifies the wave shape and the harmonics of the transmitted wave are also generated in tissue. The presence of tissue harmonic signals, merged with harmonic signals from contrast agents, degrades the image quality in contrast harmonic imaging.

This thesis aims to better distinguish the echoes from contrast agents and the echoes from tissue, whether through designing new modalities, or investigating and optimizing the existing modalities. Our efforts are mainly focused on the multi-pulse techniques in ultrasound contrast imaging.

Firstly, we propose a mathematical background to generalize most of the multi-pulse ultrasound imaging techniques that have been described in previous literatures. The formulation can be used to predict the nonlinear components in each frequency band and to design new transmission sequences to either increase or decrease specified nonlinear components in each harmonic band. Simulation results on several multi-pulse techniques are in agreement with the results given in previous literatures.

Secondly, the techniques using multiple transmissions to increase the CTR are generally based on the response of static scatterers inside the imaged region. However, scatterer motion, for example in blood vessels, has an inevitable influence on the relevance of the techniques. It can either upgrade or degrade the technique involved. Simulations, *in-vitro* experiments from a single bubble and clouds of bubbles, and *in-vivo* experiments from rats show that the phase shift of the echoes backscattered from bubbles is dependent on the transmissions' phase shift, and that the bubble motion influences the efficiency of multi-pulse techniques. Fundamental and second-harmonic amplitudes of the summed signal change periodically, exhibiting maximum or minimum values, according to scatterer motion. Furthermore, experimental results based on the second-harmonic inversion (SHI) technique reveal that bubble motion can be taken into account to regulate the pulse repetition frequency (PRF). With the optimal PRF, the CTR of SHI images can be improved compared to second-harmonic images.

Besides of these considerations relative to generalization and scatterer movement in multi pulse techniques, a new technique, called double pulse inversion (DPI), has also been proposed. The PI technique is applied twice before and after the arrival of the contrast agents to the region of interest. The resulting PI signals are substracted to suppress the tissue-generated harmonics and to improve CTR. Simulations and *in-vitro* experimental results have shown an improved CTR of DPI. However, the presence of tissue movements may hamper the effectiveness of this technique. *In-vivo* experimental results confirm that the tissue motion of the rat during the acquisition is an inevitable barrier of this technique.

**MOTS-CLES** : Ultrasound contrast imaging, Multi-pulse transmission, Contrast agents, Scatterer motion

**Laboratoire (s) de recherche** : CREATIS

**Directeur de thèse**: Olivier BASSET/ Christian CACHARD

**Président de jury** : François TRANCART

**Composition du jury** : Olivier BASSET (Co-directeur de thèse), Christian CACHARD (Co-directeur de thèse), Philippe MARMOTTANT (Rapporteur), Ayache BOUAKAZ (Rapporteur), François TRANQUART (Examinateur), Denis FRIBOULET (Examinateur), Armand ABERGEL (Examinateur)